PHD

ELECTRICAL AND STRUCTURAL PROPERTIES OF GRAPHENE-BASED HETEROSTRUCTURES WITH SELF-ASSEMBLED ORGANIC TUNNELLING BARRIER

Altarifi, Saleh

Award date:
2020

Awarding institution:
University of Bath

ELECTRICAL AND STRUCTURAL PROPERTIES OF GRAPHENE-BASED HETEROSTRUCTURES WITH SELF-ASSEMBLED ORGANIC TUNNELLING BARRIER

Saleh Mansour Altarifi

A thesis submitted for the degree of Doctor of Philosophy

University of Bath
Department of Physics

October 2020

Abstract

In this thesis, a microfabrication process of synthesizing organic self-assembled Van der Waal heterostructures on rigid substrates is presented. The devices presented here consist of graphene monolayers functionalized with *N,N′*-bis[2-(4-pyridyl)ethyl]-naphthalenediimide molecules (NDI-Py) and clipped together to form organic tunnel junction. We will show that the NDI cores lie flat on the graphene surface bound by π-π interactions and the attached functional groups (pyridylethyl groups) are clipped by forming ion-dipole bonds with silver atoms. The molecular self-assembly takes place as molecules self-organise into quasi-crystalline monolayer due to the weak hydrogen bonding between molecular cores which yield a pinhole-free monolayer. Pyridinic endings have two rotational degrees of freedom which allow them to stand above the plane and adopt a conformation suitable for reaching out to another molecule. The molecular bridges serve as an insulating layer that does not require a control over its thickness and position like hexagonal Boron Nitride hBN. The components of the self-assembled devices are fabricated on rigid substrates (SiO_2/Si) yet are designed to be transferred onto conformable substrates. The molecular self-assembly demonstrated in the thesis thus offers a route towards organic Van der Waals devices that benefit from the versatility of chemical synthesis and meet the requirement of flexible electronics.

The structural properties of the organic self-assembled heterostructures are investigated at intermediate stages of the fabrication. Optical microscopy images show the advantages of the fabrication protocol presented in this thesis that include utilizing a thin insulating layer (SiO_2) to locate insulated graphene electrodes on transparent substrates and the technique in using a two-polymer stamp to produce wrinkle-free graphene electrodes. The adsorption of NDI-Py molecules before and after clipping the graphene electrodes is verified by the blue-shift of the Raman peaks of graphene. This blue shift arises from the p-doping of the NDI-Py and the emergence of the NDI-Py peaks in the Raman spectrum. The low temperature scanning tunnelling microscope (STM) images demonstrate that the molecules are self-organised into quasi-crystalline monolayer due to the weak hydrogen-carbonyl bonds between the cores of NDI-Py. This yields a monolayer of

NDI-Py molecules free of pinholes. In addition, the STM images of graphene functionalized with NDI molecules show that the pyridylethyl groups are standing up right which promotes the ion-dipole bonds (Ag-N-Ag) to construct the molecular bridges. The X-ray photoelectron spectroscopy (XPS) measurements reveal that the filling fraction of the pyridinic-N sites with Ag is 65% which is necessary to form the molecular bridges in the heterostructures.

The current-voltage (*I-V*) characteristics of the tunnel junction demonstrate coherent tunnelling consistent with microstructural properties. The *I-V* curves of the heterostructures at 77 ºC yield consistent tunnel barrier width (1.62 nm). Also, the thermo-activated current observed is quenched at low temperature leaving a finite tunnelling component in the current which demonstrates the high-quality tunnel junctions. Tunnelling across the junctions depends on the chemical potential of the bottom graphene electrodes when tuned by a back-gate voltage. This action gives a zero-resistance peak at -8V when the Fermi levels of the electrodes crossed the Dirac points of graphene. This confirms the existence of energy conserving (coherent) tunnelling processes through the structure.

Acknowledgements

I would like to express my great appreciation and offer my special thanks to my supervisor Prof. Alain Nogaret for his support, invaluable suggestions, and sharing his experience all the time (Je vous remercie du fond du coeur). His encouragement during the difficult times is much appreciated. I would like to acknowledge the support of Qassim University and the Saudi Arabian Cultural Bureau in the United Kingdom towards a full scholarship.

My special thanks go to Dr. Dan Pantos for preparing the organic molecules and the great discussions. My special thanks are extended to Dr. Mattia Cattelan from University of Bristol for the XPS measurements and discussing the initial results, Dr. Adelina Ilie and her student Anamaria Trandafir for performing density functional theory calculations and taking the STM images, and Prof. Simon Bending for giving me the chance to use the thermal evaporator. My thank is due to Isaac Taylor-Harrod for helping me to get familiar with the clean room. Also, I would like thank Dr. Stephen Wedge at the David Bullet nanofabrication facility in the University of Bath, Wendy Lambson and Clare Cambridge, technicians at the department of physics in the University of Bath for the quick assistance when needed.

My thanks are due to Dr. Kamal Abu Hassan, Joseph Taylor for their lovely chats in our free times, and for sharing delicious biscuits. I thank my friends in Saudi Arabia for their lovely calls and messages in the difficult times. Also, my special thanks go to Katherine Coburn at the University of British Columbia, Prof. Mark Boley and Dr. Ryan Gordon at the Western Illinois University for their support prior to PhD.

My deepest gratitude and appreciation are for my parents, my brothers (Bandar and Mohammed), my lovely wife Noha Aldakhilallah, my parents in law, and my beautiful kids (Evana, Mariah, and Ibrahim) for their every day-support and being patience during my long journey. I will be always grateful.

Dedication

This thesis is dedicated to my mother Zahwa Alkhateeb who taught me how to hold the pencil to write the first words in my live and who remembers me all the times in her prayers.

Content

1 Introduction

Until the present time, many electronic devices have been built and fabricated on rigid substrates like the field effect transistors (FET) and metal-oxide semiconductor FET (MOSFETs) built based on silicon or III-V semiconductors,[1-3] for example Esaki diodes and light emitting diodes.[4-5] Yet, the need for miniaturising the devices and scaling them on flexible substrates is driven by the need to build conformable electronics like touch screens, wearable sensors, and artificial skins.[6]

FET transistors which utilise thin films of organic molecules or polymers like pentacene as the active layer have been transferred onto flexible substrates.[7-8] These organic films are fabricated at room temperature, low cost, are less complex in the fabrication process, and are flexible. In contrast, the chalcogenide van der Waals heterostructures require high growth temperatures (600ºC–1100ºC) in chemical vapor deposition (CVD) chambers or epitaxial reactors which carry a high infrastructure cost and require a precise control of the growth parameters.[9] Other devices, showing Negative Differential Resistance (NDR) phenomena and behaving as oscillators when biased in the NDR region, are built on crystalline substrates but are yet to be transferred onto flexible substrates. These include Esaki diodes, semiconductor superlattices,[10] and double barrier resonant tunnelling diodes.[2] Making new flexible NDR devices or modifying the current ones to be flexible would allow sensing strain/pressure by measuring the changes in frequencies of these oscillators and implementing them as active components in electronics that could mimic the functions of the biological mechanoreceptors. Also, it would be implemented as active components in voltage amplifiers, or in fabricating multilevel logic memories due to the possibility of producing multi NDR regions as in composite materials.[6, 11]

However, the isolation of graphene as a novel material consisting of a monolayer of carbon atoms covalently bonded together in hexagonal crystal structure exfoliated from a graphite bulk in 2004 by Geim and Novoselov provided a great opportunity to replace silicon channels used in MOSFETs.[12] That is because the silicon-based devices like MOSFETs, the fundamental components of the integrated circuits, are approaching gates leaking through quantum tunnelling. The discovery of graphene paved the way to novel devices that seek to increase scalability of semiconductor devices, and their high integration density by utilizing the two-dimensional materials (2D). As the components of FETs and MOSFETs are scaled down to a few nanometres in size, more problems emerged like the increase in OFF power consumption due to leakage tunnelling between the gate and the conductive channel when thinner dielectrics are used. Even though the use of insulators with high-dielectric constant would overcome the problem of thinning the insulation layer, the barrier heights of these insulators are low which activate the charge-carrier tunnelling between the source and the drain terminals.[13]

Graphene has some potential advantages over silicon and III-V semiconductors as it is a two-dimensional material (2D) that is flexible, stable, planar, translucid, and has high electrical and thermal conductivities.[9] Moreover, it is possible by application of a gate voltage to control the carrier density in the graphene sheets.[12] Isolation of graphene and its use in the FETs has also given researchers the opportunity to utilise other 2D materials like the transition metal dichalcogenides (TMD), including but not limited to MoS_2, WS_2, $MoSe_2$, to explore the chances of building 2D-based electronics.[14]

Most of the fabrication processes of FETs and metal oxide semiconductors such as deposition of layers into structures and photolithography are applicable to a great extent in fabricating graphene-based devices. However, the use of graphene in FETs as a channel replacing silicon[15] faces challenges like synthesising the graphene on flexible substrates, transferring sheets from growth catalyst to the target substrates without degrading its electrical and mechanical properties, depositing into large areas with a control over the grain sizes and crystal orientations, and the difficulty to switch off in-plane conduction due to the zero-bandgap between the conductance and valence bands. The latter limits the use of graphene-based lateral FETs due to the high-power dissipation during the off-state. Also, it results in low ON/OFF ratios when implemented in digital applications.[16] These limitations led physicists to focus on graphene-based heterostructures.

1.1 Van der Waals heterostructures

The idea of tailoring band structure and electronic properties in tunnelling transport perpendicular to the layers has motivated researchers to build graphene-based Van der Waals heterostructure devices as a route to gain similar functions provided by FETs and MOSFETs like amplification and high frequency generation with higher yields. The proposed vertical devices would be two terminal devices, allowing precise control of their thickness and an extreme reduction of their lateral dimensions which is not possible in the case of MOSFETs due to the unavoidable gate leakage. Combining graphene with insulators in the heterostructure devices is necessary to open new functionalities. By building these trilayer devices, it allows one to inject electrons through a tunnelling barrier and induce large changes in the conductance through applying electrostatic back gate (**Figure 1.1**).

The vast change in the conductance is possible in the graphene-based heterostructures as the graphene has vanishing density of states at the Dirac points. This property helps to maximize the tunnelling current by maximizing the number of energy states that satisfy the conservation of energy and in-plane momentum through the control of the gate voltage, or to block the tunnelling current as these filled and empty energy states are misaligned when

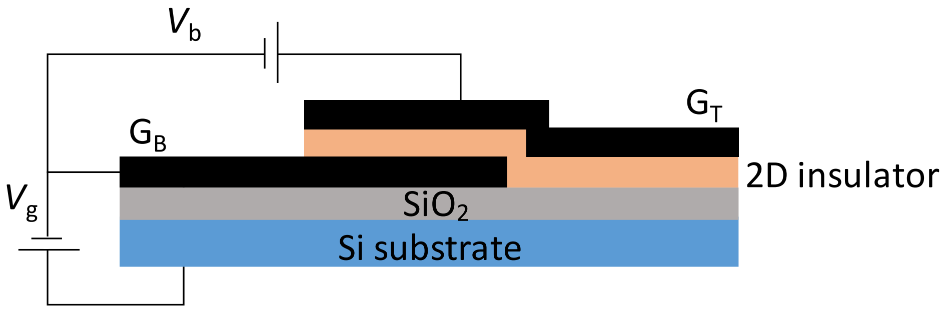

Figure 1.1: Schematics of a graphene-based heterostructure system consisting of top and bottom graphene electrodes and separated by a thin film insulator as a tunnelling barrier all stacked on SiO_2/Si substrate. V_b is the bias voltage applied and the V_g is the gate voltage. Figure source: reproduced form Britnell et al. (2013).[17]

the applied voltage is tuned away from the resonance peak. Another advantage of incorporating graphene in 2D heterostructures is that these materials allow for devices controlled at the atomic scale giving precise control over the designs by utilizing a bottom-up approach. The components of G-based FETs are fabricated on rigid substrates and could be transferred to flexible substrates with the right choice of the materials used, allowing one to explore more physical phenomena.

1.2 Prior art of graphene-based heterostructures

Recent studies have used graphene as electrodes separated by a 2D dielectric layer resembling flexible heterostructure systems to explore the existence of resonant tunnelling and negative differential resistance regions in the current-voltage *I-V* curves of these multi-layered devices.[18-19] The first study of this type was conducted by Britnell et al. in 2012 where hexagonal boron nitride hBN was used as a dielectric layer between two exfoliated graphene electrodes.[18] hBN is an insulator with a large bandgap (5.9 eV) and has hexagonal lattice structure similar to graphene with 1.8% lattice mismatch. The hBN lattice alternates Boron atoms and Nitrogen atoms and is attached to graphene through van der Waal.[20] The tunnelling current density of the device was controlled by a gate voltage.

The graphene/hBN/graphene device made by Britnell et al. in 2013 exhibited NDR regions in the *I-V* curves at low temperature as the conservation of energy and momentum in the tunnelling event is satisfied.[17] The electric field applied between the graphene electrodes misalign the Dirac points which prevents the tunnelling event. The carriers only tunnel when the changes in the momenta are introduced by elastic scattering processes like disorder or interaction effects. In the *I-V* curves of these devices, the current increases steadily at low bias voltage that is applied between the electrodes as a result of weak elastic scattering. The strong peak occurs when the magnitude of disorder leading to a change in electrons momenta reaches a critical magnitude where the conservation of the momentum is relaxed and the Dirac points of the two electrodes are aligned. Once the magnitude of the disorder exceeds the critical value, the tunnelling current drops giving the NDR region.

However, the device showed a peak to valley ratio (PVR) or ON/OFF ratio around 4:1 that is less than the other ratios achieved by the double barrier resonant tunnelling devices like in reference [21] with low current density due to the large bandgap of hBN. The lack of control over the size, and thickness of the hBN flakes, and the mechanical exfoliation method used to produce its thin film would hinder its use in researches and industry. Also, it requires time to find the hBN flakes and locate the precise thickness needed for these devices. Other 2D materials were used like WS_2 and dichalcogenides in general which have the same lattice structure as graphene to produce graphene-based heterostructure devices.[22]

In summary, van der Waals structures that have so far relied on graphene combined with other 2D materials are met with the following challenges: the requirement for lattice matched unit cells restricts the design of heterostructures to a small number of materials and parameters, high growth temperatures that requires a high infrastructure cost, and a precise control of the growth parameters. In addition, the 2D chalcogenides are prone to oxidation especially metallic ones,[9] and the graphene/chalcogenide material system is not biocompatible and not compatible with the needs of flexible electronics. The challenge facing the demonstration of organic Van der Waals structures is the need to organise molecules into the chemically stable, quasi-crystalline, pinhole free monolayers needed to form insulating tunnelling barriers. Also, the supramolecular chemistry provides vast molecular designs to fabricate organic molecule-based heterostructures and replacing the ones with inorganic 2D materials.

1.3 Objectives of the present work

One possible route to overcome the issues mentioned earlier is to build vertical graphene-based heterostructure with a self-assembled molecular dielectric monolayer as a tunnelling barrier. The thesis aims to demonstrate this route as an alternative method for constructing Van der Waals structures. This approach compromises little on physics properties like constant barrier width, no pinholes while allowing tuneability of electronic properties and low temperature growth through self-assembly. In this work, we present a method to fabricate self-assembled graphene heterostructures by using organic molecules specifically *N,N′*-bis[2-(4-pyridyl)ethyl]-naphthalenediimide molecules (NDI-Py) as an insulating barrier. NDI stands for a naphthalene diimide molecule where each side of the molecule is functionalized with alkyl spacer C_2H_4 terminated with pyridine C_5H_5N molecules (Py). The barrier consists of NDI-Py molecules that are adsorbed on each graphene electrode via π-π stacking and are self-organized via weak hydrogen interactions between the cores of the molecules. These molecules will be bound together by inserting the Ag ion of the silver nitrate catalyst between the pyridinic nitrogens to form molecular bridges between graphene electrodes. The complete description of the self-assembled device is presented in Chapter 3. The chosen molecule has a polycyclic core made of four benzene rings which is lattice-matched to the hexagonal structure of graphene. The NDI cores will be shown to be lying flat on highly oriented pyrolytic graphite HOPG and graphene via the Van der Waals interactions.[23] The NDI-based molecules were used in in-plane organic thin film transistors with different alkyl chains and terminal groups as they are planar, stable p-type dopants of graphene, have high electron affinity and high carrier mobility.[24]

The fabrication process is a unique bottom-up approach followed by a controllable stamping process at moderate temperature not exceeding 90ºC. The protocol of the process is designed to be utilized with any suitable engineered NDI-based molecular structures covering a wide range of functionalities offered by supramolecular chemistry. This process is also not costly and is established to fabricate many devices simultaneously to avoid any disparity. Also, the fabrication protocol involves techniques to ease location of the graphene electrodes on transparent polymers which promotes transferring these devices onto flexible substrates. This technique is independent of the graphene synthesis and could include CVD or exfoliated graphene.

We will probe the structural properties of the devices at intermediate stages of the fabrication process. First, this will be done by examining the graphene electrodes` transfer processes and its doping with the molecules using Raman spectroscopy. The Raman study here is to determine the type of bonds that NDI-Py molecules form with graphene, estimating the doping concentrations due to the adsorption of the molecules, and to demonstrate that the thermodynamically stable configuration of NDI molecules is the one where the NDI cores lie flat on the graphene surface. We employ scanning tunnelling microscopy (STM) to study the supra-molecular patterns of the molecules and to assess the suitability of the organic layer to form a uniform monolayer that lies flat on the graphene plane and must be pinhole free. This is combined with density functional theory calculations (DFT) of free NDI-

Py molecules to probe the molecular orbitals when imaging the samples with different tip-substrate polarity. This will help to investigate the low-temperature STM images. We show that the self-organised molecular configurations are driven by hydrogen-carbonyl interactions between the molecules. At the same time, the pyridinic endings of the molecules are standing upright with respect to the graphene plane in order to be ready for clipping with the other endings via Ag+ ions. X-ray photoelectron spectroscopy (XPS) is used to investigate the changes in stoichiometry of the molecular bridges and to determine the filling fraction of pyridinic N-sites with Ag+ ions.

Then, we examine the *I-V* characteristics of the tunnelling junctions of the graphene-based heterostructures at the room temperature (300 K) and liquid nitrogen temperature (77 K). The working principle of these devices is based on the tunnelling of the charge carriers between the graphene electrodes through an insulating barrier when biasing the electrodes. The conductance will be controlled by applying a back-gate voltage which essentially controls the chemical potential of the bottom electrode. We will demonstrate coherent tunnelling between the graphene electrodes. We also fit the *I-V* curves with Simmons equation to validate the exponential dependence of the *I-V* curves. and estimating the tunnel barrier width. We will show that the doping concentration extracted from the electrical measurements validates the doping concentration estimated from the Raman spectra of the graphene electrode doped with the NDI-Py.

1.4 Structure of the thesis

The thesis is divided into six chapters. The first chapter introduces the challenges of miniaturisation the current Si-based transistors and introduces in-plane graphene transistors. Then, it discusses the vertical transport in graphene-based heterostructures and its limitations. We conclude the chapter by introducing the motivation and the aims of this thesis in developing organic van der Waal heterostructures. The second chapter presents the crystal and band structure of graphene, the methods of synthesising, characterising, and transferring graphene. It also explores the organic molecules used in fabricating the self-assembled devices utilising metallic ions, Silver (Ag) in this case. Then, the quantum tunnelling phenomenon is presented followed by an overview of the Simmons` generalized formula of the tunnelling current density in a system consisting of two similar conducting electrodes separated by a thin insulating film. Finally, the chapter is concluded with an overview of the techniques used to probe the structural properties. The third chapter presents our protocol to fabricate the graphene-based heterostructure in detail. It includes the results of different stages of the fabrication process. The fourth chapter explores the outcomes of the structural properties of the self-assembled devices at every stage of the fabrication process by Raman Spectroscopy, STM and XPS. The fifth chapter describes the measurement and interpretation of the *I-V* characteristics of the vertical graphene-based devices at room temperature and low temperature and how the Simmons formula is used to fit the *I-V* curves to validate the tunnelling picture and compare the value of the barrier width extracted from fits with the one obtained from STM. It also explores the effect of applying electric field to tune the conductivity of the flexible devices. The sixth chapter summarizes the results and the outcomes of the project and introduces suggestions and routes to study the devices in the presence of magnetic field to quench elastic scattering processes due to the lack of translational symmetry and observe negative differential resistance. The conclusion underlines how this work could be extended to transfer the devices onto flexible substrates.

2 Background

2.1 Graphene

2.1.1 Crystal and band structure of graphene

Carbon has six electrons that are distributed among the orbitals $1s^2$, $2s^2$, $2p_x^1$, and $2p_y^1$ leaving the $2p_z$ orbital empty where the electron configuration is given as $1s^2$ $2s^2$ $2p^2$ in the ground state. An important property of carbon is its propensity to form bonds hybridizing the 2s and 2p orbitals. Hybridisation is a process of mixing two orbitals like s and p in the presence of other atoms to form a new orbital that holds the same number of electrons in the original ones and make identical bonds with other atoms.[25] This process happens in carbon structures when one electron from the 2s orbital is promoted to the empty orbital $2p_z$ during atom bonding giving rise to different allotropes for carbon like graphite, graphene, and diamond.

Forming covalent bonds between carbon atoms gives rise to Diamond structure as a carbon allotrope when the 2s and 2p orbitals of each atom hybridised and form four sp^3 orbitals that are energetically equal. In this case the carbon atoms are covalently bound in 3D tetrahedral structure. In the graphene case, hybridisation occurs between the 2s, $2p_x$ and $2p_y$ orbitals forming three sp^2 hybridised orbitals that lie in a plane at angle 120° from each other, and the $2p_z^1$ becomes perpendicular to the plane of the three orbitals. This results in delocalizing the electrons of $2p_z^1$ over the graphene plane (π bonds). The in-plane covalent bonds (σ bonds) between the carbon atoms make up the benzene-ring structure of the monolayer graphene. The graphite allotrope is formed when layers of graphene are stacked on each other through the van der Waals interaction [26] Graphite is a semimetal where interlayer coupling introduces the band overlap whereas graphene is a zero gap semiconductor.[27]

In graphene, the carbon atoms are sited in corners of a honeycomb lattice that is split into two sublattices for the transitional symmetry. The nearest neighbour distance a_0 between two carbon atoms in the hexagonal lattice is 1.42 Å. A monolayer graphene crystal structure has a rhombus unit cell that has two atoms, they are A and B (**Figure 2.1a**). The basis vectors $\mathbf{a}_1$ and $\mathbf{a}_2$ of the unit cell that span the triangular sublattices are given by:

$$\boldsymbol{a}_1 = \frac{a}{2}\begin{pmatrix}\sqrt{3}\\ 1\end{pmatrix} \qquad \boldsymbol{a}_2 = \frac{a}{2}\begin{pmatrix}\sqrt{3}\\ -1\end{pmatrix}, \tag{2-1}$$

where a is the lattice constant where $a = \sqrt{3}\, a_o$, $a_o = 2.46$ Å .[28] A diffraction pattern resulted from the real lattice maps the reciprocal lattice hence the reciprocal lattice is a set of diffraction points that are risen by a set of real planes. The basis vectors of the reciprocal lattice $\mathbf{b}_1$ and $\mathbf{b}_2$ can be constructed through the following relations:

$$\boldsymbol{b}_1 = 2\pi\frac{\boldsymbol{a}_2 \times \boldsymbol{a}_3}{\boldsymbol{a}_1.\boldsymbol{a}_2 \times \boldsymbol{a}_3} \qquad \boldsymbol{b}_2 = 2\pi\frac{\boldsymbol{a}_3 \times \boldsymbol{a}_1}{\boldsymbol{a}_1.\boldsymbol{a}_2 \times \boldsymbol{a}_3}, \tag{2-2}$$

considering that $\boldsymbol{a}_3$ in the 2D lattice is given by $\boldsymbol{a}_3 = c\hat{z}$. Then, by using equations (2-1) in (2-2), the reciprocal lattice vectors are:

$$\boldsymbol{b}_1 = \frac{2\pi}{a}\begin{pmatrix}1/\sqrt{3}\\ 1\end{pmatrix} \qquad \boldsymbol{b}_2 = \frac{2\pi}{a}\begin{pmatrix}1/\sqrt{3}\\ -1\end{pmatrix}. \tag{2-3}$$

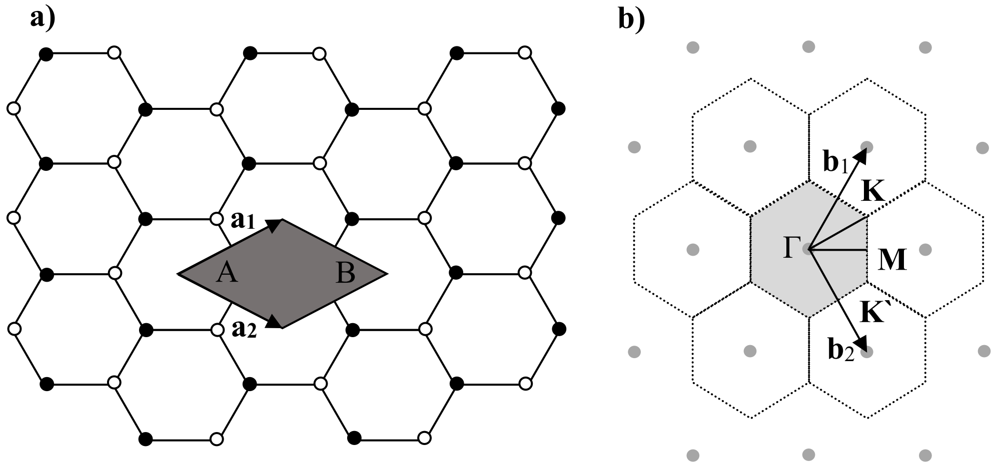

Figure 2.1: Crystal structure of 2D monolayer of graphene. **a)** A hexagonal lattice in real space where the unit cell is represented by the shaded area (a rhombus unit cell) that contains two non-equivalent atoms A (black) and B (white) at the centres of two triangular sublattices. Each sublattice is spanned by the real basis vectors $\mathbf{a}_1$ and $\mathbf{a}_2$. **b)** A reciprocal lattice of the real lattice that has basis vectors $\mathbf{b}_1$ and $\mathbf{b}_2$ in the reciprocal space. The shaded hexagon represents the first Brillouin zone where Γ, K, K`, and M are the high symmetry points in the reciprocal lattice.

The reciprocal lattice has the same structure as the real lattice but rotated by π/2 illustrated in **Figure 2.1b**. The Brillouin zone is constructed by making planes are that are perpendicularly bisecting the reciprocal basis vectors drawn from an origin in reciprocal lattice. These planes enclose the smallest volume in the reciprocal lattice that is called the first Brillouin zone. The corners of this zone correspond to the diffraction peaks of a set of planes of a specific lattice distance in the real space. At the Brillouin zone boundaries, an incident wavevector **k** is diffracted when it satisfies the Bragg law of diffraction**.** The wavevectors reflected by the crystal occur at the edge of the Brillouin where folding occurs. In figure 2.1b, the high symmetry points in the reciprocal lattice are the Dirac points where Γ is at the centre of the first

Brillouin zone (the shaded hexagon), non-equivalent points K and K` at the corners zone are known as Dirac points, and M that is at the midpoint between K and K`. All the points mentioned earlier plays an important role in studying the electronic properties of graphene where the low-energy excitations are around the Dirac points. The two Dirac points **K** and **K`** positions in the reciprocal lattices are given by:

$$\boldsymbol{K} = \frac{2\pi}{a}\begin{pmatrix} 1/\sqrt{3} \\ 1/3 \end{pmatrix} \qquad \boldsymbol{K}` = \frac{2\pi}{a}\begin{pmatrix} 1/\sqrt{3} \\ -1/3 \end{pmatrix}. \tag{2-4}$$

The tight binding method is used to study the band structure of monolayer graphene by introducing the dispersion relation.[29] In 1947, Wallace used the tight-binding method to calculate the band structure of monolayer graphene.[30] Wallace only assumed the in-plane conduction and neglected the interaction between the planes of graphite where the electron does not interact with the other valence electrons in the σ bonds. The method of calculating the band structure started with two atoms at the unit cell of the graphene, two sublattices for the graphene lattice and a hexagonal Brillouin zone in the reciprocal space. As, the valence (π) and conduction (π^*) bands are resulted from the $2p_z$ orbitals overlapping, the approximation considers a single conduction electron and the nearest neighbour interaction between the two atoms in the unit cell. The unit cell used in the calculations is shown in Figure 2.1a.

The dispersion relation that describes the relation between the band energies and the momentum in the k-space is given by:

$$E_{\pm}(k_x, k_y) = \pm\gamma_0\sqrt{1 + 4\cos^2\left(\frac{k_y a}{2}\right) + 4\cos\left(\frac{k_y a}{2}\right)\cos\left(\frac{\sqrt{3}k_x a}{2}\right)},$$

(2-5)

where $E_{\pm}$ in the energy of the conduction (+) and valence band (-), a is the nearest neighbour distance a= 1.42 Å, k_y and k_x momentum components along the x and y directions. The γ_0 term is the overlap energy that depends on the interatomic separation is given by:

$$\gamma_0 = \int X^* (\boldsymbol{r} - \boldsymbol{\rho})(U - V)X(\boldsymbol{r})dr, \qquad (2\text{-}6)$$

X(r) is a wavefunction of the $2p_z$ electron moving in the potential of an isolated atom U , X^* is the conjugated wavefunction , and V is the periodic potential of the lattice. **ρ** is a vector connecting the nearest neighbour atoms. [30] When the energy dispersion relation (2-5) is expanded around Dirac points K and K` in the k-space given by the points in relation (2-4), it shows that the energy band depends linearly on the momentum $\mathbf{k}(k_x, k_y)$,

$$E_{\pm}(\boldsymbol{k}) = \hbar v_F|\boldsymbol{k} - \boldsymbol{K}|, \qquad (2\text{-}6)$$

ν_F is the Fermi velocity $\nu_F = 1 \times 10^6\ ms^{-1}$. At the Dirac points given in relation (2-5), the empty conduction band and the filled valence band meet at the Dirac points where the Fermi energy is sited. Charge carriers are described as massless particles that travel with $\nu_F = c/300$ because the dispersion curve resembles the dispersion curve of photons. c is the speed of light.

When the electron energy dispersion curve is plotted along the high symmetry lines in graphene, the band structure exhibits the π bonding and π* anti-bonding bands (**Figure 2.2a**). As the graphene has two non-equivalent atoms at the unit cell, one atom will promote one electron that is in the $2p_z$ orbital to the π bonding (valence band) and the other atom promotes an electron to the π^* bonding (conduction band) when the electrons of same momentum. The conduction band and the valence band meet at the diffraction peaks which are the K points, indicating that the graphene is a zero band gap material. Hence the electronic density of states is vanishing as the energy bands tend to Dirac points between the conduction and valence band that take the conical shapes in the band distribution (Figure 2.2b). In pristine graphene, the Fermi energy would be at the Dirac points.

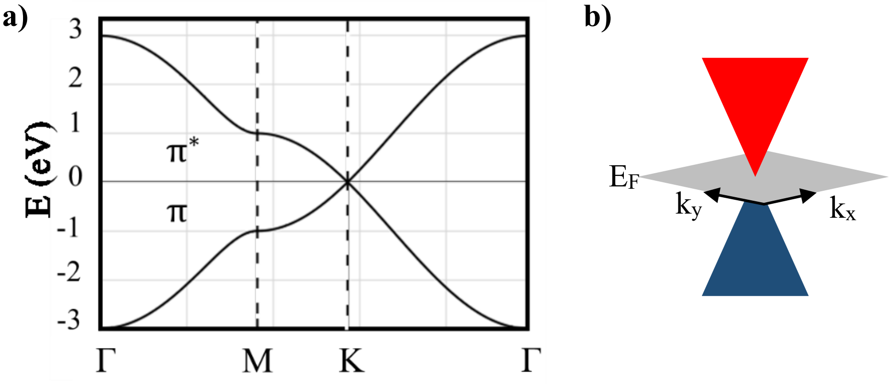

Figure 2.2: a) The energy dispersion curve of graphene along the high symmetry points showing the occupied π and non-occupied π^* bands. **b)** The conical shape of the conduction (red) and valence (blue) bands meeting at a Dirac point that sits at Fermi energy.

Figure 2.3 shows a 3D schematic of the band structure of monolayer graphene where the two bands meeting at the Dirac points [31]. Therefore, graphene is considered to be a semiconductor with a zero energy band gap where the density of states vanishes closer to the Dirac points. If this holds true and the Fermi level is at the Dirac points, the conductance then should go to $2e^2/h$ where e is the electron charge and h is the Planck constant. The deviation from this prediction in experiments is believed to arise from the fact that graphene is warped and has dimples in real space.[32]

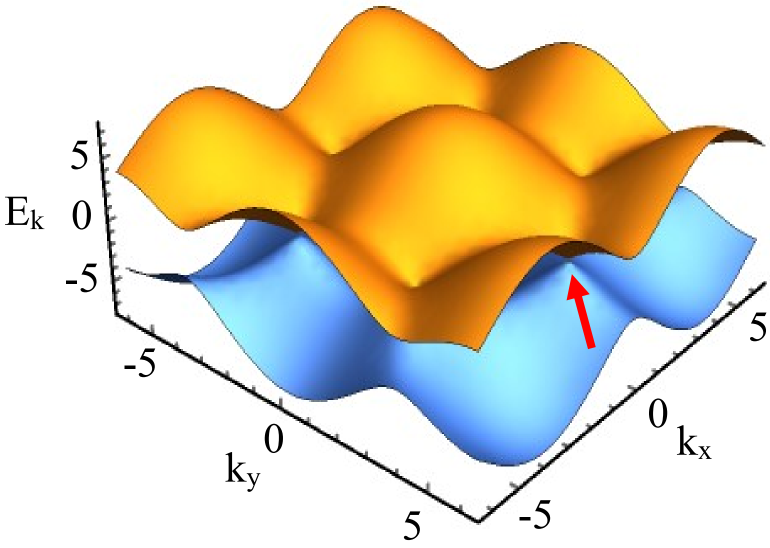

Figure 2.3: The band structure of monolayer graphene where the conduction band (yellow) meets the valence band (blue) based on equation 2-5. The arrow points to the linearity close to the Dirac points in the monolayer graphene.

2.1.2 Synthesis techniques

In 2004, monolayer of carbon atoms bond together through in-plane covalent bonds in a hexagonal lattice has been mechanically exfoliated from graphite bulk by Novoselov and Geim using an adhesive tape and transferred to a silicon dioxide substrate. The isolated graphene was stable and stayed at high quality under ambient conditions.[12] Theoretically, It was concluded that

2D crystal would not exist due to lack of long-range order at low temperatures and due to thermal fluctuations.[33] In 1984, it was shown experimentally that the a few atomic layers have decomposed after growth.[34]

Surprisingly, a scotch tape and highly oriented pyrolytic graphite HOPG were all that was needed to obtain a few layers or monolayer of graphene on silicon wafer coated with a silicon dioxide layer. This process of repeatedly exfoliating the graphite bulk using a mechanical force represented by folding and unfolding the strong adhesive tape is called mechanical exfoliation. Later, another process of synthesising graphene includes chemical exfoliation where polar solvents and surfactants were used. This process also have been used to obtain hBN thin films by Han et al. in 2008.[35] Other processes emerged including chemical and electromechanical reduction of graphene oxide, epitaxial growth of graphene on SiC catalyst and chemical vapour deposition CVD.

CVD is the most frequently process used in synthesising graphene sheets due to the existence of this technology in the industry field, the possibility of setting up in research laboratories, and ability of producing high quality graphene over large areas on metals.[26] Any graphene that could be produced with high quality could be used to fabricate our devices but is it not our intention in this work to explore dependence of the microstructural and electrical properties of our devices on the graphene synthesised by different processes.

We focus here on the CVD process as we are planning to use graphene synthesised by this technique. In general, the process is done by using a mixture of methane CH_4 as a carbon precursor, Hydrogen H_2 and Argon Ar gases, of different ratios, flow over a substrate placed in a quartz tube where the temperature is around 1000 ºC. Then a flow of Ar is used during the cooling step where the temperature is lowered by 10 ºC every second.[36] Similar process was done under low pressure.[37] Nickel has been used as a substrate to form a pyrolytic carbon films by Banerjee in 1961 [38], and used by Karu and Beer in 1966 to produce high quality graphite.[39] Other substrates also were used like Copper Cu and Cobalt (Co).[40] Not only metallic substrates were used, alloy catalysts like Nickel-Molybdenum alloy (Ni-Mo) also have been used to synthesize graphene that leads to the production of a homogenous monolayer graphene sheet by using the CVD technique.[41] Copper-Gold catalyst was another alloy used to grow monolayer of graphene at low temperature close to 900 ºC .[42]

Among all previously mentioned substrates, Cu has been the preferred choice of synthesis graphene due to the production of large areas of monolayer graphene sheets.[43] It is attributed to the low carbon solubility of Cu compared with Ni (0.008% atomic weight at 1084 ºC for copper [44] and 0.6% atomic weight at 1326 ºC for Ni [40] and the low diffusion of carbon on the copper surface. In addition, Cu substrates have the ability to stabilise the carbon atoms through the weak bonding made by the outer shell electron of copper (Ar)$3d^{10}4S^1$ and the $2p_z$ electron during formation of graphene.[26] The produced graphene is polycrystalline with different domain size that depends on the growth conditions. Raman spectra of graphene synthesised on Cu transferred onto SiO_2 show no major defects as concluded in reference [45] in contrast to graphene synthesised on a Ni substrate in reference.[46] In this project, we use CVD monolayer graphene sheets synthesised on Cu substrates to fabricate the graphene-based heterostructure.

2.1.3 Graphene characterisation techniques used in this thesis

All the graphene sheets produced by different processes like mechanical exfoliation and CVD and others are characterised in researches to evaluate their yields in producing high quality, defect-free, large area graphene films on different substrates. These techniques include observation under optical microscopes, Raman Spectroscopy, Scanning Electron Microscopy (SEM), Transmission Electron Microscopy (TEM), Scanning Tunnelling Microscopy (STM), Atomic Force Microscopy (AFM), and Hall mobility experiments. Raman Spectroscopy is of our interest to characterise the graphene sheets used in fabricating the device. Therefore, Raman spectroscopy will be briefly introduced in section 2.4.1 where we focus on the Raman spectrum of a monolayer graphene sheet. This technique helps to study the quality of transferred graphene, the existence of new species and defects due to the fabrication process.

2.1.4 Wet and dry transfer methods of graphene

The synthesised monolayer graphene sheets on metallic substrates or alloy substrates of high-quality face a challenging issue that is how the graphene is transferred without degrading its electrical, chemical, and optical properties. Graphene needs to be transferred from the growth substrates to be used in electronic applications. Therefore, different techniques have been used and modified by researchers to transfer large areas of graphene at high quality to final rigid substrates such as SiO_2/Si, hBN/SiO_2/Si,[17] or flexible ones like Polydimethylsiloxane (PDMS).[47] The transfer process could be wet or dry depending on the polymer used, the growth substrate and the final substrate. This section will focus on the types of transfer processes of graphene by explaining what we mean by the wet and dry transfer processes.

These two processes are essential to set a background for the reader before we introduce our protocol of fabricating our self-assembled devices.

The wet transfer process involves spin coating a graphene sheet on growth substrate with a thin layer of a polymer as a carrier layer that is cured by heat to be a reliable support for the graphene. Then, the substrate is immersed in etching solution to release the graphene while the polymer layer supports the graphene. Then, the graphene/polymer stack is floated on deionised water (DI water) to clean the residue of the etching solution. Finally, the stack is fished by the final substrate and left at an angle to dry. The polymer is dissolved later in a suitable solvent leaving the graphene attached to the target substrate.

For example, Polymethylmethacrylate (PMMA) polymer was used as a support layer to transfer a CVD graphene on Cu to another substrate. The metallic substrate was etched in Ferric Chloride ($FeCl_3$) to free the graphene/polymer stack.[48] The PMMA was also used to transfer mechanically exfoliated graphene layer from SiO_2. In this case, the PMMA/ graphene/ SiO_2 substrate was immersed in etching solution like Sodium Hydroxide (NaOH) to etch some of SiO_2 that is enough to release the graphene and the polymer.[49] The wet process is cheap, easy to use, and used in transferring graphene into different substrates. The drawback of this process is the lack of precise control over the position of the transferred graphene. The wet process may also produce polymeric residues and cracks due to the interaction with etching solvents or due to the water residues left underneath the transferred graphene which affect the graphene properties. [50-51] Yet, there are ongoing researches to enhance the wet transfer processes by adding a second layer of polymers, changing polymers, changing the etching solvents, or changing the curing temperature of polymers.[48, 52]

The other process to transfer graphene is called the dry transfer where a support polymer is attached to graphene layers and transferred to a final dry substrate by stamping without a wet medium. For example, dry transfer is used when exfoliating layers from fresh graphite surface by pressing a scotch tape against the surface and transferred onto SiO_2 surface by repeating stamping process to get thinner layers of graphene.[12] This process gives high quality graphene sheets with less folds and cracks in contrast to the wet transfer, but it lacks the control over the number, location, size and shape of the exfoliated layers.

In most cases, the dry processes were done in two steps where the first step is a wet transfer to a sacrificial layer and the second step is stamping onto the final dry substrate. This approach involves using at least a combination of two sacrificial substrates. Xu-Dong Chen et al. used polyethylene terephthalate (PET) with silicone as a two-layer film.[53] Then, the structure was pressed into the graphene copper followed by etching the copper where the sample was then transferred to the new substrate and the PET/silicone was peeled off. Similarly, a PDMS stamp and PolyIsoButylene (PIB) polymer were used to transfer graphene.[54] Sugkyun Cha et al., for instance, used gold layer deposited on the Graphene/Cu foil and the foil was etched in etchant bath.[55] Then, the Au/Graphene film was fished by a PDMS stamp and Au layer was etched. Finally, the Graphene/PDMS was placed on the final dry substrate and the PDMS was peeled off. It is worth noticing that these approaches could be useful in fabrication processes, yet they still suffer from either metallic residues or polymeric residues or both at the same time. Also, utilising an expensive sacrificial layer like Au is inappropriate in industry where it increases the cost of the fabrication and because it is opaque which does not allow to precisely control position of the graphene.

One of the transfer methods involved using a stack of two polymers to transfer graphene sheets. A hollow PDMS stamp was used as a handle to be attached to the PMMA/graphene film before etching the growth substrate.[51] This hollow stamp minimized the contact area between the PDMS and PMMA in order to minimize the effect of the strong adhesion force between the two polymers. After etching the original substrate, the PDMS/PMMA/graphene was brought in contact with the final substrate where the graphene facing the substrate while heating up for 3 hours at high temperature (~165 ºC) to soften the PMMA polymer allowing the graphene to be transferred. Finally, the PDMS stamp was peeled off and the PMMA was dissolved leaving the graphene sheet on the substrate. This technique is interesting as it involved using two flexible and transparent polymers allowing to control the final position of the transferred graphene. Yet, it required to heat the sample at elevated temperatures for long time which is not a preferable approach. Also, the PMMA/ graphene stack was suspended and not well supported which might lead to folded graphene especially if one wants to increase the area of transferred graphene.

In fact, any combination of the wet and dry transfer techniques is certainly required with some modifications to meet the requirements of any advanced fabrication process. The requirements could be aligning the graphene sheet or patterned graphene into a certain direction, or the need to process the graphene surface before transferring it onto the final substrate. These require one to use polymers that are transparent, easy to precisely control the transferred graphene, and do not require to be treated at high temperature in order to achieve the full transfer. We will show that in chapter 3 how we proceed to achieve these requirements by using PolyIsoButylene (PIB) and PDMS stack to transfer the top part of our device.

2.1.5 Approaches to graphene functionalisation

Functionalizing graphene is a way to change its chemical and electrical properties that could be done by adsorbing carefully designed molecules on its surface.[56] Covalent bonding of molecules or atoms to graphene is possible by functionalizing it with, for example, atomic hydrogen or fluorine which result in decreasing the carrier mobility turning graphene into an insulator.[57-58] Although covalent bond has changed the electronic properties of graphene and introduced band gap in its band structure, it changed the local density of states in the graphene layer by breaking the sp^2 and introducing sp^3 bonding which distort the graphene lattice.

Non-covalent functionalization, another form of modification of graphene's properties, relies on utilizing materials possessing carbon rings with six-fold symmetry and the same lattice parameters as graphene and π bonds to be deposited on the surface of graphene/graphite through van der Waals forces resulting from the π-π stacking. This functionalisation process makes changes to the electrical properties of graphene to fabricate, for example, n-type or p-type semiconductors which help in fabricating graphitic-based solar cells and energy storage devices. This depends on rich/deficient molecular cores of the molecules attached to the graphene surface. For instance, perylene-based molecules were deposited on monolayer graphene by a thermal evaporation process and were found to be self-assembled on the graphene surface without disturbing the graphene lattice or introducing *sp*^{3} bonds.[59] Other molecules have been used to enhance the properties of graphene like aromatic Naphthalene Diimide Molecules (NDI), functionalized with different appendages, used to tune a tunnelling barrier in graphite-silicone interface (**Figures 2.4a, and 2.4b**).[11]

The structural and chemical properties of functionalised graphene are characterized by different technique like Raman Spectroscopy, STM, and XPS to study for instance the doping concentrations, the type of bonding with graphene, and to study how the functionalizing materials are absorbed on the graphene surfaces. In general, the graphene properties are influenced by the properties of the materials used to functionalize it and the ways of interactions with the graphene surface. In the next section, NDI-Py molecules will be introduced which will be used later in this work. The cores of the molecules were attached to the graphene surface via π-π interaction. These molecular cores interact via hydrogen-carbonyl interactions and self-assemble into a thin layer and have rotatable side chains that could be utilized in building supramolecular structures.

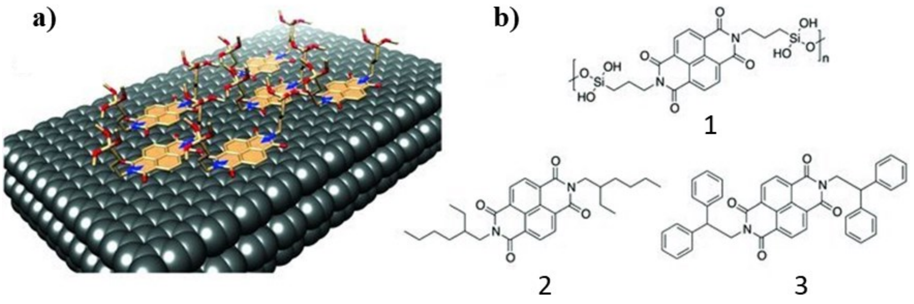

Figure 2.4: Three variants of NDI molecules with different attachments for functionalization graphite surfaces. **a)** Schematic of self-assembly of NDI-Si molecules on graphite nanoparticles. **b)** NDI molecules functionalized at the imides` positions with Si-OH group. Figure source: Littlejohn et al.[11]; ©2013 John Wiley and Sons; adapted with permission.

2.2 Naphthalene diimide molecules NDIs

1,4,5,8-Naphthalenediimides NDI molecule consists of an aromatic naphthalene core with two imide groups attached to it (**Figure 2.5**). Functionalizing the molecules with other groups like silanol (Si-OH) [11] and alkyl chains of different lengths [23] were used in constructing molecular structures and modifying the electronic and optical properties of electronic devices such as, organic field effect transistors [60] and graphitic-based composites.[11] In fact, the NDI molecule and its derivative have been used in fabricating organic molecule-based electronics for being easy to synthesize, electron-deficient, planar, self-organized, and self-assembled by the π-π interaction between the cores of the molecules and the substrates.[61] In this section, we focus on one member of the NDI-based molecules family which is N,N′-Bis[2-(4-pyridyl)ethyl]-NDI, shortened as (NDI-Py), molecule to explore its chemical structure, how it interacts with graphene, and how it is synthesized. This molecule will be employed in our self-assembled graphene-based device.

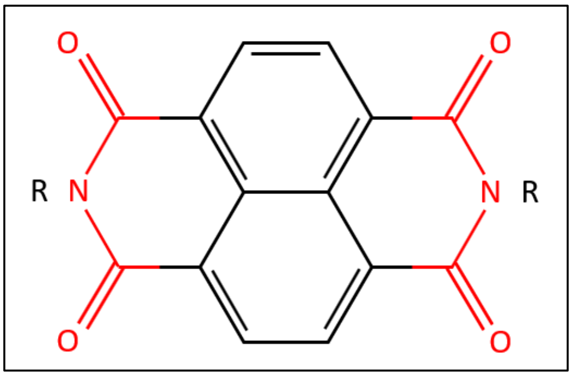

Figure 2.5: Molecular structure of one NDI molecule. The black middle part of the molecule is the naphthalene and the two red parts are the imide molecules (O=C–N–C=O). R represents the functional groups attached to the core of the NDI by bonding to the nitrogen.

2.2.1 Molecular structure and synthesis of NDI-Py

The NDI-Py molecule consists of NDI molecule functionalized at the imides with one ethyl group (C_2H_4) in each side as a spacer attached to its end one pyridine molecule (C_5H_5N). The ethyl group and the pyridine together are called a pyridylethyl group, in the entire thesis. Here, the pyridine ending has lone pair of electrons at the N atom which facilitate forming molecular bridges via ion dipole bonds. The details of the molecular structure of the NDI-Py are shown in **figure 2.6** and combined with the dimensions of the free NDI-Py molecule as this is important in the analysis of the results of the STM discussed in chapter 4.

The length and width of the core of the molecule are 7.23 Å × 6.76 Å, shown in **Figure 2.6a**. The length of the pyridylethyl group shown in **Figure 2.6b** is only about 5.013 Å, but the estimated distance between the nitrogen of the imide and the nitrogen atom of the pyridine (in one side of the molecule) is about 6.595 Å. This means that length of the molecule will be around 19.43 Å in case the molecule is relaxed on the same axis of the core as shown in **Figure 2.6c**. This is not fixed as the total length depend on the conformation of the molecules on the graphene as the side chains are flexible to rotate out of the long axis of the cores. These molecular distances were calculated based on the geometrical parameters published in reference.[62] All hydrogen bonds were included in the calculations. The NDI-Py molecule used in this work was synthesized and characterized by Dr. Dan Pantos' group at the University of Bath as part of their work in synthesising wide range of napthalenemonoimide and N-desymmetrized naphthalenediimide molecules by using a microwave assisted protocol.[63]

Synthesis of NDI-Py

The procedure for making NDI-Py molecules states that the 1,4,5,8-Naphthaletetracarboxylic dianhydride is used with the 4-aminomethylpyridine in 5 mL of dry dimethylformamide in a tightly closed, pressure–resistant microwave tube. Then, the mixture is sonicated until the mixture becomes homogeneous followed by microwave heating

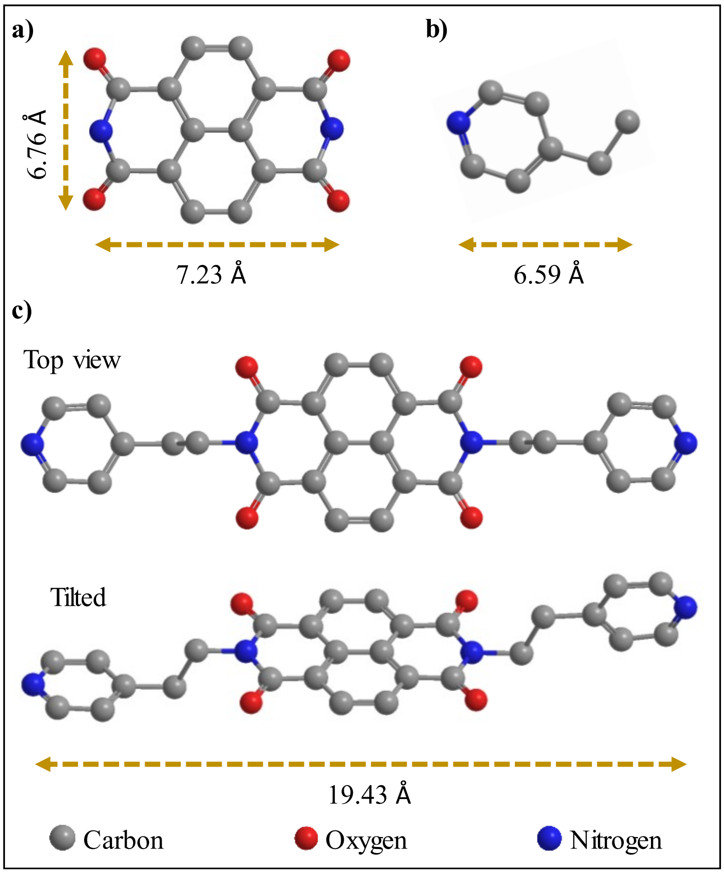

Figure 2.6: Schematics of the molecular structure of a free NDI-Py molecule. **a)** The core of the NDI molecule showing the molecular width 6.76 Å and the length 7.23 Å. **b)** molecular structure of the pyridylethyl molecule (6.59 Å long). **c)** Top and side tilted view of the NDI-Py molecule when the pyridylethyl groups are extended fully (19.43 Å). All hydrogen atoms were omitted for clarity.

at 70 °C for 5 minutes. A second heating process is required at 140 °C for 5-15 minutes. After, the solvent must be removed at reduced pressure and the residue left is suspended by acetone. Then, the suspended residue is added to 1 Molar of stirred hydrochloric acid solution HCl(aq). The outcome is collected, filtered, washed with water, and left to dry in vacuum.[63]

2.3 Theory of quantum tunnelling

Quantum tunnelling is a physical phenomenon that allows the electrons to tunnel between two conducting electrodes separated by a potential barrier due to the particle–wave duality. This event is classically forbidden as the current carriers have no enough energy to surmount the potential barrier. The flow of the current between the electrodes is only possible when the barrier width is comparable to the De Broglie wavelength of the electron. Here, we briefly present the theory of quantum tunnelling by introducing first the transmission probability of a charged particle tunnelling through a potential barrier. Second, we introduce Simmons`s generalized formula of the tunnelling current through a thin potential barrier of an arbitrary shape which accounts for image charges in the tunnelling barrier.[64] Here these image charges are significant given the high dielectric constant of the organic tunnelling barrier.

2.3.1 Probability of transmission through a potential barrier

Consider that an electron of mass m, wavefunction $\Psi(x)$, and energy E is incident on a potential barrier of height V_0 and width d (**Figure 2.7**). Classically, the particle will surmount the barrier if $E > V_0$ and bounce back when $E < V_0$. Yet, in quantum mechanics, there is a finite probability that the electron will tunnel through the barrier if the barrier is thin enough and the height of the potential is not infinite. This non-zero finite probability is derived from the solutions of the time-dependent Schrödinger equation in 1D for the wavefunction of the electron Ψ(x) of mass m approaching a potential barrier from $x = -\infty$,

$$\frac{-\hbar^2}{2m}\left(\frac{d^2\Psi(x)}{dx^2}\right) + U(x)\Psi(x) = E\,\Psi(x), \qquad (2\text{-}7)$$

where $\hbar$ is the reduced Planck constant. The schematic shown in figure 2.7 illustrates the wavefunction of the electron Ψ(x) in 3 different regions of the potential U(x) which are before ($U(x) = 0$), inside ($U(x) = V_0$), and after the barrier ($U(x) = 0$). The general solutions of equation 2-7 represent the wavefunction of the electron in three regions. In region 1 and 3, where the potential barrier height is zero, the wavefunctions of the electron are given by:

$$\Psi_1(x) = A\,exp(ik_1x) + B\,exp(-ik_1x) \quad \text{for } U(x) = 0\,,\ x < 0 \qquad (2\text{-}8)$$

$$\Psi_3(x) = F\,exp(ik_3x) + G\,exp(-ik_3x) \quad \text{for } U(x) = 0\,,\ x > d, \qquad (2\text{-}9)$$

where $k_1 = \sqrt{2mE}/\hbar$ and $k_1 = k_3$. Here, A and B are the incoming and reflected coefficients in region 1, respectively. F and G are the transmitted and reflected coefficients in regions 3, respectively. By assuming that at infinity there is no reflection of the wavefunction that travels in the positive x-direction in region 3, we only consider the transmitted wavefunction. So, we consider G to be zero.

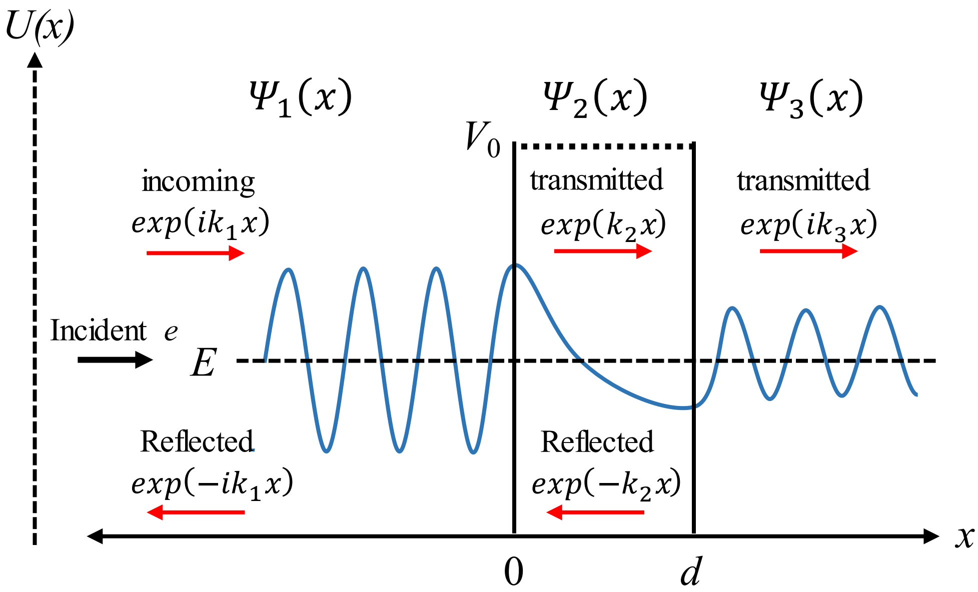

Figure 2.7: Schematic of an electron (e) of a wavefunction $\Psi(x)$ and energy E incident on a potential barrier of height V_0 and width d. Ψ_1(x), Ψ_2(x), and Ψ_3(x) are the solutions of the Schrödinger equation before, inside, and after the potential barrier, respectively. Each solution is a sum of incoming or transmitted and reflected wavefunctions except that the wavefunction experience no reflection behind the barrier.

In region 2, the potential is not zero and the solution to Schrödinger equation is given by:

$$\Psi_2(x) = C\,exp(ik_2x) + D\,exp(-ik_2x) \quad \text{for} \quad U(x) = V_0,\ 0 < x < d, \qquad (2\text{-}10)$$

where $k_2 = \sqrt{2m(E - V_0)}/\hbar$, and C and D are the transmitted and reflected coefficients in region 2. Since E is smaller than V_0 inside the barrier in this region 2, we could rewrite k_2 as $k_2 = \sqrt{2m(V_0 - E)}/\hbar$, and the solution of Schrödinger equation in this region becomes:

$\Psi_2(x) = C\,exp(k_2x) + D\,exp(-k_2x)$ for $U(x) = V_0$, $0 < x < d$ (2-11),

here we notice that the wavefunction of the electron entering region 2 is exponentially decaying as schematically shown in figure 2.7.

To calculate the probability of the electron tunnelling through the barrier, we need to find the ratio of the transmitted coefficient to the incoming coefficient (F/A), where $T = |F|^2/|A|^2$ is the transmission probability. To find these coefficients, the wavefunctions and its derivatives should be continuous at the boundaries of the potential barrier, at $x = 0$ and $x = d$. At the $x = 0$, by equating the equation 2-8 and 5 $\Psi_1 (x = 0) = \Psi_2 (x = 0)$. It yields:

$$A + B = C + D. \tag{2-12}$$

From the first derivatives with respect to x of equation 2-8 and 2-9 and setting $\Psi`_1 (x = 0) = \Psi`_2 (x = 0)$, we get:

$$A - B = \left(\frac{k_2}{ik_1}\right)(C - D). \tag{2-13}$$

Now, we add equation 2-12 and 2-13 to get the coefficient A that characterizes the incoming wavefunction in terms of C and D, where A will be:

$$A = \frac{1}{2}\left[C(1 + \frac{k_2}{ik_1}) + D(1 - \frac{k_2}{ik_1})\right]. \tag{2-14}$$

Similarly, for the boundary conditions between region 2 and 3, at x = d when setting $\Psi_2 (x = d) = \Psi_3 (x = d)$ and $\Psi`_2 (x = d) = \Psi`_3 (x = d)$, we get:

$$C\,exp\,(-k_2d) + D\,exp\,(k_2d) = F\,exp(ik_1d) \tag{2-15}$$

$$-C\ exp\ (-k_2 d)\ +\ D\ exp\ (k_2 d)\ = (k_1/ik_2)\ F\ exp(ik_1 d). \quad (2\text{-}16)$$

To get the C and D coefficients in terms of F, we first add equation 2-15 and equation 2-16 to get the D coefficient in terms of F. Then, by subtracting equation 2-15 from equation 2-15, we get the C coefficient in terms of F. The coefficients are:

$$C = F\frac{exp(ik_1 d)}{2\ exp\ (k_2 d)}\left(1 + \frac{k_1}{ik_2}\right) \qquad D = F\frac{exp(ik_1 d)}{2\ exp\ (-k_2 d)}\left(1 - \frac{k_1}{ik_2}\right).$$

By substituting the value of C and D in equation 2-8, we are now able to write the incoming coefficient A that characterizes the incoming wavefunction in terms of the transmitted coefficient F that characterizes the transmitted wavefunction. Then, the transmission coefficient is given by:

$$\frac{F}{A} = \frac{4\ ik_1 k_2\ exp(-ik_1 d)}{(k_2^2 - k_1^2)exp\ (-k_2 d) + (k_1^2 + k_2^2)exp\ (k_2 d)}. \qquad (2\text{-}17)$$

The probability of the electron to tunnel from region 1 to region 3 through the potential barrier is approximated by WKB approximation method when assuming that we have a wider potential barrier which results in that the term $exp(-k_2 d)$ goes to zero. Then, the approximation of the transmission probability T = $|F|^2/|A|^2$ is given by:

$$T(E) \approx \frac{16\ k_1^2\ k_2^2}{(k_1^2 + k_2^2)^2\ \exp\ (2k_2 d)}. \qquad (2\text{-}18)$$

The transmission probability is simplified by writing it in terms of the energy instead of k_1 and k_2 as follow:

$$T(E) \approx 16\left[\frac{E(V_0 - E)}{V_0^2}\right] exp\left[\frac{-2\mathrm{d}}{\hbar}\sqrt{2\mathrm{m}(V_0 - E)}\right]. \qquad (2\text{-}19)$$

Here, the probability to find the electron tunnelling through the potential barrier depends exponentially on the width of the barrier, the potential height and the energy of the tunnelling electrons. Therefore, any small changes in these parameters leads to a high change in the electron tunnelling probability in the system. This makes the changes in the width of the barrier extremely sensitive.

The transmission probability could reach unity when an electron penetrates a very high potential barrier V_0 that is much larger than the rest energy the electron (mc^2). This results in the formation of positive energy states inside the barrier which match the energy states of the incoming electrons that leads to high tunnelling probability across the barrier. This effect is called Klein tunnelling.[65] This effect in non-relativistic systems is not easy to be observed as it requires large field ($>10^{16}$ $V.cm^{-1}$).

However, graphene has been studied to explore this effect because its quasiparticles exhibit linear dispersion relation acting as massless relativistic particles which lead to be described by Dirac-like equation instead of Schrödinger equation. Also, the energy states of electrons and holes are interconnected in graphene where the states are conjugated, and the quasiparticles are described by two-components spinor wavefunction corresponding to the two sublattices forming the graphene crystal structure. This is analogue to the charge-conjugation symmetry in Quantum electrodynamics (QED) that results in Klein paradox. Another reason that makes graphene suitable to observe Klein tunnelling is the projection of the pseudospin on the direction of motion which is called chirality like the chirality in 3D quantum electrodynamics. All these reasons make it possible to reformulate Klein paradox for a single and bilayer graphene which was conducted by Katsnelson et al., 2006.[65] At small kinetic energies tunnelling in graphene can be however approximated using the Simmons picture which we present in the next section (2.3.2) and which accounts for the polarization of molecular bridges in the barrier.

2.3.2 Electric tunnelling between similar electrodes separated by a thin insulating film

A theory for the electric current tunnelling through a generalized potential barrier of arbitrary shape was conducted by J. Simmons in 1963.[64] This theory will be used in studying the tunnelling event across the junctions of our devices. The derivation was conducted after theoretical studies published earlier than Simmons`s work to derive the tunnelling current through different shape of the potential barriers modified by dipole charges and with different range of voltages across the electrodes.[66] To derive the generalized formula, Simmons started by assuming that there is a thin insulating film separating two similar conducting electrodes, named electrode 1 and electrode 2 (**Figure 2.8**). The derivation was also done under the assumption that the temperature is low which eliminates the contribution of the thermal current to the current between the electrodes.

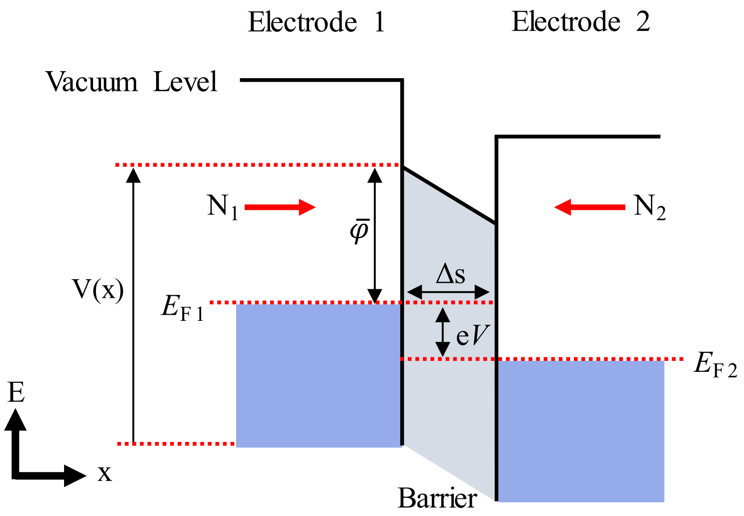

Figure 2.8: Schematics of energy diagram of a system consisting of two similar conducting electrodes 1, and 2 separated by a thin insulating film which induces a potential barrier of height V(x) and width Δs. $\bar{\varphi}$ is the mean potential height from the fermi level of electrode 1. $E_{F\,1}$ and $E_{F\,2}$ are the fermi levels of electrode 1 and 2, respectively. N_1 is the number of electrons tunnelling from electrode 1 to electrode 2, and N_2 is the number of the electrons tunnlling from electrode 2 to electrode 1. V is the applied bias voltage.

The derivation started with the equation of the transmission probability, equation 2-19, after treating it with the WKB approximation where the potential barrier V is a function of x, *V(x)*. equation 2-19 becomes:

$$T(E_x) = \exp\left[-\frac{4\pi}{h}\int_{s_2}^{s_1}\sqrt{2m(V(x)-E)}\;dx\right], \qquad \text{(2-20)}$$

where s_1 and s_2 are the barrier limits at the fermi level of electrode 1. The Energy E is the energy component in the x-direction of the electron as $E_x = mv_x^2/2$ and v_x is the velocity component of the electron in the x direction.

The detailed steps are found in reference.[64] Now, the net flow of the electrons N between the electrodes is calculated by deriving the number of electrons tunnelling between electrode 1 and 2, called N_1, and the number of electrons tunnelling from electrode 2 to 1, called N_2, as $N = (N_1 - N_2)$. Here, N_1 and N_2 are given by the following relations:

$$N_1 = C \int_0^{E_m} T(E)\, dE \int_0^{\infty} f(E)\, dE_r \tag{2-21}$$

$$N_2 = C \int_0^{E_m} T(E)\, dE \int_0^{\infty} f(E + eV)\, dE_r\,, \tag{2-22}$$

where $C = (4\pi m^2/h^3)$, and E_m represents the maximum energy of the electrons for each the electrode. The second integral is derived in terms of the polar coordinate as $E_x = mv_r^2/2$. The $f\ (E)$, $f\ (E + eV)$ functions are the Fermi-Dirac distribution functions of electrode 1 and 2, respectively, given by:

$$f(E) = \frac{1}{1 + \exp[\frac{E - E_F}{K_B T}]} \qquad f(E + eV) = \frac{1}{1 + \exp[\frac{E + eV - E_F}{K_B T}]}\,,$$

where T is the temperature, E_F is the Fermi energy, and K_B is Boltzmann constant. V is the positive potential applied. Equations 2-21 and 2-22 are used to find the total number of the electrons N tunnelling through potential barrier *V(x)* introduced due to presence of the thin insulating film between the electrodes:

$$N = C \int_0^{E_m} T(E)\, dE \int_0^{\infty} f(E) - f(E + eV)\, dE_r\,. \tag{2-23}$$

So, the tunnelling current density J is given by:

$$J = C \int_0^{E_m} T(E)\, dE \int_0^{\infty} f(E) - f(E + eV)\, dE_r\,, \qquad \text{(2-24)}$$

as $J = (Nev)$, e is the charge of the electron, and v is the velocity. Then, the derived formula for the current density tunnelling through a thin insulating film of an arbitrary shape (at T = 0 K) when applying bias voltage V_b is given by:

$$J = J_o \left\{\bar{\varphi} \exp[-A\sqrt{\bar{\varphi}}] - (\bar{\varphi} + eV) \exp[-A\sqrt{(\bar{\varphi} + eV)}]\right\}, \qquad \text{(2-25)}$$

where $\bar{\varphi}$ is the mean barrier height, and

$$J_o = \frac{e}{2\pi h(\beta \Delta s)^2}\,, \qquad A = \left(\frac{4\pi\beta\Delta s}{h}\right)\sqrt{2m}\,.$$

Here, β is a correction factor chosen to be unity for a good approximation, and $\Delta s = (s_2 - s_1)$ is the tunnelling distance through the barrier of generalized shape. Equation 2-25 is one initial possible approach to estimate the insulating barrier thickness and height potentials as free parameters by fitting the *I-V* curves of the heterostructure devices as these devices are made of two electrodes separated by 2D insulating films. This parameter is calculated from the *I-V* characteristic curves when the area of the tunnelling junction is known.

Quantum tunnelling theory is the core principle in studying the electric properties of the diodes, FETs, and heterostructure devices. It paved the way for building imaging techniques like STM. This technique will be briefly reviewed in section 2.4.2.

2.3.3 Electric tunnelling in graphene-insulator-graphene vertical structures

A more realistic model to describe the tunnelling event in graphene-insulator-graphene structures was introduced by Georgiou et al.[22]. In the model, the two graphene electrodes are separated by a thin insulating layer, like WS$_2$. This structure allows one to tune the density of states of the graphene electrodes and to influence the effective potential height of the barrier. The structure is fabricated on an insulating layer on a Si substrate where a gate voltage is applied between the bottom graphene electrode and Si substrate. This increases the carrier concentrations in both electrodes due to the weak screening of the electric field by the bottom graphene layer. When applying a bias voltage between the graphene electrodes, the charge carriers tunnel through the insulating barrier. This model does not consider the conservation of in-plane momentum. In the model, the tunnelling current $I(V)$ between two graphene electrodes is given by:

$$I(V)\ \alpha \int D_B(E) D_T(E-eV) T(E)\ [f_T(E+eV) - f_B(E)] dE, \quad \text{(2-26)}$$

where $D_B(E) = (2|E|/\pi\hbar^2 v_F^2)$ and $D_T(E) = (2|E-eV|/\pi\hbar^2 v_F^2)$ are the density of states of the bottom and top electrodes, respectively. f_B and f_T are the Fermi functions of the bottom and top graphene electrodes, respectively. $T(E)$ is the transmission probability. The expression used to compute the tunnelling current suggests that the in-plane momentum conservation condition is not satisfied. In the model, *T(E)* is given in the following form:

$$T(E) = \exp\left[-2\frac{\sqrt{2m^*}}{\hbar}\int_0^d \sqrt{\Delta - (eV/d)}\, dx\right], \quad \text{(2-27)}$$

where m^* is the effective mass, ħ is the reduced Planck constant, d is the barrier thickness, and Δ is the barrier height. *T(E)* is given by

$$T(E) = \exp\left[-2\frac{\sqrt{2m^*}}{\hbar}\frac{2d}{3eV}\left[\Delta^{3/2} - (\Delta - eV)^{3/2}\right)\right], \qquad (2\text{-}28)$$

By substituting equation (2-28) in equation (2-26) and in the approximation of an energy independent tunneling probability at T = 0 K we find that:

$$I(V)\ \alpha\ (eV)^3 \exp\left[-2\frac{\sqrt{2m^*}}{\hbar}\frac{2d}{3eV}\left[\Delta^{3/2} - (\Delta - eV)^{3/2}\right)\right], \qquad (2\text{-}29)$$

From this model, we see that the tunnelling current in equation (2-29) has a pure cubic dependence at low bias voltages (V^3) at 0 K. This strong dependence of tunnelling current on V is attributed to the fact that the density of states of the graphene electrodes depends strongly on the energy of the carriers, $D_B(E)\ \alpha\ |E|$, which leads to a strong non-linear I-V curves at low voltages and very low temperatures.

2.4 Overview of characterisation techniques

2.4.1 Raman spectroscopy

In Raman spectroscopy, a monochromatic light is used to illuminate the sample to study the interaction between the photon and the molecular vibrations as the scattered photons suffer from energy changes, gaining or losing. There will be different scattering processes that result from illuminating the material (**Figure 2.9**). The First process, called Rayleigh scattering, is an elastic scattering process where the incident and scattered photons has the same energies. The second process occurs when the scattered photons have less energy than the incidents ones and it is called Raman scattering (Stokes scattering). The other process happens when the scattered photons have higher energy than the incident photons, and it is called Raman scattering (Anti-Stokes scattering).[26]

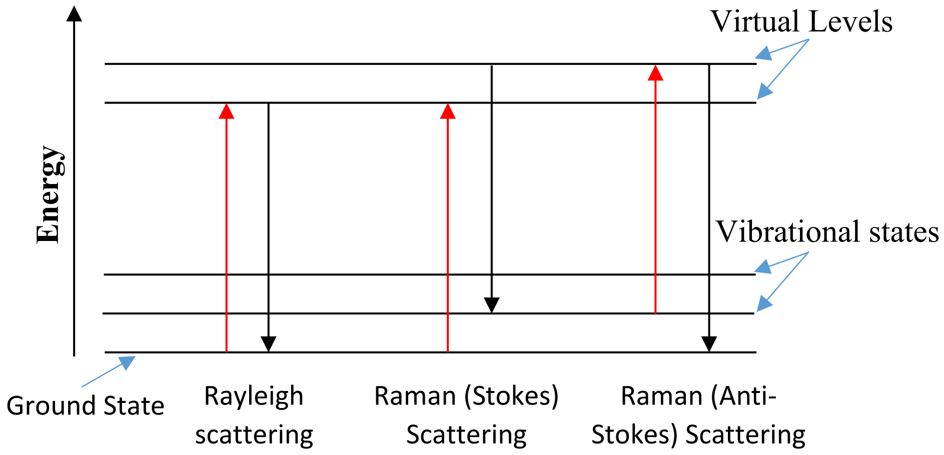

Figure 2.9: Scattering Processes result from illumination of a material by a monochromatic light: Elastic (Rayleigh scattering), Inelastic Scattering processes (Stokes and Ani-Stokes).

Raman spectrometer consists of a source of light of wavelength λ = 532 nm. Filters were used to choose the Raman scattered photons. A spectrophotometer is attached to the device as a tool to split the lights components (colours) by using a diffraction grating or prism combined with a light detector. The intensity of the scattered photons is graphically plotted as function of the frequencies of the laser that is related to the energy shifts. The Raman spectrum is used to study the modes of vibrations through the positions of the peaks, their intensities, peak broadening, and the ratio between them. By studying the absorption peaks in the spectrum, one gets information about the type vibrational modes in graphene which can exhibit resonance lines specific to certain types of bonds in the adsorbed molecules.[67]

In Raman spectrum of graphene, there are four different modes of vibration. The 2D mode is the most intense in the spectrum. It results from a second order double resonant process between the Dirac points in the Brillouin zone. Its position is located around 2700 cm^{-1}. The energy of the 2D peak might change due to the doping of graphene higher (lower) energies in case of p-doping (n-doping).[68] The second main peak is the G peak that results from the bond stretching between the carbon atoms in the graphene sheets. It is considered a first order scattering process [26] positioned at 1580 cm^{-1} (**Figure 2.10**).[68] The G peaks could be split into two peaks due to the existence of impurities (broken symmetry) and a surface charge resulting in another peak called D at 1350 cm^{-1}.[69] The G peak exists when a charge carrier gets excited and inelastically scattered by a phonon followed by elastic scattering by a defect or boundary zone. Similar to the 2D peak, the energy of the G peak changes due to the doping of graphene higher (lower) energies in case of p-doping (n-doping). The other peak is the G` peak that is around 2450 cm^{-1}. This peak resulted from combining the in-plane longitudinal acoustic phonon in the zone boundary and the in-plane optical phonon mode. This peak is sharp for monolayer graphene and it occurs at lower shifts when the number of graphene layers increases.[26]

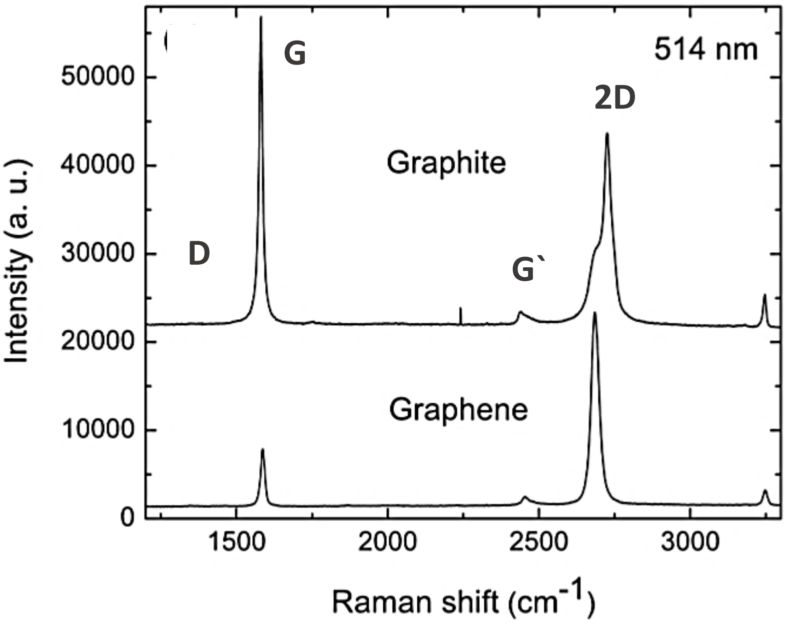

Figure 2.11: The Raman spectra of monolayer graphene and graphite. D peak is not present in this spectrum as there was no clear defect within the tested area. Figure source: Ferrari et al. [68]; ©2006 American Physical Society; adapted with permission.

The number of graphene layers is derived from the intensity ratio between 2D peak and G peak I_{2D}/I_G.[68] In monolayer graphene, the intensity ratio between the 2D and G peaks I_{2D}/I_G is around 4.17 in monolayer graphene, indicating of existence of monolayer graphene while it reaches 0.48 for five layers of graphene.[70],[68] It is also possible to evaluate the level of disorder in graphene by taking the intensity ratio between the D and G peaks I_D/I_G. Higher I_D/I_G indicates that there are more defects in the graphene sample.[71]

2.4.2 Scanning tunnelling microscopy (STM)

In 1982, Binnig and Rohrer invented the STM based on the quantum tunnelling phenomena discussed earlier in chapter 2.[72] The idea of this instrument is to apply a bias voltage between a very sharp metallic tip and the material surface under study which allows the electrons to tunnel to the available empty energy states on the other side depending on the polarity. This is due to the sensitivity of the tunnelling current to the change in the separation between the tip and the surface. The main parts of instrument are shown schematically in **Figure 2.11**. The sharp tip is placed very close to the surface (within 1 nm) to activate the tunnelling mechanism. It is controlled by a piezoelectric tube moving in the x,y, and z directions and connected to a feedback loop to maintain the tunnelling current at constant value if needed.

The design of the instrument allows it to be operated in two different modes: Constant height mode and Constant current mode. Selecting the mode depends on the flatness of the scanned surface and the aim of the measurements. The constant height mode done by fixing the distance along the z-direction with respect to the surface is best when the sample has a flat surface so the tip of the STM will not crash into any part of the sample. This mode allows to probe the local density states of the scanned sample when studying the tunnelling current as a function of the applied bias voltage. If the sample under study has irregular surface or unknown and is expected to be of different heights or being a 3D surface, then the constant current mode would be the best choice to explore the topographical features of the sample. Therefore, the constant current mode will be used to study the molecular configurations of the NDI-Py molecules and the orientation of the endings of the molecules. This mode takes long time to scan the surface compared to the height constant mode as the tip would take time to change the height with respect to the surface. The constant current mode is set up by activating the feedback loop which keeps the current at a pre-set value of the tunnelling current while adjusting the distance between the tip and the sample surface. The scanning in any mode could be done at room temperature or lower temperatures and under ultra-high vacuum at different bias voltage values. The measurements result in images that reveal information about topography of surface when interpreting its local density of states.[73]

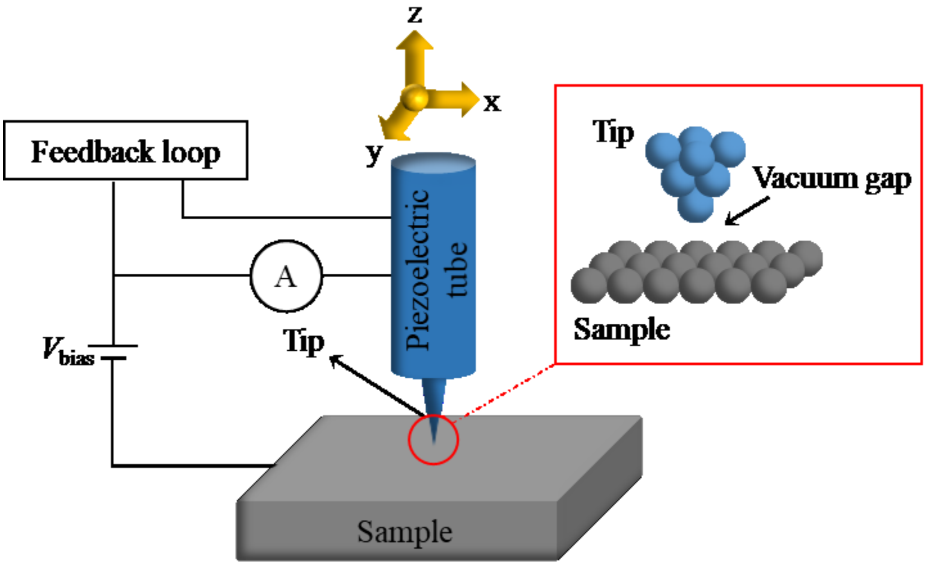

Figure 2.11: Schematics of the main components of the STM illustrating the arrangements of this technique. The tip of STM is positioned within 1nm of the surface and the tunnelling of the electrons is activated by applying a bias voltage between the tip and the sample. The direction of the electrons depends on the polarity. The red box shows the vacuum gap between the head of the tip and the sample in atomic scale.

The local density of states of a sample is revealed when studying the tunnelling spectroscopy as a function of the bias voltage applied to the sample. This gives insight into the local density of states when studying the differential tunnelling conductance. In detail, when applying a negative voltage to the sample and a positive voltage to the tip, the electrons tunnel from the occupied states in the sample to the unoccupied states of the tip. By changing the polarity of the setup, the electrons of the occupied state of the tip will tunnel into the unoccupied states of the sample. Here, studying the measured differential conductance at a certain bias voltage and at each point of the sample surface is used to map the local density of states of the sample.

The STM was employed to study the surface structure of different materials and molecules including the molecular structures of self-assembled organic molecules and the conformation of these molecules on a range of conducting and insulating substrates.[23, 74] This is important especially when they are employed in fabricating organic semiconductors as the molecular arrangement and the interaction with the surfaces play a role in determining the carrier charge transport properties. Yet, the interpretations of the STM images of the aromatic planar organic molecules are affected by the underlaying substrates as the local density of states of the molecules would couple with the local electron density of states of the substrates resulting from the adsorption process. This interaction, especially with metallic substrates, leads to lowering the atomic resolution of images which complicated the analysis of the images of NDI self-organised patterns which we will be reporting. Other materials either conducting or insulating were found to be useful for imaging the aromatic organic molecules due to the weak interaction of the molecules with the substrates like graphite, graphene and hBN.[75-76]

2.4.3 X-ray photoelectron spectroscopy (XPS)

X-ray Photoelectron Spectroscopy is a non-destructive technique to study the surface elemental composition and the chemical states of constituent elements of a sample. The XPS technique was developed in 1956 by a research group led by Kai Siegbahn based on the photoelectric effect.[77-78] X-ray as a source of photons is used to eject electrons from the core levels of the atoms in a sample to the vacuum with different kinetic energies E_k, depending on the energy levels they are ejected from. The emitted electrons are called photoelectrons. Their kinetic energies are detected by an energy analyser located near the surface of the sample and these energies characterize the core energy levels (**Figure 2.12a**). This is done in high vacuum environment to avoid the gas phase collisions, and contaminations. The components of the XPS are mainly X-ray source, sample holder, and electron optics to direct the emitted photoelectrons to an energy analyser. All these components are contained in Ultra-high vacuum system. The whole system is linked to data acquisition system to process the measurements. Simplified schematic of XPS components is show in **Figure 2.12b**.

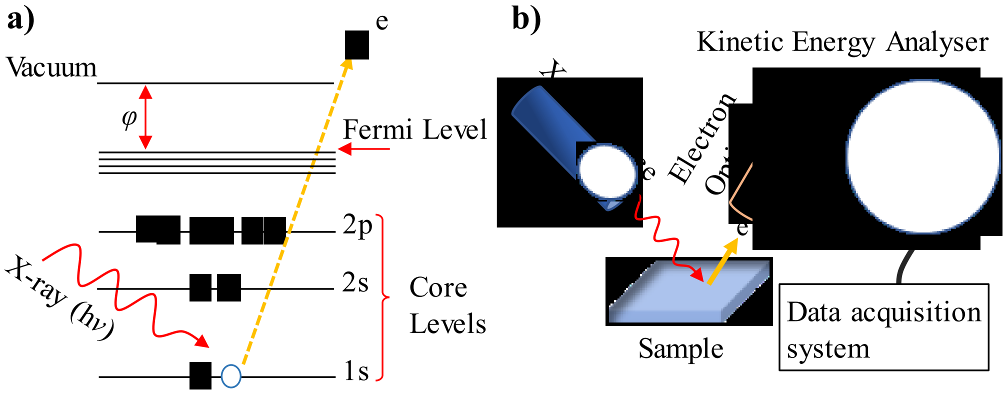

Figure 2.12: a) Schematic of the emitting process of the photoelectrons of a sample`s surface by a beam of X-ray of energy hν, where φ is the work function. **b)** Simplified schematic of the main components of XPS.

2.4.3.1 Interpretation of the XPS Spectrum

The kinetic energies of the core electrons, after absorbing the energies of the photons, will be reduced by an amount equal to their binding energies as they overcome the Coulomb attraction with nucleuses. Once the photoelectrons leave the surface, they lose no energy because they are tens of angstroms away from the surface as the mean free path is about 1.5 nm. These energies are distinctive and are calculated by subtracting the detected kinetic energies from the energy of the photons (X-ray) used to excite electrons:

$$h\nu = E_k + E_B + \varphi\,, \tag{2-30}$$

where hν is the energy of the X-ray source, h is the Planck constant, ν is the frequency of the X-ray. E_k is the kinetic energy of the detected electrons escaping from the sample surface, E_B is the binding energy of the detected electrons to their nucleuses, and φ is the induced work function of the energy analyser. Therefore, the binding energy E_B (with known work function of the energy analyser) is given by:

$$E_B = h\nu - E_k\,. \tag{2-31}$$

The ejected electrons produce peaks in the energy spectrum when plotting the number of electrons emitted from the surface per energy interval as a function of their corresponding binding energies where each element has a set of binding energies. Any changes to the binding energies of the main atoms (chemical shifts) are attributed to the changes in the bonding states (chemical bonding) of these atoms. If an atom is bonded to another atom, for instance, there will a charge transfer that affects the charge potential on the bonded atoms depending on the electronegativity which is defined as the tendency of an atom to attract the shared electrons with another atom. Here, the electronegativity is inversely proportional to the binding energies.[79] Tabulated values of the binding energies found in well-known references and databases of the binding energies are used to identify the bonding states of the sample under study.[80] The XPS analysis is possible if the peak deconvolution is applied to the acquired spectra which helps to identify the bonding states of the atoms and the corresponding intensities for further analysis.

Once the high-resolution spectrum of each atom in the sample is acquired, the elemental composition of the sample could be quantitatively determined by calculating the atomic ratios of the atoms. A combination of Lorentzian and Gaussian functions is used to fit and deconvolute the XPS spectra in order to calculate the atomic ratios of an atom in different bonding states. This is done after subtracting the background of the spectrum. For the quantitative analysis, the normalised area under the curve from each element`s spectrum represents the number of atoms detected in the sample and it is calculated by using the following relation [80]:

$$\text{Number of Atoms} = \text{normalized area} = \frac{\text{Area under the curve}}{(\text{dt}).(\text{No. of Scans}).(\text{S})}, \tag{2-32}$$

where the area under the curve represents the number of electrons detected per second, (*dt*) is the interval time, and *S* is the atomic sensitivity factor for each element. The sensitivity factor is the product of x-ray flux, the photoelectric cross-section for the atomic orbital, the angular efficiency factor based on the angle between the photon and the detected electrons, the efficiency in formation of photoelectrons of the normal photoelectron energy, the mean free path of the photoelectrons, the area of the sample from which the photoelectrons are detected, and the detection efficiency.[80] When the normalized area of each component of the sample is calculated, one could determine the atomic ratios of the constituent atoms or the atomic fraction of any component with respect to the total components.

3 Synthesis of Organic van der Waals Heterostructures

In this chapter, we introduce the design and the synthesis of the graphene-based heterostructures in details. The chapter is divided into three parts. The first part details the lithographic process for patterning monolayer graphene into ribbons of different widths. The second part introduces how a monolayer graphene sheet on a metallic catalyst was transferred into a two-polymer flexible transparent sacrificial substrate to ease locating the graphene electrodes and releasing the electrodes in the designated places. The third part explains how the self-assembly of the device was done. Then, the results will be presented and discussed.

3.1 Description of the design

The fabrication technique used in this research is a bottom-up method for assembling van der Waals heterojunctions. By functionalizing two graphene ribbons with NDI-Py molecules and clipping them through their pyridylethyl endings, we form high quality graphene/NDI-Py-Ag-Py-NDI/graphene tunnelling junctions. The fabrication process was designed to build a graphene self-assembled device, shown in **Figure 3.1a**, which is a tunnelling device with bottom and top graphene ribbons synthesized by optical lithography and reactive ion etching on a rigid substrate. The top and bottom electrodes are aligned and self-assembled using a specifically designed dry transfer technique to form a cross junction where tunnelling occurs. The self-assembly is performed by functionalizing two graphene ribbons with NDI-Py molecules via π-π interactions. The pyridylethyl groups attached to the NDI core rise above the plane and have 2-rotational degrees of freedom (**Figure 3.1b**). This is due to the steric repulsion between the two carbonyl groups on each side of the molecule and the CH_2 group which prevents the side groups from interacting with the graphene substrate. This effect has been observed in molecular conformations of NDI molecules functionalised with longer side chains.[23, 74] Here, the pyridylethyl are restricted to articulate about the B-axis which yields either an U-shaped or a Z-shaped isomer where the Py endings are on the same side or on opposite sides of the symmetry axis, respectively (Figure 3.1b). Also, the pyridine rings may tilt relative to the NDI plane with an angle α. The stable energetic state of the molecule is discussed in chapter 4 when discussing the predictions of the density functional theory. In details, when the naphthalene core of the molecule attaches to graphene, the N atoms of the pyridine endings can form ion-dipole bonds with Ag^+ ions. We use silver nitrate to form N-Ag-N bonds and in this way the NDI molecules on graphene ribbons are attached to form an insulating organic flexible tunnelling barrier at the centre of the cross (**Figure 3.1c**).

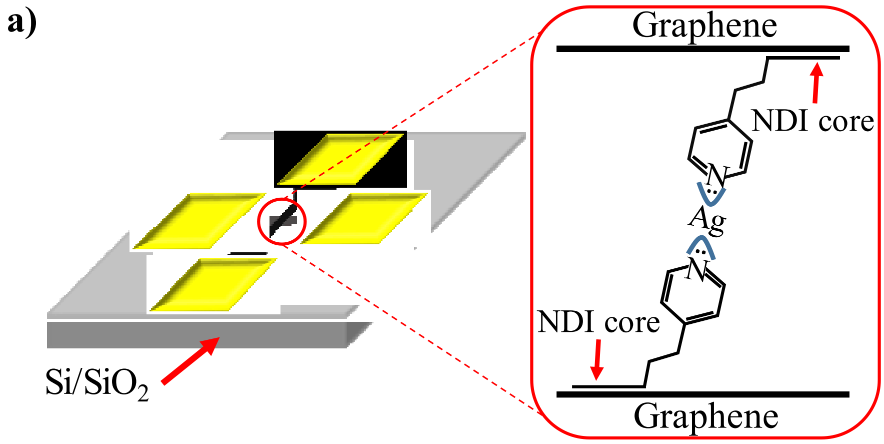

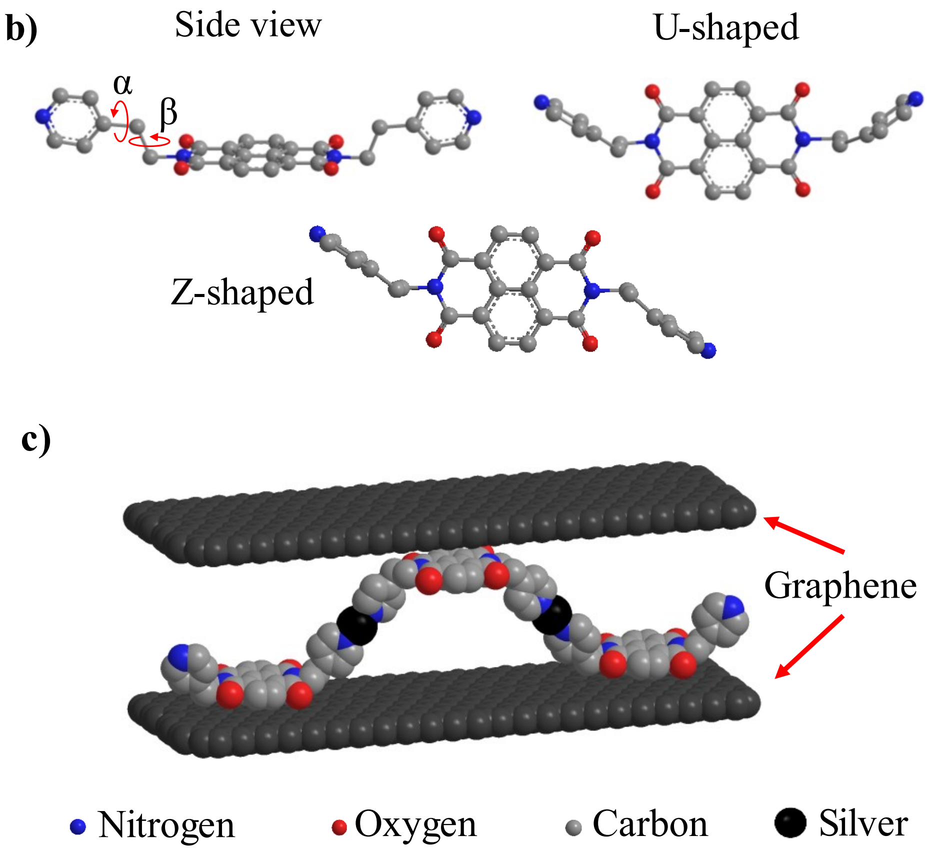

Figure 3.1: a) Schematics of the self-assembled tunnelling junction at the intersection of the two graphene ribbons (black/gray). The junction is fabricated on a SiO_2(300 nm)/Si substrate. **b)** Side and top views of the NDI molecules. The naphthalene diimide cores anchors the molecules to the graphene ribbon. The pyridylethyl groups are raised above the graphene plane with 2-rotational degrees of freedom with respect to the plane of the NDI core. The ethyl arm may tilt forward or backward with an angle β making: U-shaped molecule when both pyridylethyl groups are on the same side, or Z-shaped molecule when the groups are on opposite sides. The pyridine ring tilts relative to the NDI plane with an angle α around its own axes that is parallel to the NDI plane. **c)** The expected molecular bridge between the graphene electrodes obtained by linking the pyridine endings via ion-dipole bonds with Ag^+ ions.

3.2 Fabrication procedures

3.2.1 Bottom graphene ribbon on SiO_2/Si substrate

This part begins with fabricating the bottom electrode from CVD monolayer graphene on a SiO_2/Si wafer through an optical lithography process to create the ribbons. This is followed by Reactive Ion Etching process RIE in O_2 plasma to etch away interstitial graphene. **Figure 3.2** shows schematics of the process in three main steps. As received a 1 cm^2 CVD monolayer graphene sheet on 300 nm of SiO_2 on Si substrate, (purchased from Graphenea) was spin coated with 1.3 um thin layer of a positive photoresist (PR) (MICROPOSIT, S1813) at 4000 rpm. Any beads of PR at the corners should be removed, step 1. The PR was soft baked at 363 K for 30 minutes in a convection oven (Figure 3.2, step 1). The baking process is interrupted after 15 minutes to dip the samples in chlorobenzene for 3 minutes, blow dried with N_2 gun, and returned to the oven to complete the baking process. The chlorobenzene dip helps to harden the top surface of the photoresist which results in slowing down the developing of the top surface with respect to the rest of the PR underneath for better undercut of the sidewall of the photoresist which is essential for a successful lift off process.

A Karl Suss MJB3 contact mask aligner and a mask were used to expose the samples covered with baked photoresist to Ultra-Violet light UV for 8 seconds in order to make the exposed areas dissolvable in a developer, (Figure 3.2, step 2). The mask has light and dark field areas that define the exposed areas of the photoresist and the shape of the patterns in each lithographic layer. The polymer underneath these patterns are not exposed and will not dissolve in the developer. These patterns will protect the graphene underneath during the etching of unwanted graphene. This process required the mask and the sample to be in contact mode before the UV exposure where the edge of the mask was aligned to the edge of the sample for better patterning with the help of the marks at the corners. The samples were dipped in the aqueous alkaline solution developer (351) diluted in Deionised water DI (Developer 351: DI) (1:3.5) for 40 seconds to dissolve the exposed photoresist. Then, the samples were immersed immediately in DI water for 1 min to stop the developing process and blow dried with N_2 gun.

Inductive Coupled Plasma etcher ICP 100 (Oxford Plasma Pro System 100, Power: 70 Watt, Pressure: 10 mTorr, Flow rate: 10 sccm) was used to etch the interstitial graphene in Oxygen plasma and this process is called Reactive Ion Etching RIE (O_2). It took 15 seconds to etch a monolayer of graphene on SiO_2 /Si substrates without burning the photoresist covering the graphene ribbon.[81] After, the photoresist was dissolved in Acetone for 30 minutes, washed with Isopropyl Alcohol IPA to remove the residues of acetone, and blow dried with N_2 gun (Figure 3.2, step 3). IPA and N_2 gun were used every time we used Acetone in the entire process.

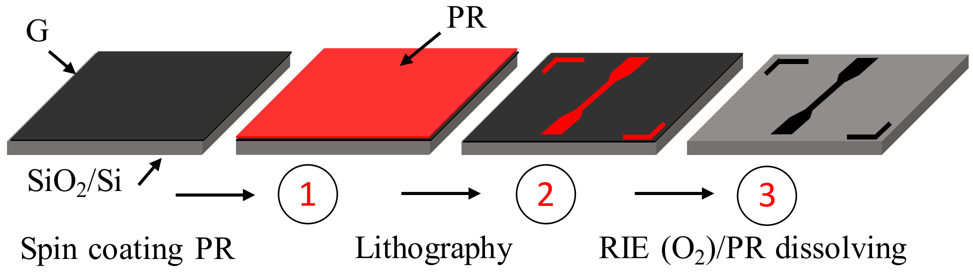

Figure 3.2: Schematics of the lithography process for pattering the bottom graphene ribbon in RIE (O_2). The graphene is spin coated with photoresist (PR). L-shape marks in step 2 at the corners help in the alignment at later stage of the fabrication process.

3.2.2 Transfer of top graphene ribbon onto a two-polymer stamp

The top graphene electrodes were fabricated from a CVD monolayer graphene sheet on 1 cm^2 Cu foil (purchased from Graphenea) by an optical lithography with the same dimensions as the bottom electrodes followed by RIE process (**Figure 3.3**). Step 1, and step 2 in section 3.2.1 were followed to produce the same graphene ribbons on the Cu foil (Figure 3.3, step 1 and step 2). Here, the copper foil had to be in a complete contact and fixed to the wafer holding it before placing it in the ICP 100 chamber. This procedure prevents the samples from heating up during the etching process which may cause, if it happened, the photoresist combusts. After, the graphene in the back of the copper foil was removed by a RIE process. Then, the photoresist covering the graphene ribbons was kept undissolved and the etched areas were covered with a 30 nm thin insulating layer of SiO_2 to enhance optical contrast and facilitate alignment of the top and bottom ribbons (Figure 3.3, step 3). The SiO_2 deposition was done via Electron-Beam evaporation process, using Edward FL-400 auto 306 Evaporator, followed by a lift off process in acetone for 20 minutes to expose the graphene ribbons.

To transfer the graphene electrodes on the Cu foil onto the final substrate, we used a transfer process which enabled us to functionalize the graphene ribbons with the NDI-Py molecules just before completing the transfer. The transfer process involved using a two-polymer stamp. These polymers were PDMS stamp and a self-release adhesive polymer PIB as sacrificial substrate to transfer the top graphene electrodes to the final substrate (SiO_2/Si). Therefore, we prepared the two polymers earlier. The PDMS solution was prepared by mixing Sylgard 184 Silicone Elastomer Kit (Base) with Sylgard 184 Silicone Elastomer Kit (Curing agent) in the ratio

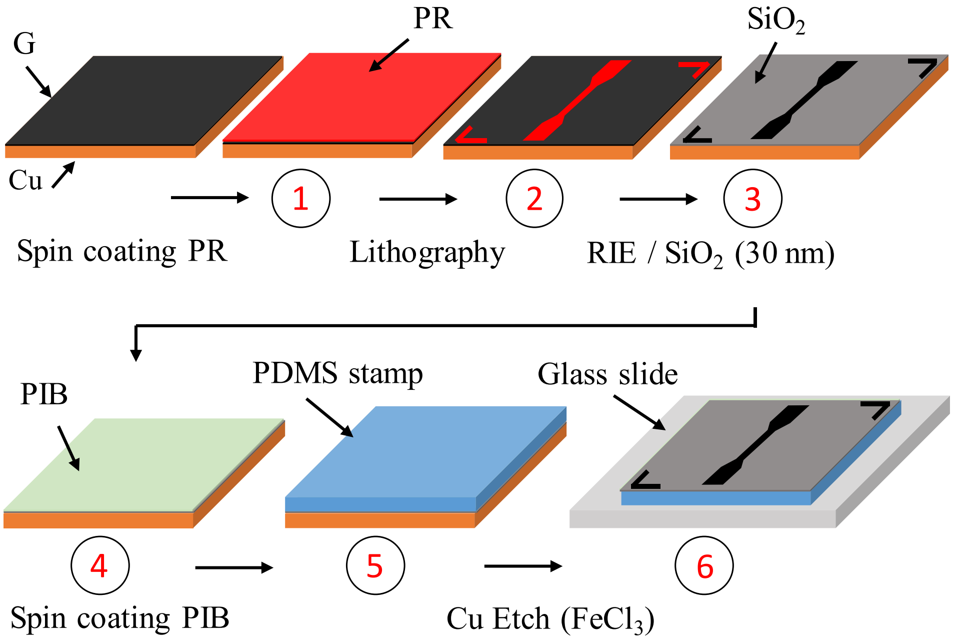

Figure 3.3: Schematics of the lithography of the top graphene ribbon on a Cu foil. In step (3), 30 nm of SiO_2 was deposited to facilitate the alignment to the bottom ribbon. After the ribbon was fabricated, PIB was spin coated (step 4), cured and attached to a PDMS stamp (step 5). The stack is placed on a glass slide after etching the Cu foil for further processing (step 6).

10:1. The mixture was poured into a pre-made glass mold to produce a 1.2 mm thick 10 cm wide stamp. Then, it was left at room temperature to release the air bubbles trapped in the mold. Soft sonication could be used to remove the air bubbles faster. After, the mixture was cured at 373 K in a convention oven for an hour. The mold should be cooled slowly until it reaches room temperature. This helps to reduce the fast shrinking of the glass mold and keep the flatness of the PDMS stamps. Then, the PDMS sheet was released from the mold and cut into 1.4 x 1.4 cm^2 stamps which will be used to transfer individual chips of corresponding size. The PIB polymer was prepared by dissolving the PIB in decane (30 gm.mL^{-1}). At this stage the two polymers are ready to be used in the dry transfer process.

The graphene bars on Cu foil were spin coated with PIB at 4000 rpm and baked for 8 minutes at 363 K on a hot plate (Figure 3.3, step 4). Then, PIB/graphene/Cu stack was adhered directly to a 1.2 mm thick PDMS stamp making a conformal contact with PIB layer (Figure 3.3, step 5). Any residues of the PIB in the back of the Cu foil was wiped gently by acetone. After, the stack was flipped on the Cu side and placed in a Ferric Chloride $FeCl_3$ (0.5M) solution and the PDMS/PIB/Graphene/Cu stack was floating freely in the solution. Once the copper was etched completely, the stack was floated in DI water and then placed on glass slide (flipped on the PDMS side) to be dried by the blow of a N_2 gun (Figure 3.3, step 6).

3.2.3 Assembly of tunnelling device

The third part of the fabrication process consisted of two steps. The first step consisted in evaporating NDI-Py to form a uniform coating on the top and bottom graphene ribbons followed by drop casting the $AgNO_3$ on the bottom electrode only. The second step consisted in transferring the top graphene ribbons onto the final substrate and is called the stamping process.

3.2.3.1 Functionalising with NDI-Py molecules

When graphene is functionalised with NDI-Py, our expectation, which we will demonstrate to be true in this thesis, is that the cores of the molecules should bind to the graphene electrodes by van der Waal forces whereas the pyridylethyl arms would be standing out of the graphene plane. By estimating the area occupied by one molecule and the target area to be covered, we calculated the mass of molecules needed to be evaporated to obtain a monolayer of NDI-Py with uniform coverage over the graphene surface. To estimate the quantity needed, we need to calculate the area of the hemispherical surface corresponding to the propagation front of molecules travelling from the crucible to the sample and the footprint of a single molecule.

In our thermal evaporator, samples are placed ~10 cm above the crucible holding the NDI-Py molecules. We assume that the sublimated molecules diffuse isotropically in the hemisphere above the crucible. Hence, the fraction of molecules reaching the 4×4 cm^2 sample area is 2.5% of the total evaporated. In order to deposit an amount of NDI-Py equivalent to a single monolayer, we first estimated the footprint of a single molecule lying flat on graphene. Based on tabulated bond lengths [62], we find this footprint to be 1.6 nm^2. Hence 5.3×10^{15} molecules are needed to cover the sample surface. When molecular endings stand vertically out of the plane, the footprint of the NDI-Py molecule is the footprint of its core: 0.48 nm^2. In this case, 1.7×10^{16} molecules are needed to form a monolayer. Given that there are 2.1 millimoles per gram of NDI-Py, the mass needed to deposit a single monolayer is between 4.2 µgm and 14 µgm. In practice, we loaded the crucible with ~14 µgm to maximise the chance in producing highly packed monolayer of the molecules that is free of pinholes.

The amount required for evaporation were roughly weighed and mounted on a boat in a thermal evaporator chamber (35 Amps, Pressure below 8.6 x 10^{-6} Torr). Doping the graphene with NDI-Py molecules was followed by drop casting aqueous solution of silver nitrate $AgNO_3$ (0.01M) onto the SiO_2 substrate patterned with bottom ribbon only. The solution covered the whole surface of the substrate. The sample was covered with a black lid to prevent the decomposition of $AgNO_3$ and let to dry in air at 313 K. This was followed by DI water rinse to remove any excess of silver as this step is important for promoting the formation of metals bonds by eliminating residues which might interfere with the bonding process.

3.2.3.2 Transfer of top graphene: Stamping process

To achieve a full transfer of the top electrodes, we used a glass slide with a hole of area that is smaller than the area of the PDMS which acted as a frame to handle the stamp. This frame reduces the contact area of the PDMS stamp with the glass holder and allows the PIB thin film to adhere well to the final substrate. In this case only the edges of the PDMS stamp are held by the glass, (**Figure 3.4, step 1**). Using a glass holder without a hole would result in weak visibility of the graphene bars through the multiple surfaces and in weak adhesion between the PIB thin film and graphene with the new substrate (SiO_2/Si) when peeling off the PDMS due to the large contact area with glass.

The stack graphene ribbons/PIB/PDMS on glass and the bottom graphene ribbons on SiO_2 substrate were inserted separately in the mask aligner to align these top and bottom graphene arrays with respect to one another with the help of the alignment marks at the corners (Figure 3.4, step 1). To perform the transfer, the stamp was brought in contact with the final substrate. Then, the edges of the PDMS stamp were released from the glass slide to complete the stamping process within the mask aligner. After, the whole structure was released from the mask aligner and placed on a hot plate for 10 minutes at 363 K and the PDMS stamp was peeled off very slowly while the structure

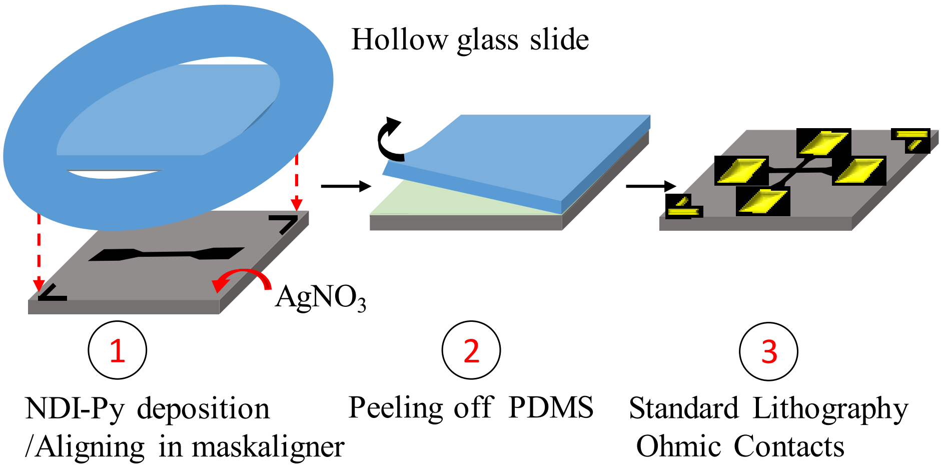

Figure 3.4: Schematics of the alignment process and bonding of the top and bottom electrodes. Both graphene electrodes were functionalised with the NDI-Py molecules and the substrate only was coated with $AgNO_3$. The glass slide should hold the stamp at its corners only as shown in step 1 to ease the alignment and stamping process. Step 1 also shows how the top and bottom marks at the corners should be aligned before stamping. Once they are aligned and stamped, the top graphene ribbons/PIB film were transferred (PIB is dissolved later in decane) to the final substrate, step 2. This was followed by a lithography process to deposit the Cr/Au ohmic contacts on the bonding pads at the extremities of the graphene ribbons, step (3).

on the hot plate (Figure 3.4, step 2). Later, the PIB film was dissolved by immersing the structure in decane for 15 minutes on a hot plate at 318 K. The obtained tri-layer structure was washed with acetone, IPA and blow dried with N_2 gun.

Finally, by using the lithography process mentioned in section 3.2.1 and a mask designed to deposit the contacts at once, 20 nm thick layer of chromium and 200 nm thick layer of gold were thermally deposited on the terminals of the devices as Ohmic contacts (Figure 3.4, step 3). Control devices were fabricated according to the same process for performing electrical measurements that are presented in chapter 5: control devices without Ag+ ions (graphene/NDI-Py-NDI-Py/graphene), and control devices without NDI molecules (graphene/graphene). Actual and control devices were processed simultaneously under the same processing conditions.

3.3 Results and discussion

Figures 3.5a and 3.5b show optical microscopy of base graphene ribbons on SiO_2/Si substrate after RIE process with two different processing times 1 minute and 15 seconds, respectively (other parameters were fixed). We varied the processing time to minimize the polymerization of the photoresist as this step may result in residues of cross-linked photoresist. Clearly 15 seconds were just enough to etch the exposed graphene areas and not to crosslink the photoresist film. This is verified each time by the absence of the residues that were observed in **Figure** 3.5 under the optical microscope and the Raman study that is presented later in Chapter 4. Longer time than 15 seconds may be considered only when etching graphene with higher thickness than the thickness of monolayer graphene.[81]

To etch the graphene sheet on Cu, it required us to place the copper foils in conformal contact with the holder to avoid accumulation of heat during the plasma etching of graphene on the substrate which may cause the photoresist to cross-links (non-dissolvable). Another problem which we avoided when etching graphene on Cu is the possibility of oxidizing the copper surface. This was eliminated by reducing the time of etching process

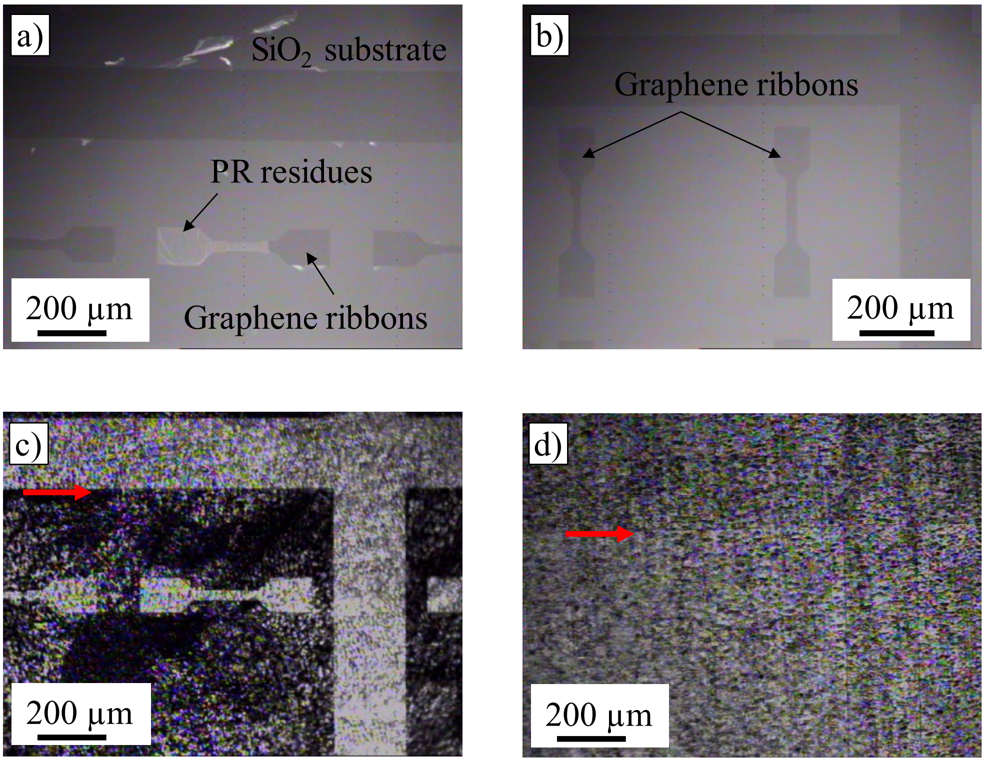

Figure 3.5: Optical Microscopy of the samples after etching the exposed graphene on different substrates. **a)** A micrograph of a bottom graphene ribbon covered with crosslinked thin layer of photoresist due to the long etching time in O_2 plasma (1 minute). **b)** A micrograph of bottom graphene ribbons after 15 sec in the ICP 100 chamber. No photoresist residue was observed. **c)** A micrograph of the Cu surface being oxidized after the removal of unwanted graphene. **d)** A micrograph showing no oxidization happened to the Cu surface after 11 seconds in O_2 plasma. Red arrows point at the boundaries between the Cu surface and the photoresist covering the graphene marks.

to 11 seconds instead of 15 seconds. Figures 3.5c and 3.5d show two copper foil surfaces after etching the unwanted graphene in the plasma for 15 seconds (dark areas) and 11 seconds (bright areas), respectively. Therefore, optimizing the etching time is essential step to obtain monolayer graphene with the minimum photoresist residues. Any residues of the photoresist obviously hinder the graphene properties and affect the transfer of the graphene onto the final substrates when using the sacrificial layers. In this case the graphene will not be directly held by the sacrificial layer, but it will be attached partially to the residues which lead to crack and torn parts in the graphene layer.

To maximize the adhesion between the PIB surface and PDMS surface, the graphene/Cu samples were carefully handled without causing any folds during the lithography process as seen in **figure 3.6a**. This helped to attach a PDMS stamp to the Cu coated with PIB as shown in Figure 3.6b leaving enough space at the edges of the stamp. The quality of the contact between PDMS and PIB was checked visually under the optical microscope which revealed no air gaps in the interlayer. The graphene ribbons were successfully transferred onto the 1.2 mm thick PIB-PDMS stamp after etching the Cu foil. The oxidized Cu foils caused by graphene RIE etching took longer time to be etched in the $FeCl_3$ solution and the etching process was not fully completed. We found these residues contaminated the bottom graphene on the final substrate. Any sample with oxidized surface was discarded at this stage.

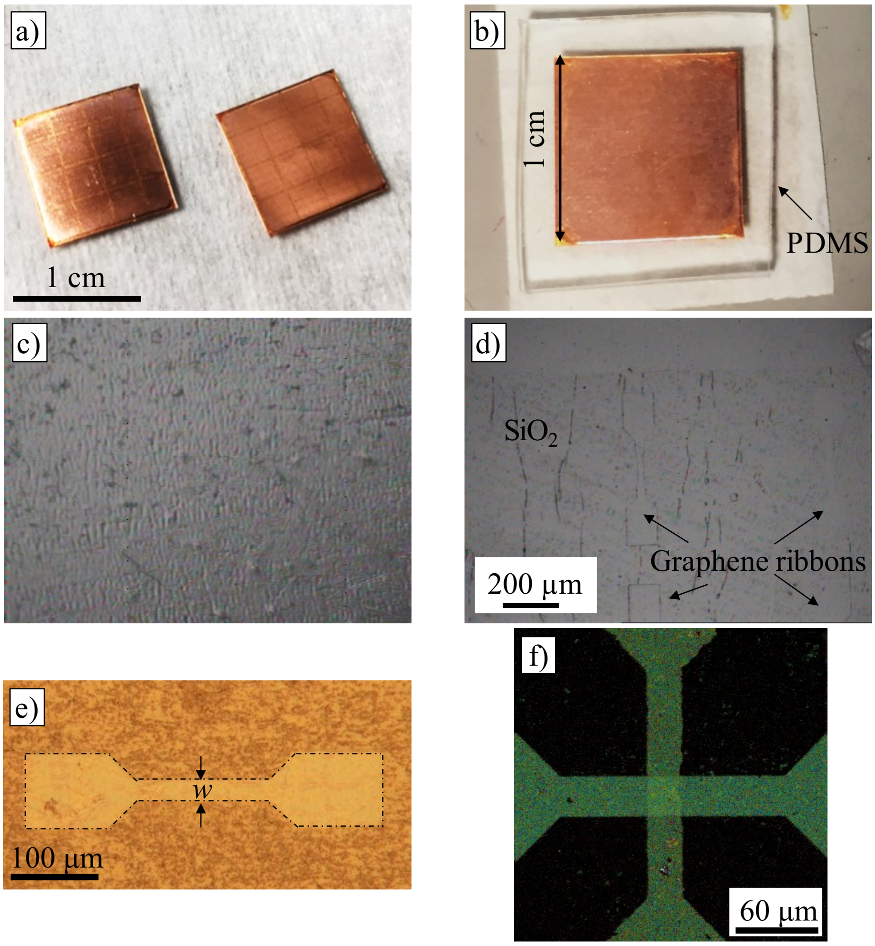

Figure 3.6: a) A digital photo of Cu foils after etching the unwanted graphene that shows the clear surface of the Cu foils where the patterns of the photoresist covering the graphene ribbons are seen by the naked eyes. **b)** A digital photo showing how the PDMS was attached to the graphene/PIB/Cu stack leaving a space around the copper foil to be held by the glass slide later. The residues of the photoresist in the corners were wiped out by acetone. **c)** Micrograph of graphene transferred onto PIB/PDMS stamp after etching the Cu foil. No ribbons were located under the microscope. **d)** Micrograph of the graphene transferred onto PIB/ PDMS stamp utilizing SiO_2 layer around the graphene ribbons. **e)** Coloured micrograph of one graphene ribbon transferred onto PDMS stamp**. f)** Confocal laser scanning microscopy image (λ = 950 nm) of the active region of the device showing the overlap region of the two graphene ribbons over a 30 x 30 μm^2 area, representing the tunnelling junction.

Another observation after etching the Cu foils was that the thickness of the PDMS stamp has impact on the outcomes of the graphene transfer onto the PIB/PDMS stamps. Different PDMS stamps of different thicknesses were tested. We found that the stamp thickness is a critical factor since stamps thinner than 0.7 mm did not maintain the shape of the graphene bars and are tricky to handle due to higher flexibility. Stamps thicker than 1.4 mm reduced the visibility of the graphene electrodes observed through the PIB/PDMS layer. Also, thicker stamps were not very useful when fitting the sample in the mask aligner due to the limited space between the sample holder and the stage of the mask aligner.

After etching the Cu, the graphene ribbons were not easily seen under the microscope of the mask aligner without the SiO_2 layer (Figure 3.6c). Yet, these graphene ribbons were easily observed with a 30 nm thick layer of SiO_2 that enhanced the contrast of the edges of the top graphene electrodes and facilitated the alignment process before stamping (Figure 3.6d). Magnified graphene ribbon transferred onto a PDMS stamp is shown in Figure 3.6e. The excellent adhesion of PIB to graphene electrodes resulted in transferring the graphene with a success rate of ~80 % for the self-assembly process. Using a different polymer like PMMA is not possible in this technique because PMMA is not adhesive and needs be heated up to 165 °C to soften the polymer in order to peel it off the PDMS. The transfer resulted in aligning the top electrodes with the bottom electrodes as shown in Figure 3.6f which complete the self-assembly of the flexible tunnelling device depicted schematically in Figure 3.1a.

The fabrication process may be iterated as many times as necessary to construct van der Waals superlattices alternating graphene and organic monolayers. Adapting our process to fabricate the self-assembled devices on transparent substrates is possible if needed. For example, it may be implemented on flexible polyester films (PEN) provided the bottom graphene ribbon is transferred from copper substrate to PEN as we have done for the top graphene electrode (Figure 3.3). This will help to locate the electrodes on the transparent substrates thanks to the SiO_2 layer surrounding the electrodes. This process might require one to reduce the thickness of the insulating layer to enhance the contrast while not affecting the height of the tunnelling junctions.

3.4 Conclusion

We used a bottom-up process to pattern graphene sheets into arrays of graphene ribbons on SiO_2/Si and Cu substrates that were free of obvious photoresist residues. The top graphene ribbons were transferred to a two-polymer flexible stamp made of PIB and PDMS polymers acting as intermediate substrate allowing us to deposit the NDI-Py molecules and drop cast the metal catalyst before completion of the device. The deposition of insulating layer around the graphene electrodes assisted to locate them on PIB-PDMS stamp during the alignment process which yield a precise alignment of the device and ease the self-assembly process. The process is the first to use molecular self-assembly as a tunnel layer and to combine bottom up molecular self-assembly with top down lithography.

4 Structural Properties of the Self-assembled Device

The adsorption process of the NDI-Py molecules on graphene and the molecular configurations were validated by Raman Spectroscopy and STM. Besides, XPS was employed to assess the chemical structure of the Ag bonds with the molecules adsorbed on the graphene ribbons. This enabled the identification of changes in stoichiometry and coordination introduced by the catalyst independently of the chemical species already present in the substrate and NDI molecules. The investigations of the structural properties have been done at intermediate stages of completion and on the final devices.

4.1 Raman spectroscopy

Raman spectroscopy (Renishaw inVia System, wavelength 532 nm, 0.7 mW) was carried out to investigate the change in phonon spectra induced by the adsorption of NDI-Py molecules on a graphene monolayer. All Raman spectra were taken after patterning the graphene to eliminate the changes in the spectra that might have occurred due to the transfer process of the graphene which could affect analysis of the NDI-Py deposition.

4.1.1 Sample Preparation

We prepared graphene ribbons with and without the NDI-Py molecules. Then, we fabricated a device without any molecules between the graphene electrodes (G/G), and a complete device (G/NDI-Py-Ag-NDI-Py/G) by the same methods mentioned in chapter 3. All samples were on SiO_2/Si substrates.

4.1.2 Raman spectrum of graphene functionalized with NDI-Py

The Raman spectrum taken by directing the laser spot at the centre of individual graphene ribbons on SiO_2/Si substrate is shown in **Figure 4.1**. This plot revealed the unique vibration modes of a monolayer graphene sheet represented by the 2D peak at 2671 cm^{-1} resulting from the doubly inter-valley resonant scattering process, and the G peak at 1582 cm^{-1} resulting from first order Raman scattering as an in-plane stretching vibration mode of C–C bond of graphene. The third main peak is the D peak observed at 1345 cm^{-1}

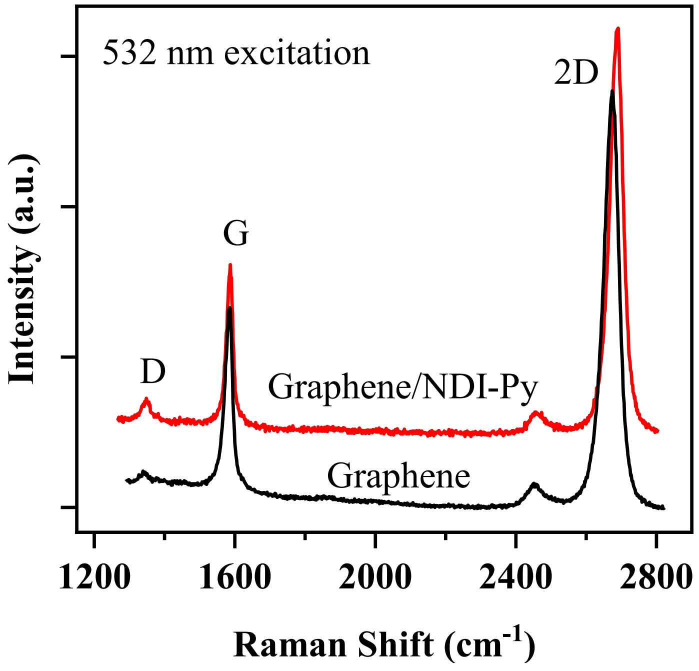

Figure 4.1: Raman spectra a monolayer graphene ribbon patterned on a SiO_2/Si substrate (black line) compared to a monolayer graphene ribbon functionalized with NDI-Py (red line). Curves are shifted upward for clarity.

which is activated by the presence of defects in the graphene causing a breathing mode for the carbon rings of graphene.[68-69, 82-85] These peaks are at slightly higher frequencies due to the unintentional doping introduced during the fabrication of graphene ribbons compared to peaks reported in other studies.[45, 48, 68] Once we deposited the NDI-Py molecules on the graphene ribbon, the spectrum revealed the 2D, G, and D peaks which are the same ones were observed in the graphene-only spectrum. Yet, the G and 2D peaks of the monolayer graphene were blue-shifted to higher frequencies by 14 cm^{-1} to 2685 cm^{-1} for the 2D peak and by 3 cm^{-1} to 1585 cm^{-1} for the G peak, due to the p-type doping introduced by the electron deficient NDI cores of the molecules while the D peak did not shift.[86-87] For the p-doping to occur, the NDI-Py core must lie flat on the graphene surface as a result of the local polarization of graphene induced by electron deficient molecules absorbed on its surface. It is possible some residues could induce some strain that might contribute to the shifts observed in the Raman peaks.

The concentration of the p-doping n_p is estimated from the shift in the G peak due to the adsorption of the NDI-Py molecules according to the formula [88]:

$$n_p = \pi(\frac{\Delta E_F}{\hbar v_F})^2 \, , \tag{4-1}$$

where ħ is the reduced Plank`s constant, v_F is the Fermi velocity, and ΔE_F is the shift of the Fermi level (with respect to the Dirac point) given by [89-90]:

$$\Delta E_F = \frac{\omega_G - \omega_{Go}}{42\ (cm^{-1}/eV)} \, , \tag{4-2}$$

where ω_G is the of the G peak frequency after depositing the molecules and ω_{Go} is the G peak frequency of graphene without the molecules (1582 cm^{-1}).

Given that the G peak was shifted by 3 ± 0.2 cm^{-1} as in Figure 4.1, the NDI-Py molecules shifted the Fermi level by 0.071 meV hence the doping introduced by NDI-Py molecules was ~ 3.6 $\times 10^{+12}$ cm^{-2}. The p-doping concentration will be investigated further in chapter 5 where we study the electrical measurements of the self-assembled devices.

4.1.3 Raman modes of NDI-Py in the tunnelling junction

As a control sample we acquired the Raman spectrum from the device without the molecules (Graphene/Graphene samples), shown in **Figure 4.2** (black curve). This spectrum appeared identical to the Raman spectrum of pristine monolayer graphene as in section 4.1.2. When we focused the laser beam at the centre of the tunnelling junction, we observed new peaks at 1414 cm^{-1}, 1459 cm^{-1}, and 1712 cm^{-1} corresponding to the stretching modes of C-C bonds, C=C and the carbonyl C=O of the imides, respectively (Figure 4.2, red curve).[91-92] Because the naphthalene core is the only part of the molecule that possesses carbonyl oxygens, the extra Raman peaks confirm that the naphthalene cores are on the graphene surface suggesting that they interact through van der Waals interactions. The additional peaks observed were not clear in the sample graphene/NDI-Py shown in Figure 4.1 due to the low possibility of detecting a monolayer of these molecules. This was interpreted this way as we started to observe these peaks when we have the molecules on both graphene electrodes.

The appearance of the molecules on the graphene surface also affected the intensity ratio of the 2D peak to the G peak I_{2D}/I_G and the ratio of D peak to the G peak I_D/I_G when compared with the device without the molecules. For the monolayer graphene without NDI-Py molecules, the ratio I_{2D}/I_G was found to be 2.3 while this ratio is 2.5 for a monolayer graphene with NDI-Py molecules as a result of the doping. The ratio I_D/I_G for graphene without the NDI-Py was 0.04, which is very close to the expected value for pristine graphene suggesting that the graphene surface has very low residues.[86, 93] This ratio increased after doping with NDI-Py molecules and was found to be 0.12. This suggests that naphthalene slightly perturbs the graphene lattice implying again that the NDI cores exist on the graphene.

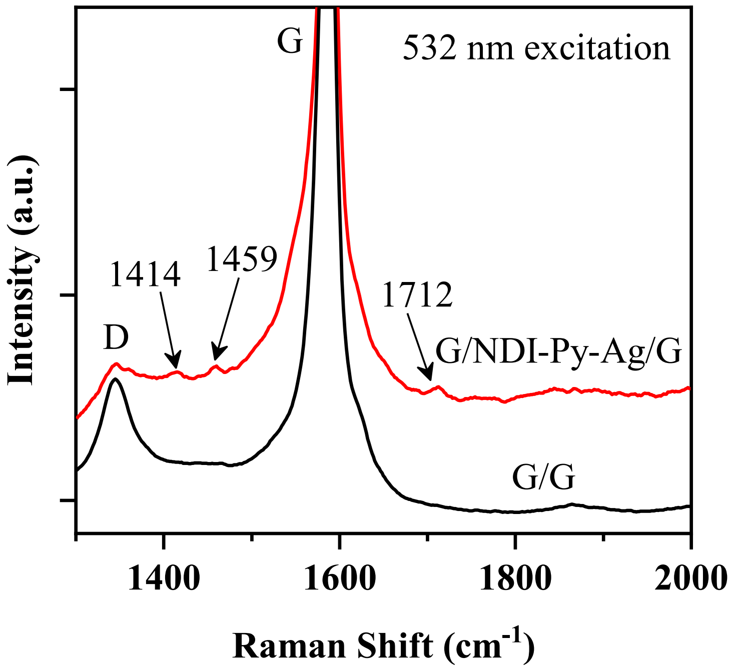

Figure 4.2: Raman spectra taken at the centre of the tunnelling junction G/NDI-Py-Ag-Py-NDI/G bridges (red line) and when the two graphene ribbons are in direct contact with one another (black line). The vibration modes induced by the NDI-Py are at 1414 cm^{-1}(C-C bonds), 1459 cm^{-1}(C=C bonds), and 1712 cm^{-1} (C=O bonds). The red spectrum is shifted up for clarity.

4.2 Molecular conformation of NDI-Py on HOPG probed by STM

The self-assembly patterns of NDI-Py molecules on Highly Oriented Pyrolytic Graphite (HOPG) was investigated by STM to assess the suitability of the organic layer as a tunnelling barrier which must be pinhole free and have constant thickness. The local density of states (LDOS) of the molecule was computed at different energy levels corresponding to different bias voltages between the STM tip and the molecules. We used density functional theory (DFT) to investigate the lowest unoccupied molecular orbitals (LUMO) and the highest occupied molecular orbitals (HOMO) molecular orbitals of the molecules The LDOS maps allowed us to relate the STM images taken at different substrate bias levels to individual electronic orbitals. In this section, we present the experimental procedures to prepare the samples, the STM images of different supramolecular patterns of the tunnel monolayer and discussions of molecular imaging the of NDI-Py.

4.2.1 Experimental procedures

To test the adsorption geometry of the DNI molecules used in our work, we evaporated the molecules on a mechanically cleaved smooth surface of HOPG for better resolution instead of graphene on SiO_2 due to the surface roughness of the dielectric material. The STM was set in the constant current mode to avoid the possibility of affecting the geometry of the standing side chains of the molecules and to get better resolution. Parameters: V= 1.87V , I = 10 pA, V= -1.69 V, I = 10 pA, Temp. = 77 K. The substrate voltages correspond to image the different molecular configurations.

4.2.2 Calculating the local density of states at different tip bias levels

The density functional theory DFT of the NDI-Py molecules geometry was optimized using the B3LYP exchange-correlation functional [94] and the 6-311G basis set [95] in Gaussian 16 software.[96] The molecule was allowed to fully relax until a threshold for the average force on atoms of 5×10^{-4} eV/Å was reached.

4.2.3 Self-organisation of NDI-Py molecules on HOPG

High resolution STM images were obtained by biasing the substrate positively with respect to the STM tip (**Figures 4.3a and 4.3b**) or negatively with respect to the tip (**Figures 4.3c and 4.3d**). The NDI cores of the molecules interact with the HOPG via van der Waals interactions, and they also interact via hydrogen bonds with next neighbouring molecules. The molecules are expected to self-assemble according to one of the lattice structures shown in **Figure 4.3e**.[97] Structures 1 and 3 in Figure 4.3e are not favourable due to the repulsive interaction of the C-H···H-C bonds (dotted circles), but structures 2 and 4 (dotted lines) are favourable due to the attractive interaction between the C-H of the core in one molecule and O=C bonds in a neighbouring molecule. When positively biasing the substrate, a self-assembly pattern of NDI-Py was revealed with unit cell a =1.1 nm, b = 3.82 nm and γ = 97°, on which we have superimposed the proposed molecular assembly (Figure 4.3a). The NDI cores coincide with the dominant bright spots as seen in Figure 4.3b. At positive voltage, the DFT calculations of the NDI-Py show that the LUMO or LUMO+1 dominate the local densities of states of the molecules and are localized on the NDI cores (Right panel, **Figure 4.4a**) which are represented by the bright spots in Figure 4.3a and 4.3b. These bright spots indicate that the in-plane molecular pattern was achieved where the nearest neighbour molecules were offset by ~ 4.2 Å along their long axes and in agreement with structure 4 in Figure 4.3e.[97] The observed molecular configuration is stabilized by the attractive C-H···O=C interactions between the cores of the NDI-Py.[23, 74, 98-99]

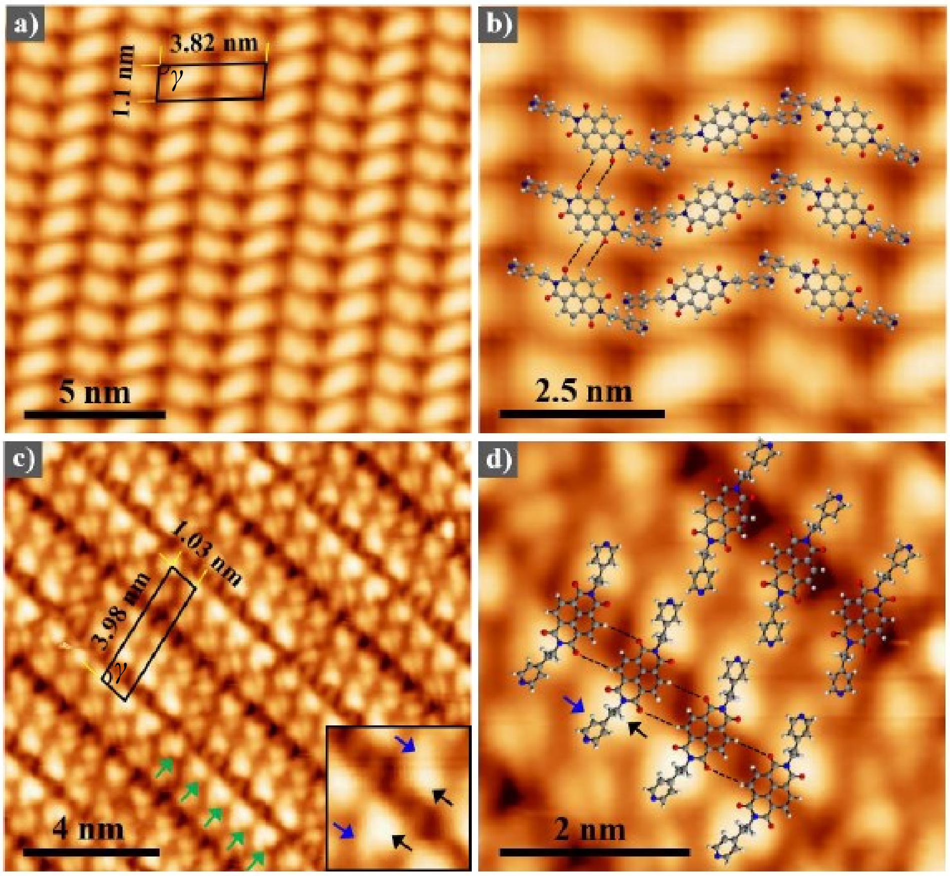

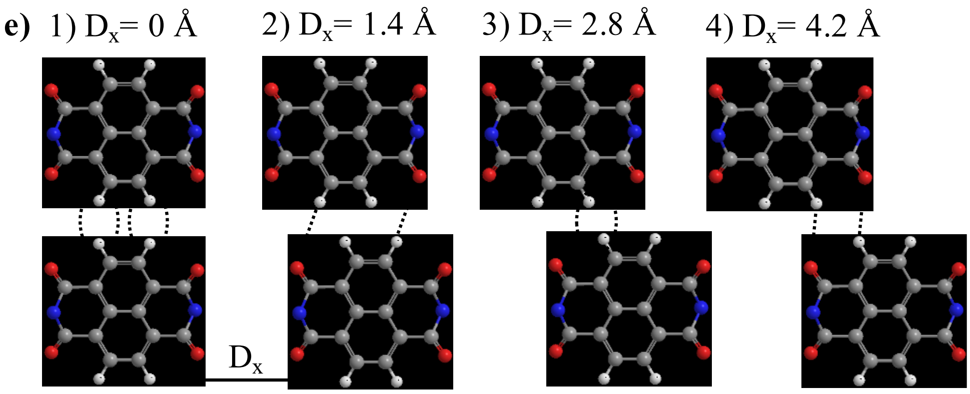

Figure 4.3: Low temperature STM images of the NDI-Py adsorbed on HOPG and self-assembly molecular structures of the NDI-Py cores. The molecules appear with bright ends or bright bodies depending on the bias voltage applied to the samples with respect to the STM tip. **a)** Tightly packed lattice of NDI-Py molecules self-assembled on HOPG obtained under positive voltage applied to the substrate at 77K (V= 1.87 V, I = 10 pA). NDI cores appear brighter with a unit cell a = 1.1 nm, b = 3.82 nm and γ = 97°. **b)** Magnified view of the unit cell in figure a) where it is superimposed with the molecular arrangement of NDI-Py self-organised by hydrogen bonds (C-H···O=C) bonds (dashed lines) where each neighbouring molecule is offset by ~ 4.2 Å. **c)** STM of the molecules imaged at negative bias voltage at 77K in a different location in the sample where the pyridinic endings (Inset, blue arrows) and the pivoting groups (Inset, black arrows) appear as bright spots at V= -1.69 V and constant current I = 10 pA. The unit cell lattice parameters: a = 1.03 nm, b = 3.98 nm and γ = 101°.**d)** Magnified view of the unit cell observed in figure c) superimposed with an NDI-Py molecular arrangement stabilized by hydrogen bonds (C-H···O=C) between the neighbouring molecules where each molecule is offset by ~1.4 Å. **e)** In-plane molecular arrangements of the NDI molecules. Structures 1 and 3 are not favourable due to the increase in the repulsive interactions between the hydrogen atoms of the cores (dotted lines) while structures 2 and 4 are favourable due to the increase in the attractive interaction between the C-H in one molecule and the carbonyl oxygen (C=O) in the neighbouring molecule (dotted circles). D_x is the offset. Figure (**e**) is adapted from: Kakinuma et al.[97]; ©2013 Royal Society of Chemistry.

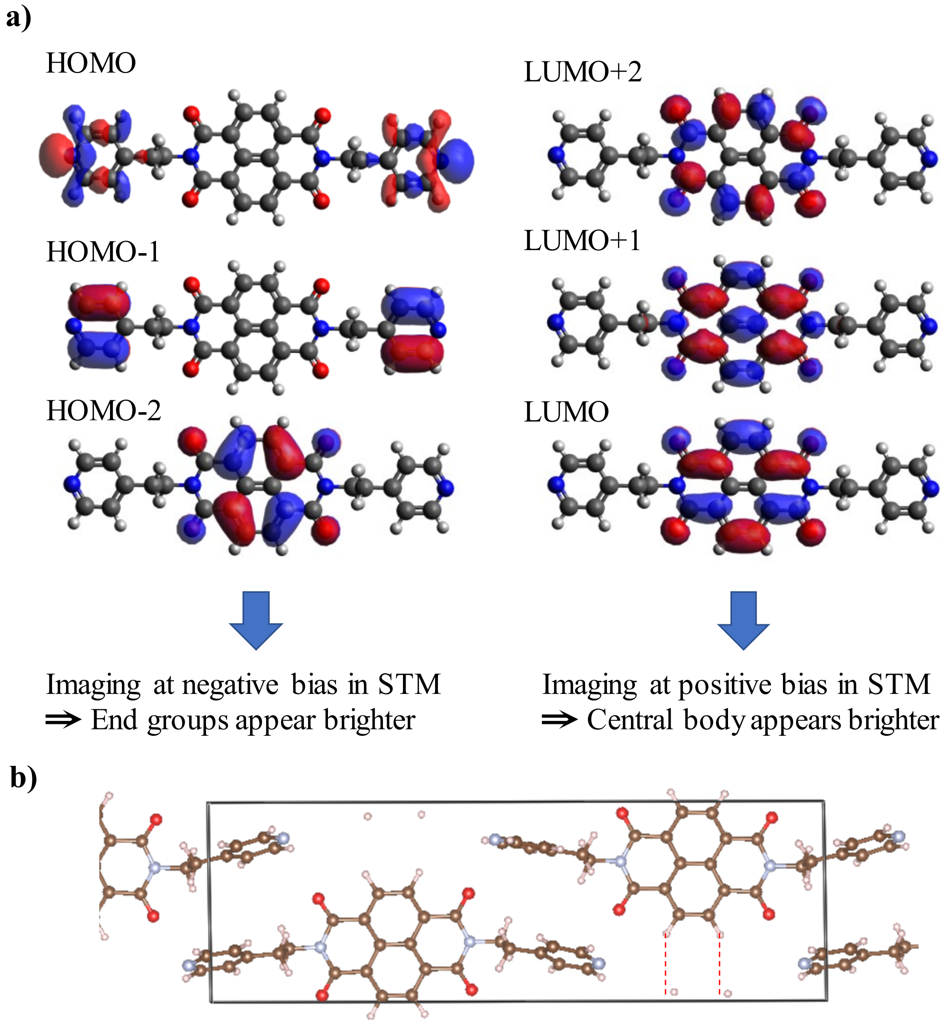

Figure 4.4: **a)** DFT simulations of the NDI-Py molecule in vacuum: geometry and electronic structure. Left panel: highest three occupied molecular orbitals of the optimized NDI-Py structure in vacuum (isodensity value 0.02 e/bohr^3). Right panel: lowest three unoccupied molecular orbitals (isodensity value 0.02 e/bohr^3). The energy levels of the molecular orbitals were found to be: -7.64 eV (HOMO-2), -7.55 eV (HOMO-1), -6.9 eV (HOMO), -4.11 eV (LUMO), -2.33 eV (LUMO+1), and -1.83 eV (LUMO+2), yielding a HOMO-LUMO gap of ~ 2.8 eV. The orbitals in the blue frames fall within the energy window around the HOMO-LUMO gap used in the STM experiments. **b)** Simulation of molecular conformation of the self-assembled monolayer showing the unit cell (black rectangle) showing the tendency of the pyridinic ends to come out the plane of the cores.

When imaging the sample at different locations, by now biasing the substrate negatively, the STM images revealed another self-assembly molecular pattern of the NDI-Py (Figure 4.3c). Applying a negative bias to the substrate allows imaging different parts of the NDI-Py molecules compared to the images obtained with a positive bias voltage shown in figure 4.3a. The DFT calculations show that when applying negative bias voltage (Left panel, **Figure 4.4a**) the local density of states of the HOMO and HOMO-1 are maximum at the sites of the pyridinic endings.

The negative bias images revealed the presence of bright spots that coincide with the pyridinic ends (black arrow in insets of Figures 4.3c and 4.3d) and their pivot articulations (blue arrow in inset of figure 4.3c and figure 4.3d). The NDI cores appeared dark in these images. The unit cell in this new configuration is a = 1.03 nm, b = 3.98, γ =101°. From Figure 4.3d, we found that the molecules are self-organised and offset by ~ 1.4 Å along their long axes and this molecular structure is consistent with structure 2 in Figure 4.3e.[97] This suggests that molecular configuration is also stabilized by the hydrogen-carbonyl oxygen interaction (C-H···O=C) and the reduction in the hydrogen-hydrogen interaction (C-H···H-C) between the neighbouring molecules. The contrast of the STM images is in broad agreement with STM studies on other non-planar NDI-based molecules.[74]

The two self-assembled patterns of the NDI-Py observed in figure 4.3a and 4.3c show that the cores of the NDI-Py lie flat on the HOPG substrate. Here, articulations of the (-N-CH_2-CH_2-C-) depend on compact packing of the molecules within the self-assembled domains. The two different configurations of the molecules are observed where the cores that are offset ~ 4.2 Å incorporate the Z-shape as in Figures 4.3a and 4.3b (depicted in Figure 3.1b), and the cores that are offset ~ 1.4 Å incorporate the U-shape as in Figures 4.3c and 4.3d (depicted in Figure 3.1b). The articulations of the spacers allow the π-π stacking between pyridyl groups of the adjacent molecules which also play a role in stabilizing the molecular structures. The possibility of the pinholes due to having the two isomers that result from the articulations of the spacers has not been examined. The simulation of molecular conformation in vacuum without the presence of graphene shows that, in a monolayer, the side groups tend to align with each other which induces their rotation around their own axes. They tend to come out of the plane that contains the molecule body (**Figure 4.4b**). This molecular conformation is not exactly the same as favourable configuration in Figure 4.3 (offset ~ 1.4 Å) but it is still favourable with smaller offset (red dashed lines, Figure 4.4b).

The spacers (-N-CH_2-CH_2-C-) rotate out of the plane because of the steric repulsions between the carbonyls and the CH_2 groups. The energy of rotation is very low in comparison with the coordinative bonds Py-Ag-Py (50-200 $kJ.mol^{-1}$), the π-π aromatic interactions, and the hydrogen-carbonyl bonds between the cores of the molecules (4-60 $kJ.mol^{-1}$).[100] It is possible that any small amount of interfacial stress could rotate the pyridinic endings out of the plane of the NDI cores. This is seen in Figure 4.3c where to accommodate this stress, the Py-endings lift out of the plane to different degrees, giving a periodic superstructure along one row of molecules (Figure 4.3c, green arrows). In the same way, the pyridinic would rotate out of the plane due to the highly energetic Py-Ag-Py bonds which facilitate constructing the molecular bridges between the graphene layers of the fully assembled device as depicted in Figure 3.1c (Chapter3).

The planar molecular conformation of the molecules on CVD graphene would be expected to orient along the crystal orientation of the graphene domains[101] as the CVD graphene is a multigrain structure of around 10 μm grain size.[40, 102] The multiple orientations of the molecules on the CVD graphene are not expected to perturb the planar conformation of the molecules.[101] It is also not expected to affect building the molecular tunnelling bridges because the side chain molecules attached to the NDI cores are able to rotate above the planes of the cores reaching other molecules on the top graphene.

4.3 X-ray photoelectron spectroscopy

4.3.1 Probing ion-dipole bonds with XPS

The goal here is to determine the filling fraction of pyridinic N-sites with Ag^+ ions. We first identify the K-absorption lines of the N, Ag, C, and O atoms from the survey spectra of the samples under study. Then, we acquire the high-resolution spectra of these main atoms in each sample we made to infer the nature of the local bonds from the shifts of these lines induced by their electronic environment. In particular, we investigate the changes in the chemical bonds of the NDI-Py on graphene before and after drop casting the $AgNO_3$. It is done by extracting the shifts (chemical shifts) in the core level binding energies of the constituent atoms of NDI-Py and $AgNO_3$ and observing the emergence of any new peaks in the spectra due to any new bonds. Then, we calculate the ideal atomic ratio of the filled sites of the pyridinic-N with Ag (bound with Ag) to the unfilled sites in order to extract the Ag filling fraction. This is done by using equation 2-30 to determine the number of the filled and unfilled sites of the pyridinic-N from the XPS spectra. In the ideal case, all the pyridinic sites are filled with Ag giving 100% filling fraction.

Then, we determine the nitrogen to silver (N:Ag) as two Ag ions bond with the two pyridinic nitrogen atoms of the NDI-Py molecules. When the chemical bonding takes place, each pyridine ending should be bound to one Ag ion through the lone pairs provided by the N of the pyridine molecule. Here, the total number of the N atom involved in the calculation is 4 (2 atoms from the NDI core and 2 atoms from the pyridinic endings) and the Ag atoms is 2. Therefore, the ideal atomic ratio of the pyridinic-N to Ag (pyridinic-N:Ag) is 1:1. This ratio is compared later with the experimental atomic ratio calculated from the amount of pyridinic-N and Ag, and this will be our reference to investigate the filling fraction further and the formation of molecular bridges clipping graphene layers together. The ratios are extracted from normalizing the areas under the relevant peaks by their photoemission cross section, considering a pure superficial surface (Equation 2-32).

The top graphene electrode was not included in this characterization in order to probe the stoichiometry and the changes in the chemical bonds of G/NDI-Py and $AgNO_3$ with XPS. Also, neither the C atoms nor O atoms were chosen to investigate the bonding process as these atoms were overestimated due to the air contamination.

4.3.2 Experimental procedures

4.3.2.1 Preparation samples for XPS

We prepared different samples for the XPS measurements to eliminate the possibility of including atomic species from the substrate in our analysis. The preparation process of the control samples is schematically shown in **Figure 4.5** which also depicts the expected molecular structures of the $AgNO_3$/NDI-

Py/G/glass, NDI-Py/G/glass and $AgNO_3$/NDI-Py/glass samples. The graphene sheets were wet transferred from the Cu substrates onto glass

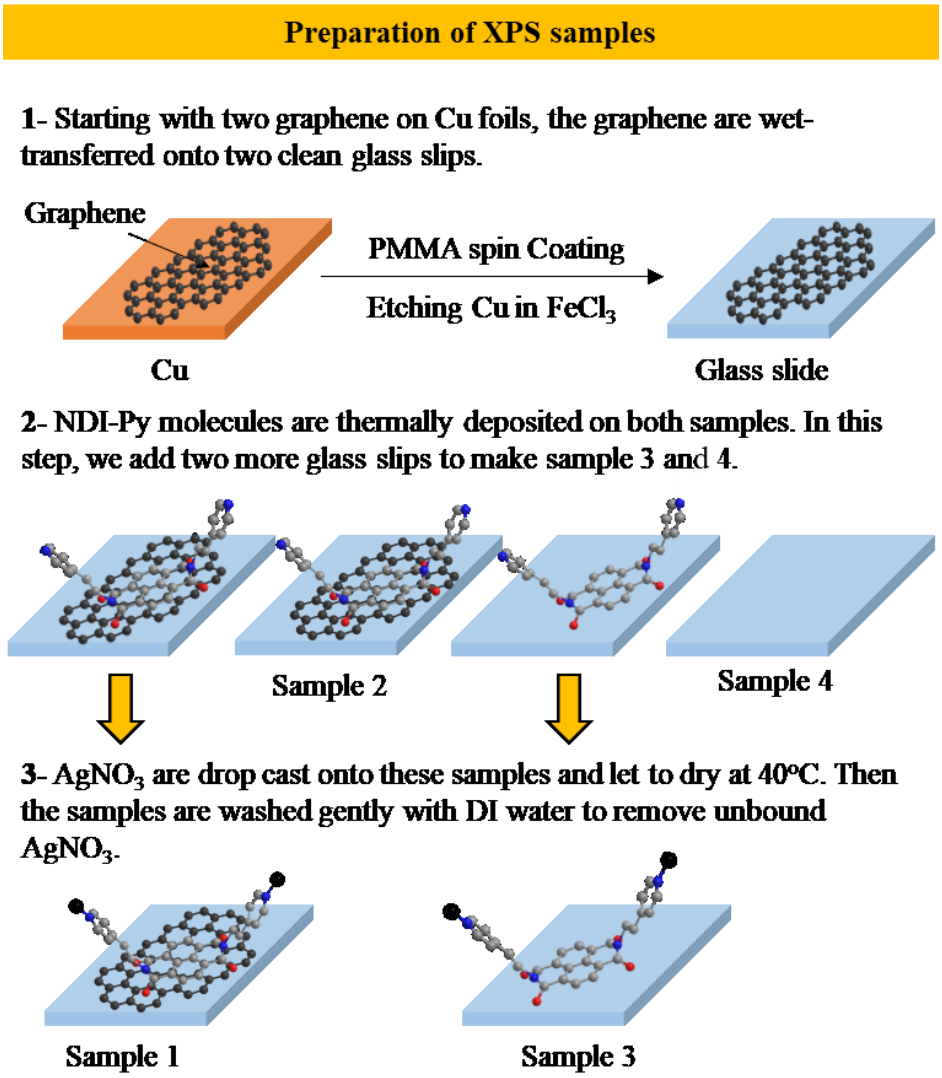

Preparation of XPS samples

1- Starting with two graphene on Cu foils, the graphene are wet-transferred onto two clean glass slips.

2- NDI-Py molecules are thermally deposited on both samples. In this step, we add two more glass slips to make sample 3 and 4.

3- $AgNO_3$ are drop cast onto these samples and let to dry at 40°C. Then the samples are washed gently with DI water to remove unbound $AgNO_3$.

Figure 4.5: Schematics of the preparation process of the XPS samples where the graphene is wet transferred. The Cu etching process is presented in section 3.2.2. All the cover slips are of the same size and the deposition of the NDI-Py are done at the same process. Where $AgNO_3$/NDI-Py/G/glass (Sample 1), NDI-Py/Graphene/glass (Sample 2), $AgNO_3$/NDI-Py/glass (Sample 3), and glass slide (Sample 4).

substrates with PMMA. Sample 1 is a thin film of NDI-Py molecules on a CVD graphene coated with $AgNO_3$ on a glass substrate instead of SiO_2 substrate to distinguish bonding layer and coordination from the substrate, O, and N species in XPS. Our control samples include NDI-Py/Graphene (NDI-Py/G) on a glass slide (Sample 2), NDI-Py on a glass slide spin coated with $AgNO_3$ (Sample 3), and a bare glass slide (Sample 4). The spectrum of sample 4 (glass substrate) is acquired as a control sample to eliminate the contribution of the substrate to the analysis of the chemical structures of samples. Ultra-High Vacuum UHV and Argon sputtering to clean the samples before the measurements were avoided to preserve the organic molecules hence the goal is to investigate the Ag-N bonding.

4.3.2.2 Acquisition parameters

A Kratos AXIS-HS XPS at the NANOESCA facility in University of Bristol was used where the source of the excitation is monochromatic Al kα x-rays with known emitted photon energy 1486.6 eV. First, a survey spectrum for each sample is obtained for element identification in the range of 0 – 1200 eV, the pass energy, where the analyser in the XPS device operates as an energy window, is 50 eV and the step size is 0.5 eV. Then, detail scan spectra (high-resolution spectra) are obtained for the selected peaks that correspond to the elements in the samples where the pass energy is 20 eV which is fixed for constant energy resolution. Each detail scan spectrum of each element in any sample should include the background of each side of the selected well-defined peak. Also, the step size should be small enough to determine the precise position of the main peak. Therefore, the step size is chosen to be

0.05 eV. The following tables display the details of the acquisition parameters of samples (**Table 4.1**) and the sensitivity factors of the elements (**Table 4.2**).

Table 4.1: The XPS acquisition parameters of four samples

Spectrum Sample 1	Start E_B (eV)	End E_B (eV)	Step (eV)	dt (sec)	Number of scans	Pass energy (eV)
Survey	1200	0	-0.5	0.25	4	50
O1s	542	520	-0.05	0.5	3	20
N1s	412	390	-0.05	0.5	8	20
Ag3d	383	361	-0.05	0.5	8	20
C1s	298	276	-0.05	0.5	5	20
Si2p	109	92	-0.05	0.5	5	20

Spectrum Sample 2	Start E_B (eV)	End E_B (eV)	Step (eV)	dt (sec)	Number of scans	Pass energy (eV)
Survey	1200	0	-0.5	0.25	4	50
O1s	542	520	-0.05	0.5	5	20
N1s	412	390	-0.05	0.5	10	20
C1s	298	276	-0.05	0.5	5	20
Si2p	109	92	-0.05	0.5	6	20

Spectrum Sample 4	Start E_B (eV)	End E_B (eV)	Step (eV)	dt (sec)	Number of scans	Pass energy (eV)
Survey	1200	0	-0.5	0.25	4	50
O1s	542	520	-0.05	0.5	4	20
C1s	298	276	-0.05	0.5	5	20
Si2p	109	92	-0.05	0.5	6	20

Spectrum Sample 3	Start E_B (eV)	End E_B (eV)	Step (eV)	dt (sec)	Number of scans	Pass energy (eV)
Survey	1200	0	-0.5	0.25	4	50
O1s	542	520	-0.05	0.5	3	20
N1s	412	390	-0.05	0.5	8	20
Ag3d	383	361	-0.05	0.5	7	20
C1s	298	276	-0.05	0.5	4	20
Si2p	109	92	-0.05	0.5	4	20

Table 4.2: The sensitivity factors of the elements in the samples

Element and transition	Sensitivity Factor
O 1s	0.00473956
N 1s	0.00290818
Ag 3d	0.0255278
C 1s	0.00161816
Si 2p	0.0011035

4.3.3 Results of XPS measurements

4.3.3.1 Identifying photoelectron lines of main elements

XPS survey spectra were acquired from the control samples to identify the photoelectron lines corresponding to the atoms present where these lines are represented as peaks in the spectra. **Figure 4.6** shows the peaks of the spectrum of sample 1 (G/NDI-$AgNO_3$) reveals the existence of C at 284.8 eV, N at 400.7 eV, Ag at 368.2 eV and 374.2 eV with a doublet separation of 6 eV, and O (532.5 eV).[80] Similar peaks are observed in sample 2 (G/NDI) and sample 3 (NDI-$AgNO_3$) except that sample 2 lacks the Ag peaks as this sample was not coated with $AgNO_3$. Sample 2 has weak peaks of Cu at 693 eV, Fe at 837.5 eV and Cl at 7 eV [80] arising from the wet transfer residues of etching the Cu substrate and these peaks are of very low intensities in sample 1. The electronic environments of the atoms are going to influence the observed X-ray absorption lines involving the core level transitions. The perturbations by these environments are what you we use to determine the fraction of adsorbed Ag ions on the pyridinic sites as discussed in the next section.

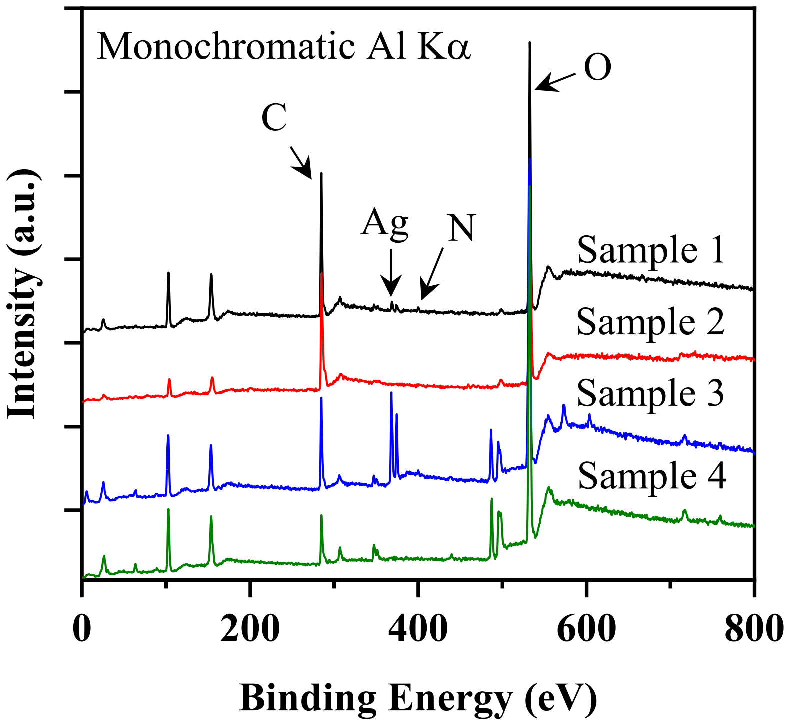

Figure 4.6: XPS survey spectra of the samples showing the four main peaks representing the constituent atoms of the tunnelling barrier. The spectra were taken in steps of 0.5 eV with pass energy 50 eV with monochromatic Al Kα source. The curves are shifted up for clarity and C peak is set at 284.8 eV. The N peak in sample 2 was only observed in the detailed spectrum of sample 2 while the N peak in sample 4 was not distinguishable from the noise of the survey spectra due to avoiding the UHV process.

4.3.3.2 The fraction of pyridinic ends forming ion-dipole bonds

High resolution spectrum of nitrogen was acquired from each sample to study how the binding energy of N is modified when we drop cast $AgNO_3$ on the NDI-Py to form the coordinative bond Ag-N (**Figure 4.8**).The photoelectron peak of the nitrogen atom of sample 2 (G/NDI-Py) (Figure 4.8a) is deconvoluted into a main imidic-N absorption line at 400.4 eV associated with the O=C-N-C=O molecular environment, and a red-shift pyridine-N line at 399.0 eV associated with the C-N-C bonds.[80] The relative amplitude of N peaks shows that sample 2 has more imidic-N than pyridinic-N. As we drop cast $AgNO_3$ onto the NDI-Py on graphene (Sample 1), a third nitrogen peak appeared at 399.7 eV which arises from Ag-pyridinic-N bonds (Figure 4.8b, purple line). The electron density around pyridinic-N decreases when establishing the Ag-N bonds which has the effect of blue-shifting the pyridinic-N peak relative to its unbound state. Obviously, not all pyridinic-N sites are filled with an Ag atom since we observe both filled (Figure 4.8b, purple line) and unfilled pyridinic sites (Figure 4.8b, green line). The imidic-N and pyridinic-N peaks are also observed at the same binding energy in sample 3 (Figure 4.8c) and sample 1 (Figure 4.8b) confirming that Ag-N bonds are not affected by substituting the graphene substrate with a glass substrate. This is because Ag atoms cannot bind to the imidic-N atoms due to the impossibility of transferring away electrons from the C-N-C covalent bonds to form Ag-N bonds. In both sample 1 and 3, no trace of NO3- were found in the spectra. The NO3- line would appear at 407.5 eV.[103]

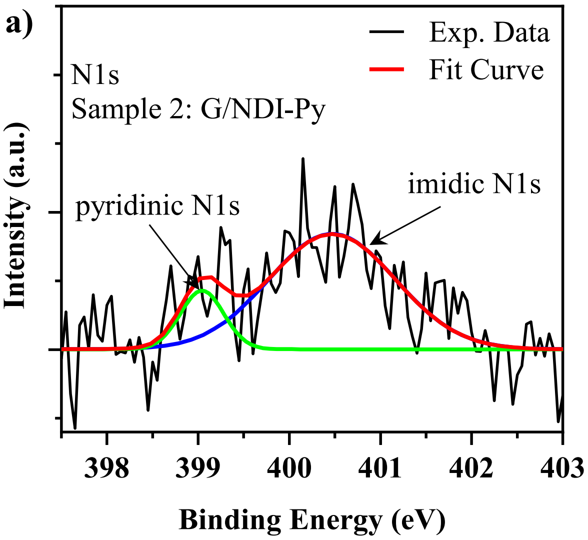
a)
N1s
Sample 2: G/NDI-Py
Exp. Data
Fit Curve
pyridinic N1s
imidic N1s
Intensity (a.u.)
398
399
400
401
402
403
Binding Energy (eV)

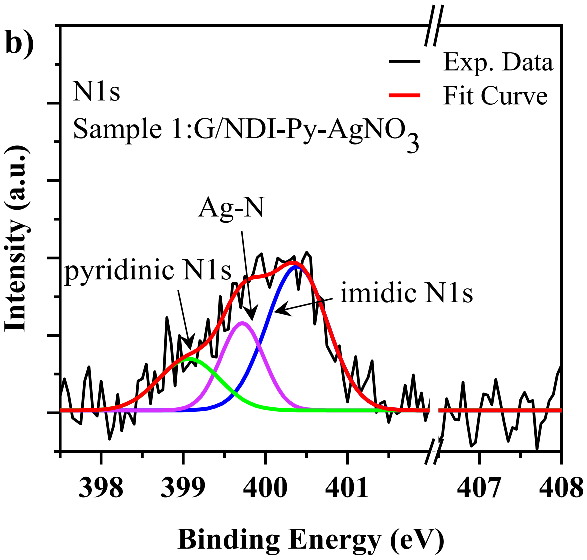
b)
N1s
Sample 1:G/NDI-Py-AgNO3
Exp. Data
Fit Curve
Ag-N
pyridinic N1s
imidic N1s
Intensity (a.u.)
398
399
400
401
407
408
Binding Energy (eV)

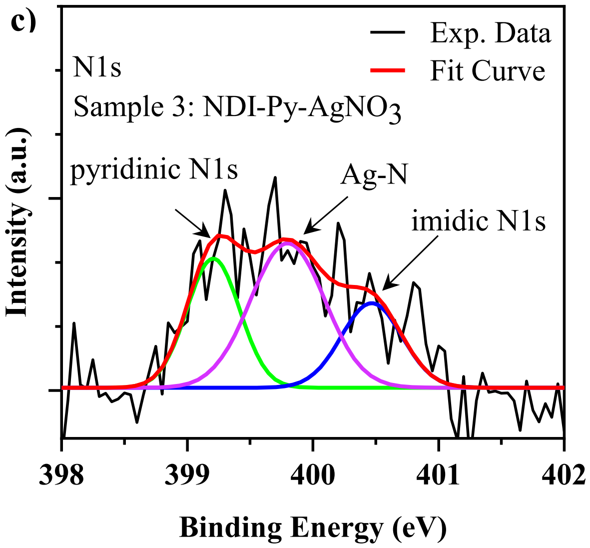

Figure 4.8: High resolution XPS spectra of nitrogen atom in sample 1, sample 2, and sample 3. **a)** Photoelectron peaks of N atom in sample 2 (black line) and fit (red line). The deconvolution of the spectrum reveals two peaks. One peak is at 400.4 eV (blue line) and is associated with imidic-N and another peak is at 399.0 eV (green line) and is associated with pyridinic-N. **b)** Spectrum of the N peak in sample 1 (black line), and fit (red line). The deconvolution of spectrum reveals three peaks at 400.4 eV, 399.7 eV and 399.1 eV corresponding to imidic-N (blue line), nitrogen in Ag-N bonds (purple line), and pyridinic-N (green line), respectively. **c)** Spectrum of N atom in sample 3 (black line), and fit (red line). The deconvolution of the spectrum reveals the presence of three peaks at 400.4 (imidic-N, blue line), 399.1 eV (pyridinic-N, green line) and at 399.7 eV (nitrogen in Ag-N bonds, purple line) in the absence of graphene. Here the fact that imidic and pyridinic are not balanced here is due to the high possibility that the molecules are not forming one layer on the glass surface.

High resolution spectra of Ag in sample 1 and sample 3 were acquired to investigate the coordinative bonds Ag-N (**Figure 4.9**). The spectrum of Ag in sample 1 (**Figure 4.9a**) exhibits two main peaks at the binding energies 368.2 eV and 374.2 eV (green line) corresponding to the spin-orbit doublet of $3d_{5/2}$ and $3d_{3/2}$ of metallic silver. Based on the deconvolution of Ag spectrum, we observed two pairs of peaks at 368.4 eV (blue line) and 374.5 eV (purple line) standing for the Ag-Pyridine-N bonds [80, 104]and Ag-clusters respectively without any presence of oxidized Ag (Ag-O) (Figure 4.9a). The photoelectron peaks of the Ag-N line remained at the same binding energies when NDI molecules stood on a glass substrate (Figure 4.9b) which validate the previous observations that Ag`s bind to pyridinic endings. These, unlike imidic endings, are unaffected by the choice of substrate material.

By extracting the areas under the nitrogen peaks which represent the number of the atoms found in in sample 1 (Figure 4.8b) and using equation 2-30 and the parameters in **Table 1** and **Table 2**, we first found that approximately half of the nitrogen atoms were imidic (Figure 4.8b, blue peak) and the other half were pyridinic (Figure 4.8b, green and purple peaks). This agrees with the stoichiometry of the NDI-Py molecules (Figure 2.6 in chapter 2) as there is one imidic nitrogen atom for each pyridinic atom in one NDI-Py molecule. We found from the spectrum of N that the ratio of filled pyridinic sites (bound with Ag) (area under the purple line) to the total number of pyridinic sites (areas under green + purple peaks) gives an Ag filling fraction of pyridinic sites of 65%.

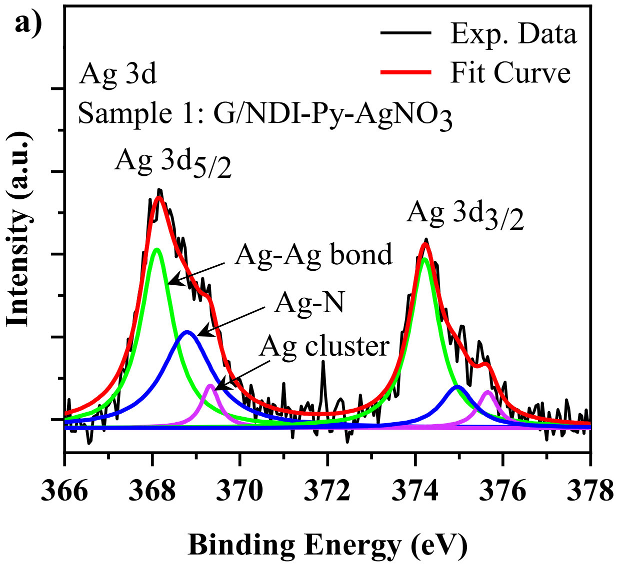

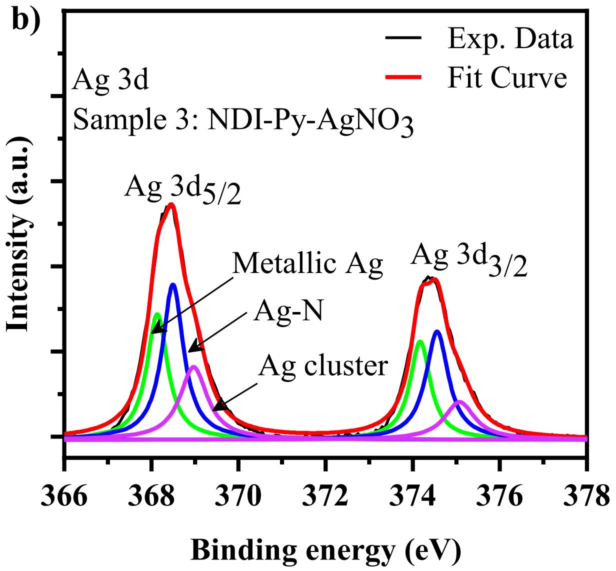

Figure 4.9: High resolution XPS Spectra of Silver atom in sample 1 and sample 3. **a)** Photoelectron peaks of Ag in sample 1 (black line), and fit (red line). The deconvolution of the spectrum yields two main peaks at 368.2 eV ($3d_{3/2}$ peak) and 374.2 eV ($3d_{5/2}$) corresponding to metallic Ag (green line). The $3d_{5/2}$ peak has two more satellite peaks observed at 368.4 eV which arising from the formation of Ag-pyridinic N bond (blue line) and a third peak at 369.0 eV arising from Ag clusters (purple line). **b)** The XPS spectrum of Ag atom in sample 3 (black line) and fit (red line). The deconvolution of the spectrum yields three peaks at 368.2 eV, 368.4, and 369.0 for the $3d_{5/2}$ peak corresponding to metallic Ag (green), Ag atom in the Ag-N bond (blue line), and the Ag cluster peak (purple line), respectively. The sample has no graphene. The spectra were taken in steps of 0.05 eV with pass energy 20 eV with monochromatic Al Kα source.

Then, by using equation 2-30, we extracted the number of the Ag atoms that were bound with N in sample 1 to extract the atomic ratio of pyridinic-N to Ag (N:Ag) (Figure 4.9a). Here, we found that the normalized area of the blue peaks of the Ag spectrum in Figure 4.9a, representing the number of the Ag bound to N, was double of the normalized area under the peak of the total pyridinic N in sample 1 (green and blue peaks in Figure 4.9a), within sample

1. This means that the experimental ratio of pyridinic-N:Ag is 2:1. Theoretically we should have one pyridinic-N for each Ag in the structure of sample 1 (**Section 4.3.1**). Yet, when considering that 65% of the pyridinic N atoms participated in the chemical bond with Ag atoms as mentioned earlier, the actual experimental atomic ratio will be 1.3:1 which is reasonably close to the theoretical ratio(1:1).

To test the effect of the absence of the graphene layer on the Ag-N bonds, we found that the atomic ratio of pyridinic-N:Ag in sample 3 (NDI/$AgNO_3$), without graphene, (Figure 4.8c) was 1:3. This ratio is high as the molecules lack π-π interaction with the glass substrate which establishes different complex structures of the molecules leading to high concentration of silver without available pyridine N-sites (Figure 4.9b). This also could be seen from the unbalanced atomic concentration ratio of the pyridinic N to the imidic N as deduced from Figure 4.8c. Therefore, the presence of graphene as opposed to glass had the effect of anchoring molecular cores and setting the orientation of the ending so that as to maximize to probability of filling Pyridinic-N sites with Ag atoms. Based on the analysis above, the Ag filled 65% of the available pyridine-N sites allowing for molecular bridges to form between graphene ribbons.

4.4 Discussion

The NDI cores are able to interact and be adsorbed on the graphene surface via π-π interactions. These molecules interact with each other via hydrogen-carbonyl oxygen bonds (4-60 $kJ.mol^{-1}$) resulting in self-organising the molecules as seen in Figure 4.3a and Figure 4.3c.[100] These criteria are essential to make an organic tunnel layer free of pinholes with a lattice matching the graphene`s lattice. This is combined with the ability of the molecules to be adsorbed on the graphene surface via Van der Waals interactions without perturbing the lattice structure as seen from our Raman study. Occasionally, the staggered molecular arrangement of Figures 4.3c and 4.3d exhibits dislocation-like features. This can arise when a Z-shaped isomer occurs in a network of U-shaped molecules (Figure 3.1b). However, the bonding of the pyridinic-N to the Ag will not be affected by the presence of both isomers.

The N-Ag-N bonds are linear and highly energetic (50-200 kJ.mol^{-1})[100] and they subsequently force the pyridine endings of different molecules to align along the same symmetry axis. The thermodynamically favoured bonding configuration of NDI-Py molecules is one where molecules assemble in pairs where the two Py endings of one molecule link to the two endings of the other molecule. These so-called chelate ring closures have been observed in solution.[105-106] Molecules anchored on graphene would however be pinned in different positions and orientations relative to one another. Hence, the bonds favoured by thermodynamics might largely be inhibited by the fixed configuration set when aligning the top and bottom layer. It follows that the accordion-like pattern of Figure 3.1c is the most probable configuration of molecular bridges. In addition, the NDI-Py molecules are stable up to 300 °C. This makes the proposed van der Waals assemblies robust and chemically inert under the normal operating conditions of electronic devices.

4.5 Conclusion

We have shown that NDI-Py molecules doped the graphene ribbons and introduced additional peaks in the Raman spectrum of graphene which correspond to the Raman vibrational modes of the NDI-Py at 1414 cm^{-1}, 1459 cm^{-1}, and 1712 cm^{-1}. These peaks are the longitudinal modes of C-C bonds, C=C bonds and C=O carbonyl bonds in the NDI-Py molecules, respectively. Based on the G peak shifts to a higher frequency, the electron-deficient cores of the NDI-Py molecules shifted down the Fermi level by 71 meV and the holes concentration was ~ $3.7\times10^{+12}$ cm^{-2}. We also showed that the ratio I_D/I_G has increased due to slight perturbation of the graphene lattice suggesting that the molecules lay flat on the graphene. This analysis is confirmed by acquiring the low temperature STM images. The STM images showed that NDI-Py molecules self-organize into a quasi-crystalline 2D lattice through the hydrogen-carbonyl bonds between the neighbouring molecules, and these molecules cover the graphene surface with a pinhole-free monolayer. The images are maybe consistent with a possible arrangement in which the pyridinic endings attached to molecules are rising above the graphene surface due to the steric repulsion between the CH_2 groups and the carbonyl groups of the cores. The pyridines of the adjacent molecules are attracted to each other through π-π stackings which helped also in the self-organisation of the NDI cores. The orientation of these pyridines helps in promoting the Ag-N bond (coordinative bond). From the XPS study, we determined the fraction of Ag atoms attached to the pyridinic endings to form molecular bridges and it was estimated to be 65%. Ag was successfully bound to N in the pyridine sites allowing the bridging of the organic molecules, attached to the graphene ribbons, to act as a tunnelling barrier for the self-assembled graphene-based heterostructures.

5 Electric Transport through the Molecular Potential Barrier

In this chapter, we investigate the current-voltage *I-V* characteristics of the self-assembled heterostructure devices at room temperature (300 K) and at the liquid nitrogen temperature (77 K) in a probe station. The investigation includes extracting the tunnel barrier width of the devices, the existence of the thermo-activated current across the tunnelling junctions to examine the microstructural properties and measuring the dependence of the *I-V* curves on chemical potential of the bottom graphene electrode by applying back-gate voltage. Control samples were also studied: one omitting Ag+ hence ion-dipole bonds (G/NDI-Py/…/Py-NDI/G), and the other omitting both Ag+ and NDI-Py (G/…/G).

5.1 Set up

Tunnelling current flows across the junction when a bias voltage V_b is applied between the graphene electrodes. Then a back-gate voltage V_g is applied between the bottom graphene electrode and the back of the substrate (p-doped silicon) which allows to modulate the chemical potential of the bottom graphene and the top graphene and investigate the tunnelling current across the molecular junction. At 77 K, the samples are mounted on a stage which is fixed on a liquid nitrogen container. LabVIEW program was designed to control and acquire the measurements of the *I-V* curves. The self-assembled devices tested are of different cross-sections w = 15, 20, and 30 μm.

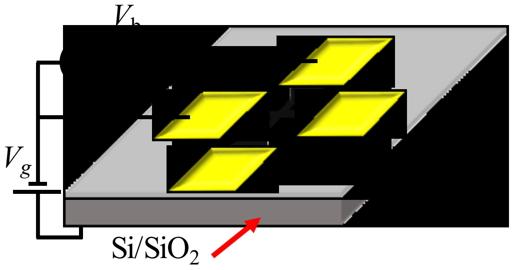

Figure 5.1: Schematics of a graphene/NDI-Py-Ag-Py-NDI/graphene tunnel junction at the intersection of two graphene ribbons (black/grey) are mounted on 300 nm of SiO_2 as a dielectric layer. Ohmic contacts are fabricated from Cr and Au thermally evaporated layers (yellow pads). V_b is the applied bias voltage across the tunnelling junction to drive a tunnelling current through the organic dielectric. V_g is the gate voltage applied on the bottom electrode and the back of the p-doped silicon Si substrate to modulate the concentration of the charge carrier.

5.2 *I-V* characteristics at 77K and 300K

The full lines of **Figure 5.2a** show the *I-V* curves of the self-assembled heterostructures across different areas of the tunnelling junctions (w^2 = 225 μm^2, 400 μm^2 and 900 μm^2). The tunnelling conductance of the trilayer device was found to be proportional to the areas of the tunnelling junctions w^2 (Figure 5.2, Inset). The measured current shows a linear dependence on bias voltage at low voltages which is inconsistent with the theoretical prediction of the tunnelling current of the graphene-insulator-graphene model, discussed in section 2.3.3 (equation 2-29), where the current shows a strong dependence (V^3) on the bias voltage. This might be due to the existence of a strong scattering that could lift the energy conservation rules. In addition, it is possible that the thermionic current at 77 K contributes more to the measured current compared to the direct tunnelling across the junction

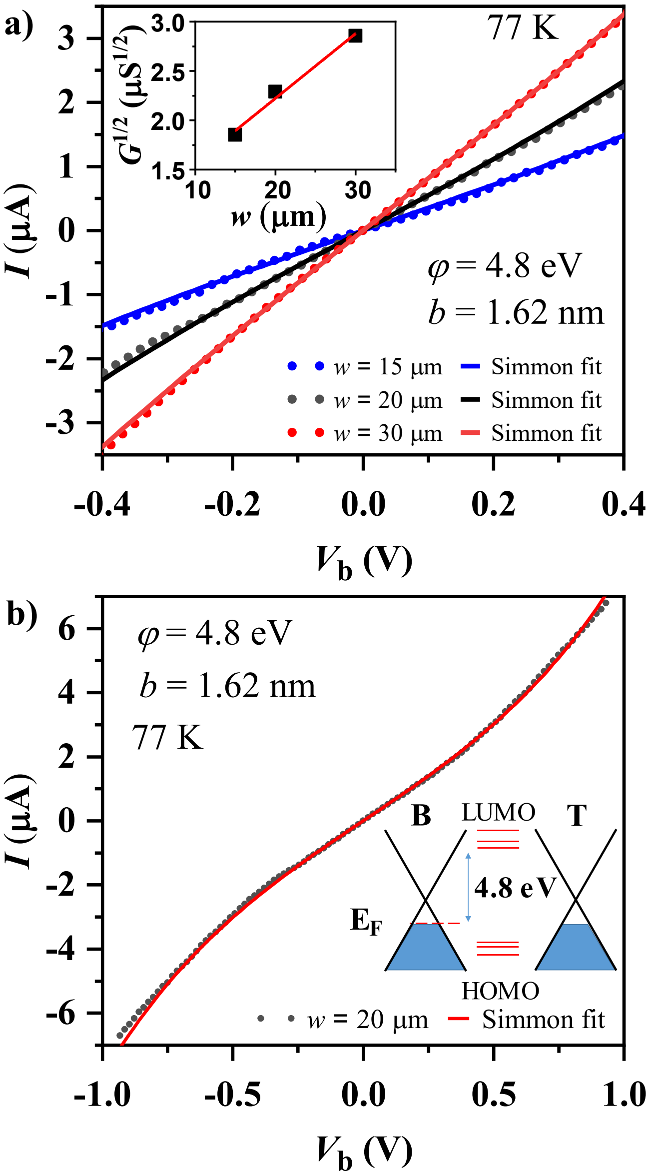

Figure 5.2: a) *I-V* characteristics of self-assembled devices of different tunnel junctions of width w = 15 µm, 20 µm, and 30 µm at 77 K (symbols). The best fits of the experimental I-V characteristics with Simmons` approximation (solid line) with barrier width b = 1.62 nm and barrier height φ = 4.8 eV. Inset: the dependence of the conductance on the cross-sectional area. **b)** *I-V* characteristic of a self-assembled device with 20 µm wide tunnelling junction at 77K (black dots) showing nonlinearity with the best fit (red line) with two free parameters: barrier width b = 1.62 nm and barrier height φ = 4.8 eV. Inset: Sketch of the expected band structure at $V_b \sim 0$ V.

which leads to a different dependence on the voltage. Here, to obtain an approximate value for the width of the tunnel barrier *b*, we fitted the curves with Simmons` equation (**Chapter 2, equation 2-25**)[64] where the potential barrier height φ arises from energy gap between the HOMO and LUMO of the pyridine were taken to be another free parameter.[107-108] The theoretical HOMO-LUMO energy gap was found to be 4.1 eV.[109] For the best fit, the tunnelling current was measured for higher bias voltage up to 1 V (**Figure 5.2b**). From the best fits, the tunnel barrier width *b* was found to be 1.62 ± 0.04 nm from the nonlinear *I-V* curves of different tunnelling junction areas where the potential height was about 4.8 eV.

The consistent value of the tunnel width suggests that the molecular bridges between the graphene electrodes make an average angle of 72° with respect to the cores of the NDI-Py molecules. This is consistent with the dense packing of NDI molecules in the plane observed from the STM images (Figure 4.3a and Figure 4.3c) and the torque applied by the highly energetic and linear N-Ag-N ion-dipole bonds to the pyridylethyl groups which conspire to align them out of the plane.[110] The tunnel width would be higher (1.7 nm) if the pyridylethyl groups attached to the NDI cores were standing upright with and angle of 90° with respect to the plane of the cores.[62, 111]

The thermo-activated current across 20×20 μm^2 tunnel junction at room temperature (300) is quenched when the devices are cooled down to 77 K (**Figure 5.3a**). The tunnelling weakly depends on the temperature due to the high estimated potential barrier in the trilayer devices. The *I-V* curves of the self-assembled devices without organic tunnel barrier (G…G) exhibit a quasi-metallic behaviour with hardly any temperature dependence (**Figure 5.3b**). Thermionic current is absent in the G…G devices due to the lack of

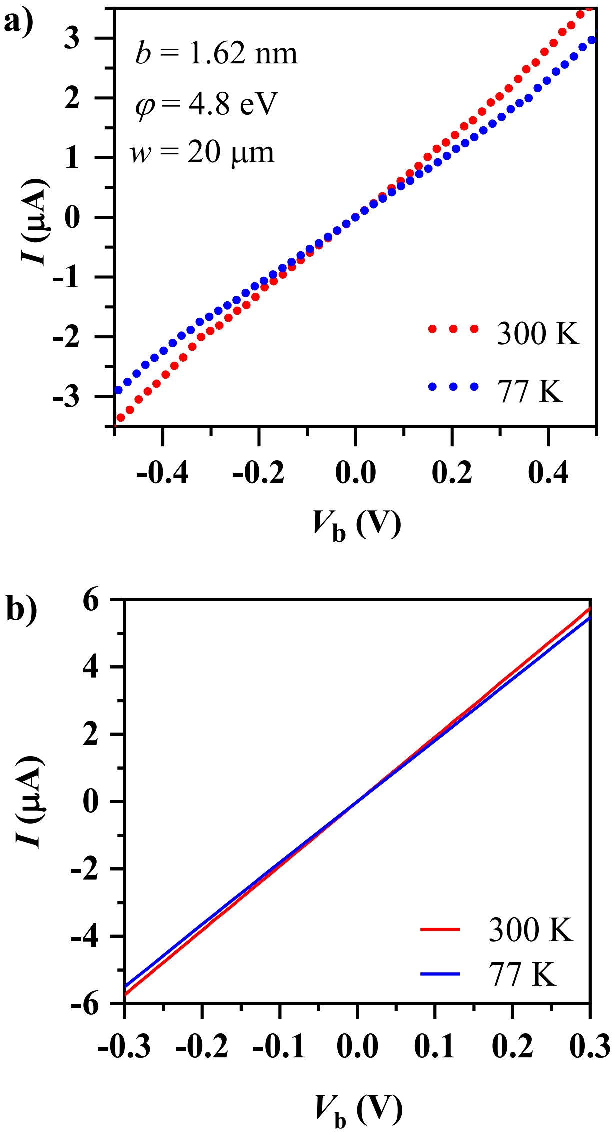

Figure 5.3: a) *I*-*V* measurements of a self-assembled device of width $w = 20$ μm at 300 K (red line) and 77 K (blue line) showing the activation of a thermionic current across the molecular bridges. **b)** *I*-*V* curves of a tunnel junction without the presence of the molecular bridge at 300 K (red line) and 77 K (blue line) showing the absence of the thermionic current as the graphene electrodes are in a direct contact with each other.

tunnel barrier where the top graphene electrode is in direct contact with the bottom graphene electrode. Yet, the existence of the thermo-activated current across the molecular tunnel barrier (a complete device) underlines the absence of the pinholes within the molecular bridges. This validates the dense quasi-crystalline arrangements of the NDI-Py which are observed in the low temperature STM images of the NDI-Py. We noticed that the conductivity of the complete devices are three times less than the graphene…graphene devices. However, one should expect a difference of orders of magnitude for such devices with tunnelling barriers. It might be needed to perform the experiments with exfoliated graphene to eliminate the contributions of the residual doping resulting from the graphene transfer in the G…G structures.

We further examine the molecular barrier by measuring the injected tunnelling current of 5 identical self-assembled devices of 20×20 μm^2 tunnel junctions with unclipped molecular bridges at 77 K to test the effect of clipped vs unclipped bridges on the electrical properties. In these devices, we stamped the graphene electrodes functionalised with NDI-Py without $AgNO_3$ (G/NDI-Py…NDI-Py/G). The injected tunnelling currents across these junctions vary from device to device (**Figure 5.4**). This suggests that the width of the tunnel barrier varies from device to device due to the unclipped molecular bridges. The inconsistency in the tunnel barrier width is tested by calculating standard deviation of the zero-bias conductance of the clipped and unclipped devices. The standard deviation of the zero-bias conductances in the unclipped devices was 5 times higher than that of the complete self-assembled.

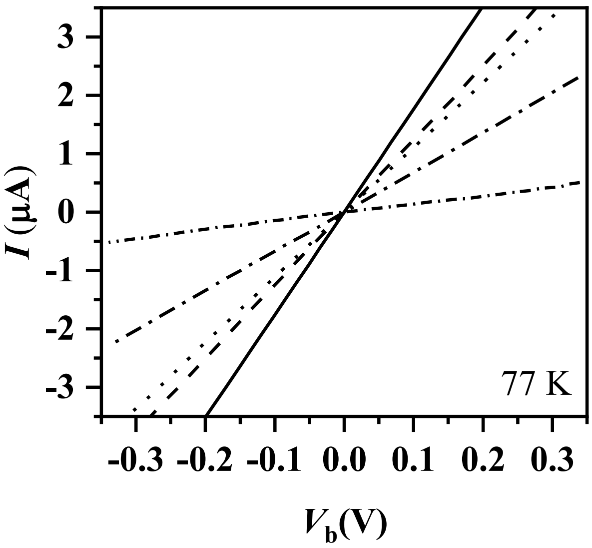

Figure 5.4: I-V curves of 5 self-assembled devices without Ag (unclipped molecular bridges) of widths w = 20 μm at 77 K. The tunnel barrier width varies from device to another due to omitting the Ag atoms, hence a wide range of zero-bias conductances.

The molecular bridge width observed in our devices (b = 1.6 nm) could be increased or decreased by changing the number of the carbon atoms already existing in the ethyl spacer that links the pyridine molecule to the NDI molecule. Our pyridinic endings were articulated to the central body with 2 C-C bonds to give two rotational degree of freedom mimicking elbow and wrist articulations when rotating with the α and β angles as shown in Figure 3.1b. Less than 2 C-C bonds would make the molecule too stiff for the Py endings to align with the Py of another molecule. More than 2 C-C bonds may give wider tunnel barriers but introduce additional degrees of freedom. These are likely to let Py endings lie on the graphene surface instead of rising above it. The barrier height could for example be tuned by replacing

Ag with Au ion-dipole bonds or by engineering chemical derivatives of pyridine groups with different HOMO-LUMO separations.

The self-assembled organic heterostructures did not exhibit any sign of negative differential resistance NDR in their *I-V* curves which normally arises from aligning the Dirac points of the top and bottom graphene electrodes. The NDR regions may be observed under conditions where the tunnel junction has translational symmetry in the plane of the layers. This would require substituting polycrystalline CVD graphene with exfoliated graphene.[17, 19] In CVD graphene, the lack of translational symmetry relaxes the selection rules on the conservation of in-plane momentum and hinders the observation of negative differential resistance in the *I-V* curves. Moreover, the observation of NDR also might be hindered due to the defects or the impurities that may exist in such devices that are made of transferred CVD graphene.

5.3 Dependence of *I-V* characteristics on the chemical potential of bottom graphene electrode

We investigated the dependence of *I-V* curves on the chemical potential of the bottom graphene ribbon tuned by the back-gate voltage V_g applied between the bottom graphene and the p-doped silicon substrate. By injecting a current through applying a bias voltage across the molecular bridges at different energies relative to the Dirac points of graphene, one gains insight into the coherence of the tunnelling process. Here, we measured the *I-V* of a self-assembled device of 20×20 μm^2 tunnel junction at 77 K (**Figure 5.5a**). Then, we extracted the zero-bias resistance r_0 from the *I-V* curves for each

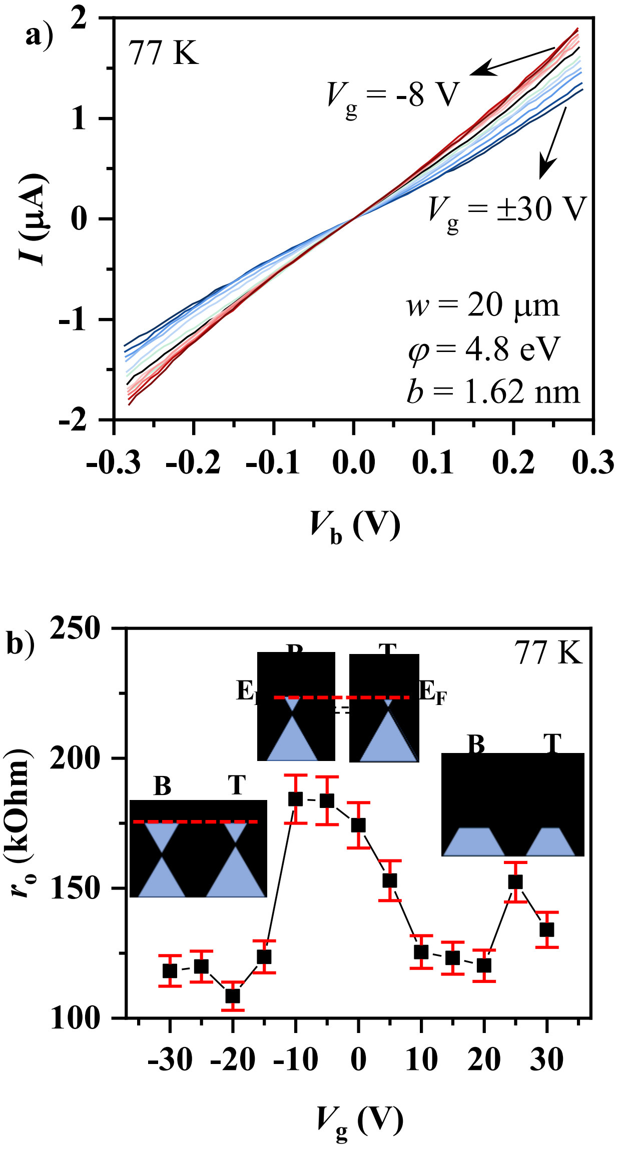

Figure 5.5: a) The *I-V* curves of a tunnel junction showing the dependence of the tunnelling conductance on the chemical potential of the bottom graphene by varying the applied back-gate potential V_g. The V_g was varied from - 30 V to + 30 V in steps of 5 V. **b)** The zero-bias resistance r_o extracted from the curves of (**a**) plotted as a function of V_g. The zero-bias resistance peak at V_g = -8 V when the Fermi level in both emitter and collector electrodes crosses the Dirac points of graphene. Black dashed lines refer to the positions of the Dirac points.

curve and plotted them as a function of the back-gate potential r_o - V_g (Figure 5.5b). We found that the zero-bias resistance $\boldsymbol{r_o}$ passes through a maximum at V_g = -8V. This peak is consistent with the chemical potential crossing the Dirac points of graphene where the density of states vanishes (Figure 5.5b, inset). From **Figure 5.5b**, we extracted the doping concentration of graphene due to the NDI-Py. Given the dielectric layer (SiO_2) thickness is d = 0.3 μm, the added hole concentration is $\Delta n_p = (\varepsilon_o\ \varepsilon_r / ed)\ \Delta V_g = 5.7\times10^{+11}$ cm^{-2}, where ε_r = 3.9 is the relative permittivity of SiO_2, e is the electron charge, and ε_o is the permittivity of vacuum. The carrier concentration extracted from this analysis shows that the graphene is n-doped ($5.7\times10^{+11} cm^{-2}$) and is not consistent with the estimated hole concentration ($3.6\times10^{+12}$ cm^{-2}) from the Raman spectrum of the graphene doped with the electron deficient NDI-Py molecules. This is probably due to the fact that the experiment has been done in a probe stations where the devices are exposed to air. In general, the polarity of the graphene in the organic self-assembled heterostructures could be changed by replacing the NDI-Py with molecules of electron rich pyrene cores. This type of molecules provides the same hydrogen-carbonyl bonds between the NDI-Py molecules which cause the pyrene cores to self-organise into dense packing structure with a lattice matching the graphene lattice.

5.4 Conclusion

The *I-V* characteristics of the tunnel junction demonstrate coherent tunnelling consistent with microstructural properties. The tunnelling transport at 77 K across the molecular bridges showed that the width of the potential barrier is 1.62 ± 0.04 nm while the height of the potential barrier is around 4.8 eV. In addition, quenching the thermo-activated current across the tunnel junction suggests that the molecular bridges are free of pinholes. These results agree with the density functional calculations and the conclusion drawn from the STM images that the NDI-Py arrange in dense quasi-crystalline structures. Tunnelling through the organic barrier was demonstrated through the observation of a peak in the tunnelling resistance as the chemical potential was swept across the Dirac points of graphene by applying a back-gate voltage. The peak is at V_g = -8 V as the graphene is n-doped due to exposing the graphene to air during the experiments which hinders observing the effect of the electron deficient cores of the NDI-Py molecules adsorbed on the graphene electrodes.

6 Conclusion and Future Work

6.1 Conclusion

In this work, we introduced a new concept for making organic van der Waals heterostructure. These structures were fabricated by a microfabrication process and with a bottom-up approach combined with chemical self-assembly. We functionalised monolayer graphene electrodes with NDI-Py molecules to form the multilayer structure. Our technique involved using noble metal reagent (Ag here) that allow clipping Pyridine radicals of the molecules via coordinative bond (Ag-N) while the NDI cores self-organise on the graphene electrodes through the hydrogen-carbonyl bonds between the cores. In this way, we promote the self-assembly of functionalized graphene electrodes to form an insulating layer of homogeneous thickness which provides an effective flexible tunnelling barrier.

We designed the fabrication method to shape, align and stamp the graphene electrodes in a unique method. This involved transferring the top graphene electrode onto two-polymer flexible stamp (PIB/PDMS) as an intermediate substrate and depositing 30 nm of insulating layer (SiO_2) around the graphene to facilitate the alignment of the device. This microfabrication process is independent of the synthesis of the graphene. The organic heterostructures presented in this thesis may be fabricated on flexible substrates when utilizing the same technique in transferring the top graphene electrode especially the molecular bridges used here may show flexibility when one applies mechanical stress (bending) to test more interesting phenomena like piezoresistance.

Then, we investigated the structural properties of the self-assembled heterostructures by Raman Spectroscopy, low temperature STM, and XPS. Raman study showed that the NDI-Py shifted the G and 2D vibration mode peaks in the graphene spectrum to higher frequency due to the p-doping arising from the electron deficient cores of the molecules ($3.6\times10^{+12}$ cm^{-2}). We observed the vibration modes of the NDI-Py at 1414 cm^{-1}, 1459 cm^{-1}, and 1712 cm^{-1} corresponding to C-C bonds, C=C bonds and C=O carbonyl bonds in the molecules suggesting that the molecules were anchored to the graphene electrodes through the molecular cores. This conclusion is confirmed by the rise in the I_D/I_G ratio from 0.04 for pristine graphene to 0.12 for the graphene with NDI-Py molecules indicating that the NDI cores lie flat on the graphene and slightly perturb the graphene lattice at the imidic sites. The Low temperature STM images showed that the NDI-Py molecules self-organised into a quasi-crystalline 2D lattice through the hydrogen-carbonyl bonds between the NDI cores. The molecules formed a monolayer of the molecules where the pyridylethyl groups rise above the graphene plane which facilitate forming the ion-dipole bond of the pyridinic endings and Ag. We probed the formation of the Ag-N bond by taking XPS measurements to determine the Ag filling fraction of the pyridinic sites. We found that 65% of the pyridinic sites were in ion-dipole bonds with Ag.

The current-voltage (*I-V*) characteristics of the tunnel junction demonstrated coherent tunnelling consistent with microstructural properties. We inject tunnelling current across the tunnel junction by applying a bias voltage at 77 K and found that the molecular barrier width is found to be 1.62 ± 0.04 nm and the barrier height is around 4.8 eV (both as free parameters). The thermionic-activated current was quenched when cooling down to 77 K due to the existence of the molecular bridges between the graphene electrodes validating the dense crystalline structures observed from the STM images of the NDI-Py molecules. We showed that the heterostructure devices without the organic molecular bridge exhibited quasi-metallic behaviour due to the lack of tunnel barrier. Also, the devices of unclipped molecular bridges (omitting Ag) showed fluctuations in zero-resistance of identical devices due to the variations in the tunnel barrier width. The chemical potential of the bottom graphene electrode of the self-assembled devices was tuned by applying gate voltage to inject tunnelling current at different energies relative to the Gamma point of graphene. The *I-V* characteristics of the self-assembled devices showed the dependency of the tunnelling current on the gate voltage as the role of gating is to change the chemical potential of the bottom graphene electrode. Back gate action modulates zero-field tunnelling resistance r_o showing a resistance maximum at about – 8 V back gate due to the n-doping (of $5.7\times10^{+11}$ cm^{-2}) probably due to performing the experiment in a probe station which exposed the devices to the air. This is not matching what we expect from the electron-deficient cores of the molecules that induce p-doping. The concentration is estimated from the Raman spectrum of graphene doped with NDI-Py ($3.6\times10^{+12}$ cm^{-2}). Hence the doping causes the Raman vibration peaks of monolayer graphene to shift to higher frequencies

In summary, the presented fabrication process is suitable to construct van der Waals superlattices alternating graphene, organic monolayers replacing the 2D insulating layer like hBN and semiconductors like TMCs. Our approach in fabricating device fills the need for finding insulator barrier layers that are thin, flexible, self-assembled and biocompatible. The process also solves the problem in aligning the graphene electrodes when using transparent sacrificial layers for the transfer process or final transparent flexible substrates. The use of the NDI-Py molecules with cores matching the graphene lattice is the key concept in fabricating the organic heterostructure due to the self-organisation of the NDI-based molecules in tight packing structures. This is combined with fine design of the attached molecular bridges (pyridylethyl groups) that are free to rotate and clip the alternating graphene electrodes. This approach paves the way to making a variety of organic heterostructures by synthesising organic molecules with different functional groups through supramolecular chemistry.

6.2 Future work

We plan to study the electrical transport properties in the presence of magnetic field at low temperatures including the investigation of the possibility of observing NDR regions in the *I-V* curves of the organic heterostructures. Applying perpendicular magnetic field quenches in-plane momentum scattering caused by the lack of the translational symmetry in the polycrystalline CVD graphene. The magnetic field generates sharp Landau-levels allowing to observe NDR regions when the levels of the top and bottom graphene electrodes are aligned and misaligned by electrostatic potential across the junctions. This is combined with applying a back-gate voltage to modulate the chemical potential of the bottom graphene electrodes.

New experiments that transfer our organic heterostructures onto flexible substrates have been started. By fabricating these devices, we will be studying the effect of applying a mechanical stress (by bending the substrates) on the resistance of the devices (Piezoresistance). This is possible as the layers of the devices are flexible including the organic molecular bridges. We have chosen Polyethylene naphthalate (PEN) substrate for being flexible and transparent. Monolayer graphene sheets transferred on PEN substrates may be obtained from the graphene market to save some time or could be wet transferred from graphene on Cu substrate using PMMA. All baking temperatures used to cure the polymers used in our fabrication process do not exceed 100 °C and are suitable for PEN substrates as the glass transition temperature of PEN is 200 °C. Using PMMA will still be possible only to wet transfer the full graphene sheets onto PEN substrates as the temperature required to bake this polymer is 165 °C. Our approach involves testing the ability to locate the graphene bars after performing the photolithography process on the PEN substrates as bottom electrodes in order to align the electrodes later. This might require us to evaporate an insulating layer (SiO_2) around the bottom graphene electrodes in the same way as in transferring the top graphene electrode of our devices (Chapter 3, section 3.2.2). It will be useful to start with 10 nm of SiO_2. The next steps to fabricate the devices on the flexible PEN would be the same of our step to stamp the graphene electrodes.

Engineering NDI molecules with different functional groups that could be clipped together without using silver would be another approach to form pure organic molecules free of the metal reagents and to reduce the cost of the fabrication process further. This is possible via the magic of the supramolecular chemistry in producing wide families of supramolecular structures and our microfabrication process in producing such devices.

References

[1] A. L. McWhorter, A. G. Foyt. Bulk GaAs Negative Conductance Amplifiers. *Applied Physics Letters* **1966**, 9, 300.

[2] E. R. Brown, J. R. Söderström, C. D. Parker, L. J. Mahoney, K. M. Molvar, T. C. McGill. Oscillations up to 712 GHz in InAs/AlSb resonant-tunneling diodes. *Applied Physics Letters* **1991**, 58, 2291.

[3] L. L. Chang, L. Esaki, R. Tsu. Resonant tunneling in semiconductor double barriers. *Applied Physics Letters* **1974**, 24, 593.

[4] L. Esaki. New Phenomenon in Narrow Germanium *p-n* Junctions. *Physical Review* **1958**, 109, 603.

[5] S.-I. Park, A.-P. Le, J. Wu, Y. Huang, X. Li, J. A. Rogers. Light Emission Characteristics and Mechanics of Foldable Inorganic Light-Emitting Diodes. *Advanced Materials* **2010**, 22, 3062.

[6] A. Nogaret. Negative differential conductance materials for flexible electronics. *Journal of Applied Polymer Science* **2014**, 131, n/a.

[7] C. Reese, M. Roberts, M.-m. Ling, Z. Bao. Organic thin film transistors. *Materials Today* **2004**, 7, 20.

[8] J. Lin, D. Ma. Origin of negative differential resistance and memory characteristics in organic devices based on tris(8-hydroxyquinoline) aluminum. *Journal of Applied Physics* **2008**, 103, 124505.

[9] D. L. Duong, S. J. Yun, Y. H. Lee. van der Waals Layered Materials: Opportunities and Challenges. *ACS Nano* **2017**, 11, 11803.

[10] C. J. Summers, K. F. Brennan, A. Torabi, H. M. Harris. Resonant tunneling and negative differential resistance in a variably spaced superlattice energy filter. *Applied Physics Letters* **1988**, 52, 132.

[11] S. Littlejohn, A. Nogaret, G. M. Prentice, G. D. Pantos. Pressure Sensing and Electronic Amplification with Functionalized Graphite–Silicone Composite. *Advanced Functional Materials* **2013**, 23, 5398.

[12] K. S. Novoselov, A. K. Geim, S. V. Morozov, D. Jiang, Y. Zhang, S. V. Dubonos, I. V. Grigorieva, A. A. Firsov. Electric Field Effect in Atomically Thin Carbon Films. *Science* **2004**, 306, 666.

[13] F. Giannazzo, G. Greco, F. Roccaforte, S. S. Sonde. Vertical Transistors Based on 2D Materials: Status and Prospects. *Crystals* **2018**, 8, 70.

[14] K. S. Novoselov, D. Jiang, F. Schedin, T. J. Booth, V. V. Khotkevich, S. V. Morozov, A. K. Geim. Two-dimensional atomic crystals. *Proceedings of the National Academy of Sciences of the United States of America* **2005**, 102, 10451.

[15] M. C. Lemme, T. J. Echtermeyer, M. Baus, H. Kurz. A Graphene Field-Effect Device. *IEEE Electron Device Letters* **2007**, 28, 282.

[16] F. Schwierz. Graphene transistors. *Nat Nano* **2010**, 5, 487.

[17] L. Britnell, R. V. Gorbachev, A. K. Geim, L. A. Ponomarenko, A. Mishchenko, M. T. Greenaway, T. M. Fromhold, K. S. Novoselov, L. Eaves. Resonant tunnelling and negative differential conductance in graphene transistors. **2013**, 4, 1794.

[18] L. Britnell, R. V. Gorbachev, R. Jalil, B. D. Belle, F. Schedin, A. Mishchenko, T. Georgiou, M. I. Katsnelson, L. Eaves, S. V. Morozov, N. M. R. Peres, J. Leist, A. K. Geim, K. S. Novoselov, L. A. Ponomarenko. Field-Effect Tunneling Transistor Based on Vertical Graphene Heterostructures. *Science* **2012**, 335, 947.

[19] Y. Zhao, Z. Wan, X. Xu, S. R. Patil, U. Hetmaniuk, M. P. Anantram. Negative Differential Resistance in Boron Nitride Graphene Heterostructures: Physical Mechanisms and Size Scaling Analysis. **2015**, 5, 10712.

[20] C. R. Dean, A. F. Young, I. Meric, C. Lee, L. Wang, S. Sorgenfrei, K. Watanabe, T. Taniguchi, P. Kim, K. L. Shepard, J. Hone. Boron nitride substrates for high-quality graphene electronics. *Nature Nanotechnology* **2010**, 5, 722.

[21] H. H. Tsai, Y. K. Su, H. H. Lin, R. L. Wang, T. L. Lee. P-N double quantum well resonant interband tunneling diode with peak-to-valley current ratio of 144 at room temperature. *IEEE Electron Device Letters* **1994**, 15, 357.

[22] T. Georgiou, R. Jalil, B. D. Belle, L. Britnell, R. V. Gorbachev, S. V. Morozov, Y.-J. Kim, A. Gholinia, S. J. Haigh, O. Makarovsky, L. Eaves, L. A. Ponomarenko, A. K. Geim, K. S. Novoselov, A.

Mishchenko. Vertical field-effect transistor based on graphene–WS2 heterostructures for flexible and transparent electronics. *Nature Nanotechnology* **2013**, 8, 100.

[23] C. Fu, H.-p. Lin, J. M. Macleod, A. Krayev, F. Rosei, D. F. Perepichka. Unravelling the Self-Assembly of Hydrogen Bonded NDI Semiconductors in 2D and 3D. *Chemistry of Materials* **2016**, 28, 951.

[24] M. A. Kobaisi, S. V. Bhosale, K. Latham, A. M. Raynor, S. V. Bhosale. Functional Naphthalene Diimides: Synthesis, Properties, and Applications. *Chemical Reviews* **2016**, 116, 11685.

[25] D. Gray, A. McCaughan, B. Mookerji. Crystal Structure of Graphite, Graphene and Silicon **2009**.

[26] J. H. Warner, F. Schaffel, M. Rummeli, A. Bachmatiuk. Graphene : fundamentals and emergent applications. **2013**.

[27] D. D. L. Chung. Review Graphite. *Journal of Materials Science* **2002**, 37, 1475.

[28] M. S. Dresselhaus, G. Dresselhaus, R. Saito. Physics of carbon nanotubes. *Carbon* **1995**, 33, 883.

[29] C. Kittel. *Introduction to Solid State Physics*. John Wiley and Sons, USA **2004**.

[30] P. R. Wallace. The Band Theory of Graphite. *Physical Review* **1947**, 71, 622.

[31] A. H. Castro Neto, F. Guinea, N. M. R. Peres, K. S. Novoselov, A. K. Geim. The electronic properties of graphene. *Reviews of Modern Physics* **2009**, 81, 109.

[32] M. I. Katsnelson, A. K. Geim. Electron scattering on microscopic corrugations in graphene. *Philosophical Transactions of the Royal Society A: Mathematical, Physical and Engineering Sciences* **2008**, 366, 195.

[33] N. D. Mermin, H. Wagner. Absence of Ferromagnetism or Antiferromagnetism in One- or Two-Dimensional Isotropic Heisenberg Models. *Physical Review Letters* **1966**, 17, 1133.

[34] J. A. Venables, G. D. T. Spiller, M. Hanbucken. Nucleation and growth of thin films. *Reports on Progress in Physics* **1984**, 47, 399.

[35] W.-Q. Han, L. Wu, Y. Zhu, K. Watanabe, T. Taniguchi. Structure of chemically derived mono- and few-atomic-layer boron nitride sheets. *Applied Physics Letters* **2008**, 93, 223103.

[36] A. Reina, X. Jia, J. Ho, D. Nezich, H. Son, V. Bulovic, M. S. Dresselhaus, J. Kong. Large Area, Few-Layer Graphene Films on Arbitrary Substrates by Chemical Vapor Deposition. *Nano Letters* **2009**, 9, 30.

[37] Q. Yu, J. Lian, S. Siriponglert, H. Li, Y. P. Chen, S.-S. Pei. Graphene segregated on Ni surfaces and transferred to insulators. *Applied Physics Letters* **2008**, 93, 113103.

[38] B. C. Banerjee, T. J. Hirt, P. L. Walker. Pyrolytic Carbon Formation from Carbon Suboxide. *Nature* **1961**, 192, 450.

[39] A. E. Karu, M. Beer. Pyrolytic Formation of Highly Crystalline Graphite Films. *Journal of Applied Physics* **1966**, 37, 2179.

[40] C. Mattevi, H. Kim, M. Chhowalla. A review of chemical vapour deposition of graphene on copper. *Journal of Materials Chemistry* **2011**, 21, 3324.

[41] B. Dai, L. Fu, Z. Zou, M. Wang, H. Xu, S. Wang, Z. Liu. Rational design of a binary metal alloy for chemical vapour deposition growth of uniform single-layer graphene. **2011**, 2, 522.

[42] H.-A. S. Shin, J. Ryu, S.-P. Cho, E.-K. Lee, S. Cho, C. Lee, Y.-C. Joo, B. H. Hong. Highly uniform growth of monolayer graphene by chemical vapor deposition on Cu-Ag alloy catalysts. *Physical Chemistry Chemical Physics* **2014**, 16, 3087.

[43] S. Bae, H. Kim, Y. Lee, X. Xu, J.-S. Park, Y. Zheng, J. Balakrishnan, T. Lei, H. Ri Kim, Y. I. Song, Y.-J. Kim, K. S. Kim, B. Ozyilmaz, J.-H. Ahn, B. H. Hong, S. Iijima. Roll-to-roll production of 30-inch graphene films for transparent electrodes. *Nat Nano* **2010**, 5, 574.

[44] O. Chuhei, N. Ayato. Ultra-thin epitaxial films of graphite and hexagonal boron nitride on solid surfaces. *Journal of Physics: Condensed Matter* **1997**, 9, 1.

[45] H. Cao, Q. Yu, L. A. Jauregui, J. Tian, W. Wu, Z. Liu, R. Jalilian, D. K. Benjamin, Z. Jiang, J. Bao, S. S. Pei, Y. P. Chen. Electronic

transport in chemical vapor deposited graphene synthesized on Cu: Quantum Hall effect and weak localization. *Applied Physics Letters* 2010, 96, 122106.

[46] H. Cao, Q. Yu, R. Colby, D. Pandey, C. S. Park, J. Lian, D. Zemlyanov, I. Childres, V. Drachev, E. A. Stach, M. Hussain, H. Li, S. S. Pei, Y. P. Chen. Large-scale graphitic thin films synthesized on Ni and transferred to insulators: Structural and electronic properties. *Journal of Applied Physics* 2010, 107, 044310.

[47] W. Hiranyawasit, K. Punpattanakul, A. Pimpin, H. Kim, S. Jeon, W. Srituravanich. A novel method for transferring graphene onto PDMS. *Applied Surface Science* 2015, 358, 70.

[48] X. Li, W. Cai, J. An, S. Kim, J. Nah, D. Yang, R. Piner, A. Velamakanni, I. Jung, E. Tutuc, S. K. Banerjee, L. Colombo, R. S. Ruoff. Large-Area Synthesis of High-Quality and Uniform Graphene Films on Copper Foils. *Science* 2009, 324, 1312.

[49] A. Reina, H. Son, L. Jiao, B. Fan, M. S. Dresselhaus, Z. Liu, J. Kong. Transferring and Identification of Single- and Few-Layer Graphene on Arbitrary Substrates. *The Journal of Physical Chemistry C* 2008, 112, 17741.

[50] X. Liang, B. A. Sperling, I. Calizo, G. Cheng, C. A. Hacker, Q. Zhang, Y. Obeng, K. Yan, H. Peng, Q. Li, X. Zhu, H. Yuan, A. R. Hight Walker, Z. Liu, L.-m. Peng, C. A. Richter. Toward Clean and Crackless Transfer of Graphene. *ACS Nano* 2011, 5, 9144.

[51] J. W. Suk, A. Kitt, C. W. Magnuson, Y. Hao, S. Ahmed, J. An, A. K. Swan, B. B. Goldberg, R. S. Ruoff. Transfer of CVD-Grown Monolayer Graphene onto Arbitrary Substrates. *ACS Nano* **2011**, 5, 6916.

[52] J. W. Suk, W. H. Lee, J. Lee, H. Chou, R. D. Piner, Y. Hao, D. Akinwande, R. S. Ruoff. Enhancement of the Electrical Properties of Graphene Grown by Chemical Vapor Deposition via Controlling the Effects of Polymer Residue. *Nano Letters* **2013**, 13, 1462.

[53] X.-D. Chen, Z.-B. Liu, C.-Y. Zheng, F. Xing, X.-Q. Yan, Y. Chen, J.-G. Tian. High-quality and efficient transfer of large-area graphene films onto different substrates. *Carbon* **2013**, 56, 271.

[54] M. Bousa, Kalbac,Martin, Jirka,Ivan, Kavan,Ladislav, Frank,Otakar. Experimental Study of PIB-based CVD Graphene Transfer Efficiency presented at 7th International Conference. Proceedings of Abstracts, Ostrava (CZ) **2015**.

[55] S. Cha, M. Cha, S. Lee, J. H. Kang, C. Kim. Low-Temperature, Dry Transfer-Printing of a Patterned Graphene Monolayer. **2015**, 5, 17877.

[56] M. S. Dresselhaus, G. Dresselhaus. Intercalation compounds of graphite. *Advances in Physics* **1981**, 30, 139.

[57] D. C. Elias, R. R. Nair, T. M. G. Mohiuddin, S. V. Morozov, P. Blake, M. P. Halsall, A. C. Ferrari, D. W. Boukhvalov, M. I. Katsnelson, A. K. Geim, K. S. Novoselov. Control of Graphene's Properties by

Reversible Hydrogenation: Evidence for Graphane. *Science* **2009**, 323, 610.

[58] R. R. Nair, W. Ren, R. Jalil, I. Riaz, V. G. Kravets, L. Britnell, P. Blake, F. Schedin, A. S. Mayorov, S. Yuan, M. I. Katsnelson, H.-M. Cheng, W. Strupinski, L. G. Bulusheva, A. V. Okotrub, I. V. Grigorieva, A. N. Grigorenko, K. S. Novoselov, A. K. Geim. Fluorographene: A Two-Dimensional Counterpart of Teflon. *Small* **2010**, 6, 2877.

[59] Q. H. Wang, M. C. Hersam. Room-temperature molecular-resolution characterization of self-assembled organic monolayers on epitaxial graphene. *Nature Chemistry* **2009**, 1, 206.

[60] M. M. Durban, P. D. Kazarinoff, C. K. Luscombe. Synthesis and Characterization of Thiophene-Containing Naphthalene Diimide n-Type Copolymers for OFET Applications. *Macromolecules* **2010**, 43, 6348.

[61] G. M. Prentice, L. Emmett, V. Luxami, G. D. Pantoş. in *Naphthalenediimide and its Congeners: From Molecules to Materials*, DOI: 10.1039/9781782621386-00001, The Royal Society of Chemistry **2017**, p. 1.

[62] Y. Tsukada, K. Hirao, J. Mizuguchi. N,N'-Bis[2-(4-pyridyl)ethyl]naphthalene-1,8:4,5-bis(dicarboximide). *Acta Crystallographica Section E* **2007**, 63, o3872.

[63] K. Tambara, N. Ponnuswamy, G. Hennrich, G. D. Pantoş. Microwave-Assisted Synthesis of Naphthalenemonoimides and N-Desymmetrized Naphthalenediimides. *The Journal of Organic Chemistry* **2011**, 76, 3338.

[64] J. G. Simmons. Generalized Formula for the Electric Tunnel Effect between Similar Electrodes Separated by a Thin Insulating Film. *Journal of Applied Physics* **1963**, 34, 1793.

[65] M. I. Katsnelson, K. S. Novoselov, A. K. Geim. Chiral tunnelling and the Klein paradox in graphene. *Nature Physics* **2006**, 2, 620.

[66] R. Holm. The Electric Tunnel Effect across Thin Insulator Films in Contacts. *Journal of Applied Physics* **1951**, 22, 569.

[67] P. S. Goh, A. F. Ismail, B. C. Ng. in *Membrane Characterization*, DOI: https://doi.org/10.1016/B978-0-444-63776-5.00002-4 (Eds: N. Hilal, A. F. Ismail, T. Matsuura, D. Oatley-Radcliffe), Elsevier **2017**, p. 31.

[68] A. C. Ferrari, J. C. Meyer, V. Scardaci, C. Casiraghi, M. Lazzeri, F. Mauri, S. Piscanec, D. Jiang, K. S. Novoselov, S. Roth, A. K. Geim. Raman Spectrum of Graphene and Graphene Layers. *Physical Review Letters* **2006**, 97, 187401.

[69] F. Tuinstra, J. L. Koenig. Raman Spectrum of Graphite. *The Journal of Chemical Physics* **1970**, 53, 1126.

[70] I. Calizo, I. Bejenari, M. Rahman, G. Liu, A. A. Balandin. Ultraviolet Raman microscopy of single and multilayer graphene. *Journal of Applied Physics* **2009**, 106, 043509.

[71] B. Ryan, C. Luiz Gustavo, N. Lukas. Raman characterization of defects and dopants in graphene. *Journal of Physics: Condensed Matter* **2015**, 27, 083002.

[72] G. Binnig, H. Rohrer, C. Gerber, E. Weibel. Surface Studies by Scanning Tunneling Microscopy. *Physical Review Letters* **1982**, 49, 57.

[73] G. Binnig, H. Rohrer. Scanning tunneling microscopy---from birth to adolescence. *Reviews of Modern Physics* **1987**, 59, 615.

[74] R. Ebeling, S. Tsukamoto, E. Dirksen, V. Caciuc, T. J. J. Müller, N. Atodiresei, S. Karthäuser. Imaging Individual Molecular-Like Orbitals of a Non-Planar Naphthalene Diimide on Pt(111): A Combined STM and DFT Study. *The Journal of Physical Chemistry C* **2017**, 121, 26916.

[75] A. J. Martínez-Galera, N. Nicoara, J. I. Martínez, Y. J. Dappe, J. Ortega, J. M. Gómez-Rodríguez. Imaging Molecular Orbitals of PTCDA on Graphene on Pt(111): Electronic Structure by STM and First-Principles Calculations. *The Journal of Physical Chemistry C* **2014**, 118, 12782.

[76] M. Hollerer, D. Lüftner, P. Hurdax, T. Ules, S. Soubatch, F. S. Tautz, G. Koller, P. Puschnig, M. Sterrer, M. G. Ramsey. Charge Transfer and Orbital Level Alignment at Inorganic/Organic Interfaces: The Role of Dielectric Interlayers. *ACS Nano* **2017**, 11, 6252.

[77] K. Siegbahn, K. Edvarson. β-ray spectroscopy in the precision range of 1 : 105. *Nuclear Physics* **1956**, 1, 137.

[78] K. Siegbahn, K. V.-s. i. Uppsala. *ESCA; Atomic, Molecular and Solid State Structure Studied by Means of Electron Spectroscopy*. Almqvist & Wiksells, **1967**.

[79] N. H. Turner, J. A. Schreifels. Surface Analysis: X-ray Photoelectron Spectroscopy and Auger Electron Spectroscopy. *Analytical Chemistry* **2000**, 72, 99.

[80] J. F. Moulder, W. F. Stickle, P. E. Sobol, K. D. Bomben. *Handbook of X-ray Photoelectron Spectroscopy*. Perkin-Elmer Corporation, Eden Prairie, Minnesota **1992**.

[81] M. C. Prado, D. Jariwala, T. J. Marks, M. C. Hersam. Optimization of graphene dry etching conditions via combined microscopic and spectroscopic analysis. *Applied Physics Letters* **2013**, 102, 193111.

[82] A. C. Ferrari, J. Robertson. Interpretation of Raman spectra of disordered and amorphous carbon. *Physical Review B* **2000**, 61, 14095.

[83] J. Maultzsch, S. Reich, C. Thomsen. Double-resonant Raman scattering in graphite: Interference effects, selection rules, and phonon dispersion. *Physical Review B* **2004**, 70, 155403.

[84] T. Shimada, T. Sugai, C. Fantini, M. Souza, L. G. Cançado, A. Jorio, M. A. Pimenta, R. Saito, A. Grüneis, G. Dresselhaus, M. S. Dresselhaus, Y. Ohno, T. Mizutani, H. Shinohara. Origin of the 2450cm−1 Raman bands in HOPG, single-wall and double-wall carbon nanotubes. *Carbon* **2005**, 43, 1049.

[85] A. C. Ferrari, D. M. Basko. Raman spectroscopy as a versatile tool for studying the properties of graphene. *Nature Nanotechnology* **2013**, 8, 235.

[86] A. C. Ferrari. Raman spectroscopy of graphene and graphite: Disorder, electron–phonon coupling, doping and nonadiabatic effects. *Solid State Communications* **2007**, 143, 47.

[87] A. Das, S. Pisana, B. Chakraborty, S. Piscanec, S. K. Saha, U. V. Waghmare, K. S. Novoselov, H. R. Krishnamurthy, A. K. Geim, A. C. Ferrari, A. K. Sood. Monitoring dopants by Raman scattering in an electrochemically top-gated graphene transistor. *Nature Nanotechnology* **2008**, 3, 210.

[88] S. Pisana, M. Lazzeri, C. Casiraghi, K. S. Novoselov, A. K. Geim, A. C. Ferrari, F. Mauri. Breakdown of the adiabatic Born–Oppenheimer approximation in graphene. *Nature Materials* **2007**, 6, 198.

[89] J. Yan, Y. Zhang, P. Kim, A. Pinczuk. Electric Field Effect Tuning of Electron-Phonon Coupling in Graphene. *Physical Review Letters* **2007**, 98, 166802.

[90] H. Yan, F. Xia, W. Zhu, M. Freitag, C. Dimitrakopoulos, A. A. Bol, G. Tulevski, P. Avouris. Infrared Spectroscopy of Wafer-Scale Graphene. *ACS Nano* **2011**, 5, 9854.

[91] L. Kortekaas, F. Lancia, J. D. Steen, W. R. Browne. Reversible Charge Trapping in Bis-Carbazole-Diimide Redox Polymers with Complete Luminescence Quenching Enabling Nondestructive

Read-Out by Resonance Raman Spectroscopy. *The Journal of Physical Chemistry C* **2017**, 121, 14688.

[92] Y.-L. Wu, K. E. Brown, D. M. Gardner, S. M. Dyar, M. R. Wasielewski. Photoinduced Hole Injection into a Self-Assembled π-Extended G-Quadruplex. *Journal of the American Chemical Society* **2015**, 137, 3981.

[93] M. S. Dresselhaus, G. Dresselhaus, R. Saito, A. Jorio. Raman spectroscopy of carbon nanotubes. *Physics Reports* **2005**, 409, 47.

[94] A. D. Becke. Density-functional thermochemistry. III. The role of exact exchange. *The Journal of Chemical Physics* **1993**, 98, 5648.

[95] C. Lee, W. Yang, R. G. Parr. Development of the Colle-Salvetti correlation-energy formula into a functional of the electron density. *Physical Review B* **1988**, 37, 785.

[96] W. J. Hehre, R. Ditchfield, J. A. Pople. Self—Consistent Molecular Orbital Methods. XII. Further Extensions of Gaussian—Type Basis Sets for Use in Molecular Orbital Studies of Organic Molecules. *The Journal of Chemical Physics* **1972**, 56, 2257.

[97] T. Kakinuma, H. Kojima, M. Ashizawa, H. Matsumoto, T. Mori. Correlation of mobility and molecular packing in organic transistors based on cycloalkyl naphthalene diimides. *Journal of Materials Chemistry C* **2013**, 1, 5395.

[98] B. Schulze Lammers, R. Ebeling, E. Dirksen, T. J. J. Müller, S. Karthäuser. Complex Adsorption Behavior of a Nonplanar

Naphthalene Diimide on Au(111). *The Journal of Physical Chemistry C* 2019, 123, 9860.

[99] S. Gabutti, M. Knutzen, M. Neuburger, G. Schull, R. Berndt, M. Mayor. A rigid sublimable naphthalenediimide cyclophane as model compound for UHV STM experiments. *Chemical Communications* 2008, DOI: 10.1039/B719796A2370.

[100] E. V. Anslyn, D. A. Dougherty. *Modern physical organic chemistry*. Sausalito, Calif. : University Science Books, Sausalito, Calif. 2006.

[101] A. D. Oyedele, C. M. Rouleau, D. B. Geohegan, K. Xiao. The growth and assembly of organic molecules and inorganic 2D materials on graphene for van der Waals heterostructures. *Carbon* 2018, 131, 246.

[102] V. Miseikis, D. Convertino, N. Mishra, M. Gemmi, T. Mashoff, S. Heun, N. Haghighian, F. Bisio, M. Canepa, V. Piazza, C. Coletti. Rapid CVD growth of millimetre-sized single crystal graphene using a cold-wall reactor. *2D Materials* 2015, 2, 014006.

[103] A. K.-V. Alexander V. Naumkin, Stephen W. Gaarenstroom, and Cedric J. Powell. NIST X-ray Photoelectron Spectroscopy Database, DOI: 10.18434/T4T88K, U.S. 2000.

[104] A. Dolatkhah, P. Jani, L. D. Wilson. Redox-Responsive Polymer Template as an Advanced Multifunctional Catalyst Support for Silver Nanoparticles. *Langmuir* 2018, 34, 10560.

[105] J. J. R. Frausto da Silva. The chelate effect redefined. *Journal of Chemical Education* **1983**, 60, 390.

[106] V. Vallet, U. Wahlgren, I. Grenthe. Chelate Effect and Thermodynamics of Metal Complex Formation in Solution: A Quantum Chemical Study. *Journal of the American Chemical Society* **2003**, 125, 14941.

[107] E. B. Hughes, H. H. G. Jellinek, B. A. Ambrose. Pyridine. Ultraviolet Absorption Spectrum and Dissociation Constant. *The Journal of Physical and Colloid Chemistry* **1949**, 53, 410.

[108] T. Karlsen, K. J. Børve, L. J. Sæthre, K. Wiesner, M. Bässler, S. Svensson. Toward the Spectrum of Free Polyethylene: Linear Alkanes Studied by Carbon 1s Photoelectron Spectroscopy and Theory. *Journal of the American Chemical Society* **2002**, 124, 7866.

[109] H. R. Moon, C. H. Choi, M. P. Suh. A Stair-Shaped Molecular Silver(0) Chain. *Angewandte Chemie International Edition* **2008**, 47, 8390.

[110] S. Roca, D. Vikić-Topić, J. Plavec, P. Šket, Z. Mihalić, D. Matković-Čalogović, Z. Popović. Structural diversity of the Ag coordination sphere in complexes of silver(I) nitrate with 3-halopyridine. Characterization of the complexes in solution and in the solid state. *Polyhedron* **2016**, 109, 166.

[111] A. Y. Robin, J. L. Sagué, K. M. Fromm. On the coordination behaviour of NO3- in coordination compounds with Ag+ Part 1.

Solubility effect on the formation of coordination polymer networks between AgNO3 and L (L = ethanediyl bis(isonicotinate) as a function of solvent. *CrystEngComm* **2006**, 8, 403.